Università degli Studi di Torino

Scuola di Dottorato in Scienza ed Alta Tecnologia
Indirizzo di Fisica ed Astrofisica

Muon Reconstruction and Momentum Scale Calibration and Their Application to Standard Model Higgs Searches with the CMS Experiment

Coordinatore
Prof. Guido Boffetta

Tutore
Dr. Nicola Amapane

Candidato
Daniele Trocino

Ciclo XXIII

Date of dissertation

27th January 2011

Candidate

Daniele Trocino

Tutor

Dr. Nicola Amapane
Università degli Studi di Torino

Degree board

Prof. C. Peroni
Università degli Studi di Torino

Prof. M. Paganoni
Università degli Studi di Milano Bicocca

Dr. M. Mulders
CERN

Dr. L. Pontecorvo
INFN Roma I, CERN

Ph.D. coordinator

Prof. Guido Boffetta
Università degli Studi di Torino

Acknowledgements

So many people have contributed to the accomplishment of this thesis that it is almost impossible to mention all of them.

First, I would like to thank the CMS Torino group: Amedeo, Nadia, Silvia, Vincenzo and all the others. Special thanks to Prof. Alessandra Romero, for her wise advice and support.

All my gratitude goes to my advisor, Nicola, for his constant presence, his invaluable suggestions and the exceptional care he put in revising this thesis.

Many thanks to my "boss" and friend Riccardo, for teaching me all there is to know about muons, and for all the *épée* matches we played.

I will never find enough words to thank Chiara, for the physics she has taught me, but mostly for the support and friendship she has always shown me.

There are a number of people to whom I am indebted for their help and the important contribution to my work: Slava, Martijn, Marco D., Sara, Nicola D., Yves, Giovanni, Zoltan, Gianluca, and many more – I apologise to all those I forgot. Special thanks go to Dr. Ludovico Pontecorvo, for the careful and enthusiastic revision of this thesis, and to Dr. Alessandro Ballestrero, for his useful suggestions.

A thought to all friends that have made my life at CERN so pleasant: Grazia, Bruno, Alessia, Nhan, Alessandro, Alberto and Matteo, just to mention a few. But first of all, the crew of *"Casa Torino"*: Cristina, Roberto, Giorgia, Marco and Susy. In particular, I am grateful to Cri, with whom I have shared work and worries.

Thanks to my long-time friends, Andrea, Francesco, Silvia, Antonietta and Filomena, who have helped me through hard times and kept me in touch with reality.

Finally, my deepest gratitude to my mother and father, to Arianna, and to my whole family. For everything.

A nonna Maria, con affettuoso ricordo.

Contents

Introduction

On 23 November 2009, the Large Hadron Collider (LHC) produced the first proton-proton collisions and finally entered the "physics era", after over twenty years of construction and commissioning. At the beginning of 2010, the beams were ramped up to 3.5 TeV and, on 30 March 2010, the first collisions at a centre-of-mass energy of 7 TeV were recorded, reaching the highest energy ever touched at a particle collider. At this energy, LHC delivered proton-proton collisions for an integrated luminosity of about 47 pb^{-1}, with a maximum instantaneous luminosity of $2 \cdot 10^{32}$ $\text{cm}^{-2}\text{s}^{-1}$. In the next years, LHC is expected to reach the design centre-of-mass energy of 14 TeV and an instantaneous luminosity of $2 \cdot 10^{34}$ $\text{cm}^{-2}\text{s}^{-1}$.

Such a huge effort is motivated by an ambitious physics program. The first and most pressing question to which the LHC will give a final answer is certainly the existence of the Higgs boson, the only still unconfirmed element of the Standard Model (SM) of particle interactions, regarded as the responsible for the masses of all the known elementary particles. More generally, it will be possible to investigate the mechanism of the electroweak symmetry breaking, of which the Higgs mechanism is the simplest realization in the SM. The LHC will also test a number of theories and physics models which aim to describe the particle interactions beyond the limits of the SM, the most notable of which is probably supersymmetry (SUSY). Besides all existing models, however, the LHC is open to any new and unexpected phenomenon or particle that may show up at this unexplored energy scale. Two of the main LHC experiments, CMS (Compact Muon Solendoid) and ATLAS (A ToroidaL ApparatuS), are designed to address these fundamental questions.

The search for extremely rare processes is made possible by the very high LHC design luminosity, with an event rate of the order of 1 GHz, which the detectors can sustain thanks to innovative hardware and software technologies. The background rate exceeds the interesting physics signals by a factor of 10^9. In such a challenging environment, one of the cleanest signature is offered by muons. The most relevant example is probably the decay of the Higgs boson into four muons, which is regarded as the "golden channel" for the Higgs discovery at the LHC.

This thesis describes my Ph.D. work, carried out in the last three years within the CMS collaboration. Throughout this time, the main goal of my work has been the study of the SM Higgs boson in its “golden” decay mode. For this purpose, I started from the development of the tools needed for this analysis: the algorithms for the identification and tracking of muons and for the precise measurement of their properties. This work is documented in Chapters 3 and 4 of this thesis, after a general introduction on LHC, its physics program and the CMS detector (Chapters 1 and 2). In particular, Chapter 3 is entirely devoted to the reconstruction of muons. Particular emphasis is put on the reconstruction inside the muon spectrometer, which I developed and for which I am currently responsible in CMS. This chapter describes the main reconstruction algorithms and their performance on collision data, comparing it with the expectations from Monte Carlo simulation.

The momentum of tracks, though very accurate, is still affected by systematic biases, due the imperfect knowledge of the detector geometry, of its material and of the magnetic field. In Chapter 4, a strategy for the precise calibration of the track momentum scale is presented. This method uses muons coming from the decay of well-known resonances, in particular the J/ψ meson and the Z boson, to define corrections for track momenta, based on the knowledge of the resonance mass. The same algorithm can also provide a measurement of the track momentum resolution. Using large samples of J/ψ and Z candidates collected by CMS during the 2010 collision runs, I measured the resolution of the tracks reconstructed by the silicon tracker alone or in combination with the muon spectrometer, and I calibrated the track momentum scale in different pseudorapidity regions and momentum ranges. These corrections are currently used in several CMS physics analyses, such as the measurement of the J/ψ, Υ and Z production cross sections.

Finally, the discovery potential of the $H \rightarrow ZZ \rightarrow 4\ell$ process is discussed in Chapter 5. My work focused, in particular, on the 4μ final state, whose analysis strategy mostly relies on the muon reconstruction techniques presented in the previous chapters. The analysis strategy, based on a sequential set of cuts, has been developed using Monte Carlo simulations of the Higgs signal and of the backgrounds with realistic detector conditions, for an integrated luminosity of 1 fb^{-1} and a centre-of-mass energy of 7 TeV. The CMS sensitivity for the observation of a Higgs boson has been studied in the mass range from 115 GeV/c^2 to 250 GeV/c^2, combining the three leptonic final states. Finally, I applied the selection strategy to the first year’s data and compared the results with the expectations from simulation.

Chapter 1

Physics at the Large Hadron Collider

The fundamental components of matter and their interactions are nowadays best described by the Standard Model of Particle Physics (SM), which is based upon two separate quantum field theories, describing the *electroweak interaction* (Glashow-Weinberg-Salam model or GWS) and the *strong interaction* (Quantum Chromo-Dynamics or QCD). In this chapter, a short overview of the SM (Section 1.1) and of the electroweak theory (Section 1.2) is given, focusing the attention on the *ElectroWeak Symmetry Breaking* (EWSB), the Higgs mechanism and the Higgs boson (Section 1.3). Finally, in Section 1.4, the bases of the Higgs boson search are introduced.

1.1 The Standard Model of Elementary Particles

The SM [1] describes the matter as composed by twelve elementary particles, the *fermions*, all having half-integer spin. Fermions can be divided into two main groups, *leptons* and *quarks*, whose classification is given in Table 1.1. Quarks are subject to both strong and electroweak interactions and do not exist as free states, but only as constituents of a wide class of particles, the *hadrons*, such as protons and neutrons. Leptons, instead, only interact through electromagnetic and weak forces.

Fermions	1^{st} fam.	2^{nd} fam.	3^{rd} fam.	Charge	Interactions
Quarks	u	c	t	$+2/3$	All
	d	s	b	$-1/3$	
Leptons	e	μ	τ	-1	Weak, E.M.
	ν_e	ν_μ	ν_τ	0	Weak

Table 1.1: *Classification of the three families of fundamental fermions.*

In the SM, the interactions between particles are described in terms of the exchange of *bosons*, integer-spin particles which are carriers of the fundamental interactions. The main characteristics of bosons and corresponding interactions are summarised in Table 1.2. The *gravitational* interaction is not taken into account, as it is not relevant at the typical mass and distance scales of particle physics.

	Electromagnetic	Weak	Strong
Quantum	Photon (γ)	$W^{\pm}$, Z	Gluons
Mass [GeV/c^2]	0	80, 90	0
Coupling constant	$\alpha(Q^2 = 0) \approx \frac{1}{137}$	$\frac{G_F}{(\hbar c)^3} \approx 1.2 \cdot 10^{-5}$ GeV^{-2}	$\alpha_s(m_Z) \approx 0.1$
Range [cm]	∞	10^{-16}	10^{-13}

Table 1.2: *Fundamental interactions relevant in particle physics and corresponding carriers.*

As previously mentioned, the SM describes these interactions by means of two *gauge* theories: the Quantum Chromo-Dynamics and the theory of the electroweak interaction (GWS model), which unifies the electromagnetic and weak interactions. In the next sections, the electroweak theory will be described in some detail.

1.2 The Electroweak Theory

From a historical point of view, the starting point for the study of electroweak interactions is Fermi's theory of muon decay [2], which is based on an effective four-fermion Lagrangian:

$$\mathcal{L} = -\frac{4G_F}{\sqrt{2}}\bar{\nu}_\mu\gamma^\alpha\frac{1-\gamma_5}{2}\mu\bar{e}\gamma_\alpha\frac{1-\gamma_5}{2}\nu_e\,, \tag{1.1}$$

where G_F is the *Fermi coupling constant* reported in Table 1.2. Equation 1.1 represents a "point-like" interaction, with only one vertex and without any intermediate boson exchanged. It is usually referred to as $V-A$ interaction, being formed by a *vectorial* and an *axial* component. The term $\frac{1}{2}(1-\gamma_5)$ that appears in it is the negative helicity projector. Only the negative helicity (*left-handed*) component of fermions takes part to this interaction.

Fermi's Lagrangian is not renormalisable and it results in a non-unitary $\mathcal{S}$ matrix. Both problems of renormalisability and unitarity are overcome describing the weak interaction by a *gauge* theory, i.e. requiring its Lagrangian to be invariant under local transformations generated by the elements of some Lie group (*gauge transformations*). The specific group of local invariance (*gauge group*) is to be determined by the phenomenological properties of the interaction and of the particles involved. In particular, the resulting Lagrangian must reduce to Equation 1.1 in the low energy limit. A detailed derivation of this Lagrangian is not provided in this work, but the results are summarised in the following. For details about the GWS model, see [3][4][5].

A gauge theory for weak interactions is conceived as an extension of the theory of electromagnetic interaction, the Quantum Electro-Dynamics or QED, which is based on the gauge group $U(1)_{EM}$, associated to the conserved quantum number Q (*electric charge*). In this case, the condition of local invariance under the $U(1)_{EM}$ group leads to the existence of a massless vector, the *photon*.

A theory reproducing both the electromagnetic and weak interaction phenomenology is achieved by extending the gauge symmetry to the group $SU(2)_I \otimes U(1)_Y$. In this sense, the weak and electromagnetic interactions are said to be unified. The generators of $SU(2)_I$ are the three components of the *weak isospin* operator, $t^a = \frac{1}{2}\tau^a$, where τ^a are the Pauli matrices. The generator of $U(1)_Y$ is the *weak hypercharge* Y operator. The corresponding quantum numbers satisfy the following relation

$$Q = I_3 + \frac{Y}{2} \, ,$$

where I_3 is the third component of the weak isospin (eigenvalue of t^3).

Fermions can be divided in doublets of negative-helicity (*left-handed*) particles and singlets of positive-helicity (*right-handed*) particles, as follows:

$$L_L = \begin{pmatrix} \nu_{\ell,L} \\ \ell_L \end{pmatrix} , \quad \ell_R \, , \quad Q_L = \begin{pmatrix} u_L \\ d_L \end{pmatrix} , \quad u_R \, , \quad d_R \, , \tag{1.2}$$

where $\ell = e, \mu, \tau$, $u = u, c, t$ and $d = d, s, b$. Neutrinos have no *right* component, as their mass is taken as null. In Table 1.3, I_3, Y and Q quantum numbers of all fermions are reported.

	I_3	Y	Q
$\begin{pmatrix} u_L \\ d_L \end{pmatrix}$	$\begin{pmatrix} 1/2 \\ -1/2 \end{pmatrix}$	$\begin{pmatrix} 1/3 \\ 1/3 \end{pmatrix}$	$\begin{pmatrix} 2/3 \\ -1/3 \end{pmatrix}$
u_R, d_R	0, 0	$4/3$, $-2/3$	$2/3$, $-1/3$
$\begin{pmatrix} \nu_{\ell,L} \\ \ell_L \end{pmatrix}$	$\begin{pmatrix} \frac{1}{2} \\ -\frac{1}{2} \end{pmatrix}$	$\begin{pmatrix} -1 \\ -1 \end{pmatrix}$	$\begin{pmatrix} 0 \\ -1 \end{pmatrix}$
ℓ_R	0	-2	-1

Table 1.3: *Isospin (I_3), hypercharge (Y) and electric charge (Q) of all fermions.*

As well as for QED, the requirement of local gauge invariance with respect to the $SU(2)_I \otimes U(1)_Y$ group introduces now four massless vector fields (*gauge fields*), $W_\mu^{1,2,3}$ and B_μ, which couple to fermions with two different coupling constants, g and g'. Note that B_μ does not represent the photon field, because it arises from the $U(1)_Y$ group of hypercharge, instead of $U(1)_{EM}$ group of electric charge. The gauge-invariant Lagrangian for fermion fields can be written as follows:

$$\mathcal{L} = \overline{\Psi}_L \gamma^\mu \left(i\partial_\mu + g t_a \mathrm{W}_\mu^a - \tfrac{1}{2} g' Y \mathrm{B}_\mu \right) \Psi_L + \overline{\psi}_R \gamma^\mu \left(i\partial_\mu - \tfrac{1}{2} g' Y \mathrm{B}_\mu \right) \psi_R \quad (1.3)$$

where

$$\Psi_L = \begin{pmatrix} \psi_L^1 \\ \psi_L^2 \end{pmatrix}$$

and where Ψ_L and ψ_R are summed over all the possibilities in Equation 1.2.

As already stated, $W_\mu^{1,2,3}$ and B_μ do not represent physical fields, which are given instead by linear combinations of the four mentioned fields: the charged bosons W^+ and W^- correspond to[1]

$$\mathrm{W}_\mu^\pm = \sqrt{\frac{1}{2}}\,(\mathrm{W}_\mu^1 \mp i\mathrm{W}_\mu^2), \quad (1.4)$$

while the neutral bosons γ and Z correspond to

$$\begin{aligned} \mathrm{A}_\mu &= \mathrm{B}_\mu \cos\theta_W + \mathrm{W}_\mu^3 \sin\theta_W & (1.5) \\ \mathrm{Z}_\mu &= -\mathrm{B}_\mu \sin\theta_W + \mathrm{W}_\mu^3 \cos\theta_W, & (1.6) \end{aligned}$$

obtained by mixing the neutral fields W_μ^3 and B_μ with a rotation defined by the *Weinberg angle* θ_W. In terms of the fields in Equations 1.4 to 1.6, the interaction term between gauge fields and fermions, taken from the Lagrangian in Equation 1.3, becomes

$$\mathcal{L}_{int} = \frac{1}{2\sqrt{2}} g (J_\alpha^+ \mathrm{W}^{(+)\alpha} + J_\alpha^- \mathrm{W}^{(-)\alpha}) + \frac{1}{2}\sqrt{g'^2 + g^2} J_\alpha^{\mathrm{Z}} \mathrm{Z}^\alpha - e J_\alpha^{EM} \mathrm{A}^\alpha, \quad (1.7)$$

where J^{EM} is the electromagnetic current coupling to the photon field, while J^+, J^- and J^{Z} are the three weak isospin currents. It is found that

$$J_\alpha^{\mathrm{Z}} = J_\alpha^3 - 2\sin^2\theta_W \cdot J_\alpha^{EM}.$$

A_μ can then be identified with the photon field and, requiring the coupling terms to be equal, one obtains

$$g \sin\theta_W = g' \cos\theta_W = e \quad (1.8)$$

which represents the electroweak unification. The GWS model thus predicts the existence of two charged gauge fields, which only couple to left-handed fermions, and two neutral gauge fields, which interact with both left- and right-handed components.

---

[1] In the following, a different notation will be also used: $\mathrm{W}_\mu^{(-)} = \mathrm{W}_\mu$, $\mathrm{W}_\mu^{(+)} = \mathrm{W}_\mu^\dagger$.

1.3 The Higgs Mechanism

In order to correctly reproduce the phenomenology of weak interactions, both fermion and gauge boson fields must acquire mass, in agreement with experimental results. Up to this point, however, all particles are considered massless: in the electroweak Lagrangian, in fact, a mass term for the gauge bosons would violate gauge invariance, which is needed to ensure the renormalisability of the theory. Explicit mass terms for fermions, instead, would not violate gauge invariance, but in the GWS model the Lagrangian is also required to preserve the invariance under *chirality* transformations, and this is achieved only with massless fermions. Masses are thus introduced with the *Higgs mechanism* [6][7], which allows fermions and W$^{\pm}$, Z bosons to be massive, while keeping the photon massless. Such mechanism is accomplished by means of a doublet of complex scalar fields,

$$\phi = \begin{pmatrix} \phi^+ \\ \phi^0 \end{pmatrix} = \frac{1}{\sqrt{2}} \begin{pmatrix} \phi^1 + i\phi^2 \\ \phi^3 + i\phi^4 \end{pmatrix}, \tag{1.9}$$

which is introduced in the electroweak Lagrangian within the term

$$\mathcal{L}_{EWSB} = (D^\mu \phi)^\dagger (D_\mu \phi) + V(\phi^\dagger \phi), \tag{1.10}$$

where $D_\mu = \partial_\mu - igt_a \mathrm{W}^a_\mu + \frac{i}{2} g' Y \mathrm{B}_\mu$ is the covariant derivative. The Lagrangian in Equation 1.10 is invariant under $SU(2)_I \otimes U(1)_Y$ transformations, since the kinetic part is written in terms of covariant derivatives and the potential V only depends on the product $\phi^\dagger \phi$. The ϕ field is characterised by the following quantum numbers:

	I_3	Y	Q
$\begin{pmatrix} \phi^+ \\ \phi^0 \end{pmatrix}$	$\begin{pmatrix} 1/2 \\ -1/2 \end{pmatrix}$	$\begin{pmatrix} 1 \\ 1 \end{pmatrix}$	$\begin{pmatrix} 1 \\ 0 \end{pmatrix}$

Writing the potential term as follows (see also Figure 1.1 for a graphical representation)

$$V(\phi^\dagger \phi) = -\mu^2 \phi^\dagger \phi - \lambda (\phi^\dagger \phi)^2, \tag{1.11}$$

with $\mu^2 < 0$ and $\lambda > 0$, it results to have a minimum for

$$\phi^\dagger \phi = \frac{1}{2}(\phi_1^2 + \phi_2^2 + \phi_3^2 + \phi_4^2) = -\frac{\mu^2}{2\lambda} \equiv \frac{v^2}{2}. \tag{1.12}$$

This minimum is not found for a single value of ϕ, but for a manifold of non-zero values. The choice of (ϕ^+, ϕ^0) corresponding to the ground state, i.e. the lowest energy state or *vacuum*, is arbitrary, and the chosen point is not invariant under rotations in the (ϕ^+, ϕ^0) plane: this is referred to as

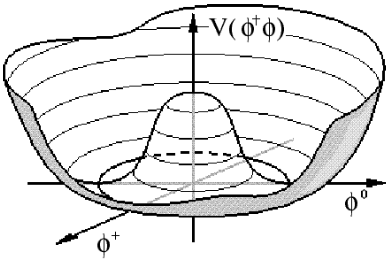

Figure 1.1: *Shape of the Higgs potential of Equation 1.11.*

spontaneous symmetry breaking. If one chooses to fix the ground state on the ϕ^0 axis, the vacuum expectation value of the ϕ field is

$$\langle\phi\rangle = \frac{1}{\sqrt{2}}\begin{pmatrix} 0 \\ v \end{pmatrix}, \quad v^2 = -\frac{\mu^2}{\lambda}. \tag{1.13}$$

The ϕ field can thus be rewritten in a generic gauge, in terms of its vacuum expectation value:

$$\phi = \frac{1}{\sqrt{2}} e^{\frac{i}{v}\phi^a t_a}\begin{pmatrix} 0 \\ \mathrm{H}+v \end{pmatrix}, \quad a = 1,2,3\ ,$$

where the three fields ϕ^a and the fourth $\phi^4 = \mathrm{H} + v$ are called *Goldstone fields*. Being scalar and massless, they introduce four new degrees of freedom, in addition to the six degrees due to the transverse polarisations of the massless vector bosons $\mathrm{W}^\pm$ and Z. The unitary gauge is fixed by the transformation

$$\phi' = e^{-\frac{i}{v}\phi^a t_a}\phi = \frac{1}{\sqrt{2}}\begin{pmatrix} 0 \\ \mathrm{H}+v \end{pmatrix} = \frac{1}{\sqrt{2}}\begin{pmatrix} 0 \\ \phi^4 \end{pmatrix}. \tag{1.14}$$

The remaining field, the *Higgs field*, has now a zero expectation value.

Rewriting the Lagrangian in Equation 1.10 with the ϕ field in the unitary gauge, $\mathcal{L}_{EWSB}$ results from the sum of three terms:

$$\mathcal{L}_{EWSB} = \mathcal{L}_{\mathrm{H}} + \mathcal{L}_{\mathrm{HW}} + \mathcal{L}_{\mathrm{HZ}}, \tag{1.15}$$

where the three terms can be written as follows, using the approximation $V \sim \mu^2\mathrm{H}^2 + \mathrm{const}$ and neglecting higher order terms:

$$\begin{aligned}
\mathcal{L}_{\mathrm{H}} &= \frac{1}{2}\partial_\alpha \mathrm{H}\partial^\alpha \mathrm{H} + \mu^2\mathrm{H}^2 \\
\mathcal{L}_{\mathrm{HW}} &= \frac{1}{4}v^2 g^2 \mathrm{W}_\alpha \mathrm{W}^{\dagger\alpha} + \frac{1}{2}v g^2 \mathrm{H}\mathrm{W}_\alpha \mathrm{W}^{\dagger\alpha} && (1.16) \\
&= m_{\mathrm{W}}^2 \mathrm{W}_\alpha \mathrm{W}^{\dagger\alpha} + g_{\mathrm{HW}}\mathrm{H}\mathrm{W}_\alpha \mathrm{W}^{\dagger\alpha} \\
\mathcal{L}_{\mathrm{HZ}} &= \frac{1}{8}v^2(g^2 + g'^2)\mathrm{Z}_\alpha \mathrm{Z}^\alpha + \frac{1}{4}v(g^2 + g'^2)\mathrm{H}\mathrm{Z}_\alpha \mathrm{Z}^\alpha && (1.17) \\
&= \frac{1}{2}m_{\mathrm{Z}}^2 \mathrm{Z}_\alpha \mathrm{Z}^\alpha + \frac{1}{2}g_{\mathrm{HZ}}\mathrm{H}\mathrm{Z}_\alpha \mathrm{Z}^\alpha
\end{aligned}$$

Equations 1.16 and 1.17 now contain mass terms for fields $\mathrm{W}^{\pm}$ and Z: each of the three gauge bosons has acquired mass and an additional degree of freedom, corresponding to the longitudinal polarisation. At the same time, three of the four Goldstone bosons have disappeared from the Lagrangian $\mathcal{L}_{EWSB}$, thus preserving the total number of degrees of freedom: the degrees related to the missing Goldstone bosons have become the longitudinal degrees of the vector bosons. Only the H scalar field is still present and has acquired mass itself: it is the Higgs field.

Summarising, the Higgs mechanism is used to introduce the weak boson masses, without explicitly breaking the gauge invariance, thus preserving the renormalisability of the theory. When a symmetry is "spontaneously" broken, in fact, it is not properly eliminated: it is rather "hidden" by the choice of the ground state. It can be shown that the minimum of the Higgs field is still invariant under the $U(1)_{EM}$ group. Hence, the electromagnetic symmetry is unbroken and the photon does not couple to the Higgs boson and remains massless.

1.3.1 Vector Boson Masses and Couplings

Equations 1.16 and 1.17 show that the masses of vector bosons $\mathrm{W}^{\pm}$ and Z are related to the parameter v, characteristic of the EWSB, and to the electroweak coupling constants:

$$\begin{cases} m_{\mathrm{W}} = \frac{1}{2} v g \\ m_{\mathrm{Z}} = \frac{1}{2} v \sqrt{g^2 + g'^2} \end{cases} \quad \rightarrow \quad \frac{m_{\mathrm{W}}}{m_{\mathrm{Z}}} = \frac{g}{\sqrt{g^2 + g'^2}} = \cos\theta_W . \tag{1.18}$$

Also the couplings of vector bosons to the Higgs can be obtained from Equations 1.16 and 1.17, and are found to depend on the square of m_{W} and m_{Z}:

$$g_{\mathrm{HW}} = \frac{1}{2} v g^2 = \frac{2}{v} m_{\mathrm{W}}^2 \tag{1.19}$$

$$g_{\mathrm{HZ}} = \frac{1}{2} v (g^2 + g'^2) = \frac{2}{v} m_{\mathrm{Z}}^2 . \tag{1.20}$$

A relation between the decay ratios of the Higgs boson to a W pair and to a Z pair can be derived from Equations 1.19 and 1.20:

$$\frac{BR(\mathrm{H} \rightarrow \mathrm{W}^+\mathrm{W}^-)}{BR(\mathrm{H} \rightarrow \mathrm{ZZ})} = \left(\frac{g_{\mathrm{HW}}}{\frac{1}{2} g_{\mathrm{HZ}}} \right)^2 = 4 \left(\frac{m_{\mathrm{W}}^2}{m_{\mathrm{Z}}^2} \right)^2 \simeq 2.4 \,.$$

Finally, the EWSB energy scale can be determined from the relation between the v parameter and the Fermi constant G_F:

$$v = \left(\frac{1}{\sqrt{2} G_F} \right)^{\frac{1}{2}} \simeq 246 \text{ GeV}. \tag{1.21}$$

1.3.2 Fermion Masses and Couplings

The Higgs mechanism is also used to generate the fermion masses, by introducing in the SM Lagrangian an $SU(2)_I \otimes U(1)_Y$ invariant term, called *Yukawa term*, which represents the interaction between the Higgs and the fermion fields. Since ϕ is an isodoublet, while the fermions are divided in left-handed doublet and right-handed singlet, the Yukawa terms (one for each fermion generation) must have the following expression for leptons:

$$\mathcal{L}_\ell = -G_{\mathrm{H}\ell} \cdot \overline{l}_\ell \phi \ell_R + \overline{\ell}_R \phi^\dagger l_\ell \,. \tag{1.22}$$

In the unitary gauge, the first component of ϕ is zero, therefore a mass term will arise from the Yukawa Lagrangian only for the second component of l_ℓ: this correctly reproduces the fact that neutrino is (approximately) massless.

$$\mathcal{L}_\ell = -\frac{G_{\mathrm{H}\ell}}{\sqrt{2}} v \bar{\ell}\ell - \frac{G_{\mathrm{H}\ell}}{\sqrt{2}} \mathrm{H} \bar{\ell}\ell \,. \tag{1.23}$$

As far as the quark fields are concerned, the *down* quarks (d, s, b) are treated in the same way as leptons; *up* quarks (u, c, t), instead, must couple to the charge-conjugate of ϕ

$$\phi^c = -i\tau_2 \phi^* = \frac{1}{\sqrt{2}} \begin{pmatrix} \phi^3 - i\phi^4 \\ -\phi^1 + i\phi^4 \end{pmatrix} \tag{1.24}$$

which becomes in the unitary gauge

$$\phi^c = \frac{1}{\sqrt{2}} \begin{pmatrix} \eta + v \\ 0 \end{pmatrix}$$

Therefore, the Yukawa Lagrangian is

$$\mathcal{L}_Y = -G_{\mathrm{H}\ell} \overline{L}_L \phi \ell_R - G_{\mathrm{H}d} \overline{Q}_L \phi d_R - G_{\mathrm{H}u} \overline{Q}_L \phi^c u_R + h.c.\,. \tag{1.25}$$

From Equation 1.23, the mass of a fermion (apart from neutrinos) and its coupling constant to the Higgs boson are found to be

$$m_f = \frac{G_{\mathrm{H}f}}{\sqrt{2}} v \tag{1.26}$$

$$g_{\mathrm{H}f} = \frac{G_{\mathrm{H}f}}{\sqrt{2}} = \frac{m_f}{v} \,. \tag{1.27}$$

Being $G_{\mathrm{H}f}$ free parameters, the mass of the fermions cannot be predicted by the theory.

1.3.3 Higgs Boson Mass

The Higgs boson mass is the only yet unknown free parameter of the SM. The Higgs in fact has never been observed experimentally and its mass cannot be predicted by the SM. It depends on the parameters v and λ, but while the former can be estimated by its relation with the constant G_F of Fermi's theory, the latter is characteristic of the field ϕ and cannot be determined other than measuring the Higgs mass itself. However, both theoretical and experimental constraints exist, including those from direct search at colliders, in particular LEP and Tevatron.

Theoretical Constraints

Theoretical constraints to the Higgs boson mass [8] can be found by imposing the energy scale Λ up to which the SM is valid, before the perturbation theory breaks down and non-SM phenomena emerge. The upper limit is obtained requiring that the running quartic coupling of Higgs potential λ remains finite up to the scale Λ (*triviality*). A lower limit is found instead by requiring that λ remains positive after the inclusion of radiative corrections, at least up to Λ: this implies that the Higgs potential is bounded from below, i.e. the minimum of such potential is an absolute minimum (*vacuum stability*). A looser constraint is found by requiring such minimum to be local, instead of absolute (*metastability*). These theoretical bounds on the Higgs mass as a function of Λ are shown in Figure 1.2 [8]. If the validity

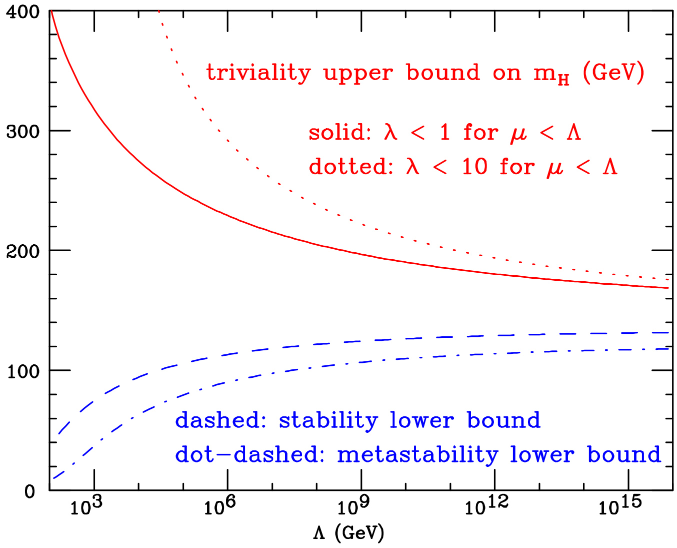

Figure 1.2: *Triviality bound for different upper limits to* λ *(red lines). Vacuum stability (blue dashed line) or metastability (blue dot-dashed line) bounds on the Higgs boson mass as a function of the new physics scale* Λ *[8].*

of the SM is assumed up to the Plank scale ($\Lambda \sim 10^{19}$ GeV), the allowed Higgs boson mass range is between 130 and 190 GeV, while for $\Lambda \sim 1$ TeV the Higgs mass can be up to 700 GeV/c^2. On the basis of these results, the Large Hardon Collider (Section 2.1) is designed for searches of the Higgs boson up to masses of about 1 TeV/c^2. If the Higgs particle is not found in this mass range, then a more sophisticated explanation for the EWSB mechanism will be needed.

Experimental Constraints

Bounds on the Higgs mass are also provided by measurements at LEP [9][10], SLC [11] and Tevatron [12].

Direct searches at LEP-II allowed to set a lower limit of 114.4 GeV/c^2 (95% C.L.) on the Higgs boson mass [13], while recent results from the Tevatron experiments exclude the mass range of 158 to 175 GeV/c^2 (95% C.L.) [14]. Moreover, constraints on the Higgs boson mass can be extracted indirectly from the measurement of other electroweak observables, which have a logarithmic dependence on m_{H} through the radiative corrections [15]. All the precision electroweak measurements performed by the four LEP experiments and by SLD, CDF and D0 [16][17] have been combined together and fitted, assuming the SM as the correct theory and using the Higgs mass as free parameter. The result of this procedure is summarised in Figure 1.3, where the $\Delta\chi^2$ of the fit, defined as $\Delta\chi^2 = \chi^2 - \chi^2_{\mathrm{min}}$, is plotted as a function of m_{H}. The black, solid curve is the result of the fit, while the blue band represents the theoretical uncertainty due to unknown higher order corrections. The yellow area shows the regions excluded by LEP-II and Tevatron measurements. The Tevatron exclusion, in particular, is derived by the results shown in Figure 1.4.

The indirectly measured value of the Higgs boson mass, corresponding to the minimum of the curve in Figure 1.3, is $m_{\mathrm{H}} = 89^{+35}_{-26}$ GeV/c^2, where the errors represent the experimental uncertainty at 68% C.L. derived from the black line, thus not taking the theoretical uncertainty into account. An upper limit of 158 GeV/c^2 can also be set at 95% C.L., including the theoretical uncertainty. This limit increases to 185 GeV/c^2 when including the direct search limit of 114.4 GeV/c^2. These results are model-dependent, as the loop corrections take into account only contributions from known physics, and are thus well-grounded only within the SM theory.

1.4 Higgs Boson Search at the LHC

The experiments at the LHC will search for the Higgs boson within a mass range going from 100 GeV/c^2 to about 1 TeV/c^2. In this section, the main Higgs production and decay processes are described, in order to determine the most promising channels to look at for the Higgs discovery.

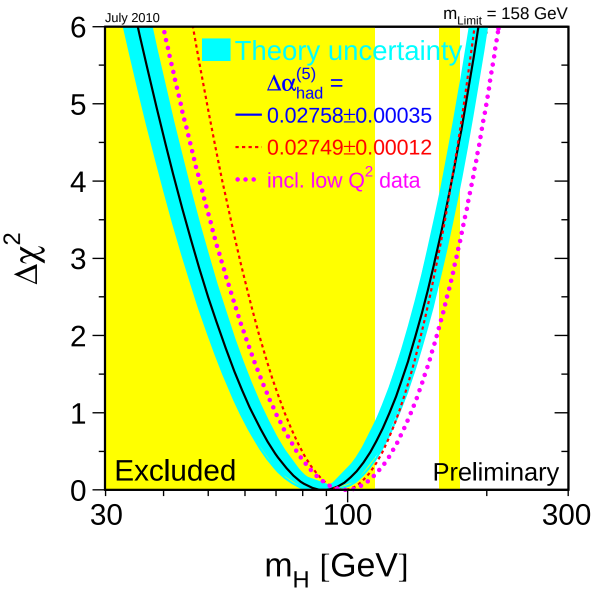

Figure 1.3: $\Delta\chi^2$ *of the fit to the electroweak precision measurements performed at LEP, SLC and Tevatron as a function of the Higgs boson mass (July 2010) [16]. The black, solid line represents the result of the fit, and the blue, shaded band is the theoretical error from unknown higher-order corrections. The yellow area represents the regions excluded by LEP-II and Tevatron.*

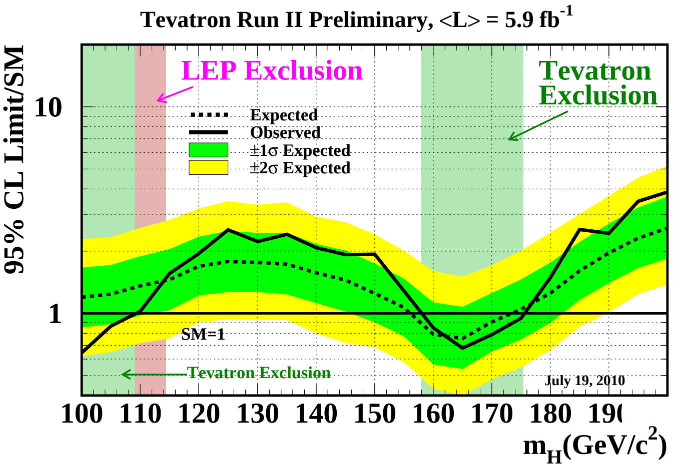

Figure 1.4: *95% C.L. upper limits on the Higgs boson production cross section as a function of the Higgs boson mass. The solid (dashed) line represents the observed (expected) ratio between the excluded cross section and the SM one. The green and yellow bands indicate, respectively, the 68% and 95% probability regions for a fluctuation of the expected limit. The regions in which the line is below 1 represent the mass ranges where the SM Higgs boson can be exluded at 95% C.L. These results are obtained combining CDF and D0 data, for a Tevatron integrated luminosity of 5.9 fb^{-1} (July 2010) [14].*

While the Higgs boson mass is not predicted by the theory, its couplings to fermions and bosons are predicted to be proportional to the corresponding particle masses (for fermions) or squared masses (for bosons), as in Equations 1.19, 1.20 and 1.27. For this reason, the Higgs boson production and decay are dominated by channels involving heavy particles, mainly the $W^{\pm}$ and Z bosons and the third generation fermions. As for the remaining gauge bosons, the Higgs does not couple to photons and gluons at tree level, but only by one-loop graphs where the main contribution is given by $q\bar{q}$ loops for the gg → H channel and by W^+W^- and $q\bar{q}$ loops for the $\gamma\gamma \to$ H channel.

1.4.1 Higgs Production

The main processes contributing to the Higgs boson production at a proton-proton collider are represented by the Feynman diagrams in Figure 1.5, and the corresponding cross sections are shown in Figure 1.6, for centre-of-mass energies of 7 and 14 TeV [18][19]. The former is the energy provided by the LHC during the 2010 runs, the latter is the LHC design energy that will be gradually reached in the next years. Figure 1.5d shows that the total production cross section at 7 TeV is up to one order of magnitude lower than at 14 TeV.

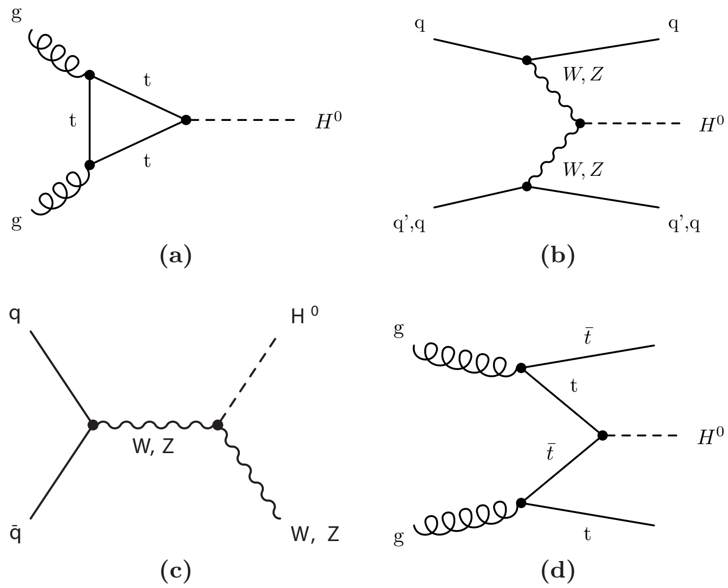

(a) (b)

(c) (d)

Figure 1.5: *Higgs production mechanisms at tree level in proton-proton collisions: (a) gluon-gluon fusion, (b) vector boson fusion, (c)* W *and* Z *associated production (or Higgsstrahlung), and (d)* $t\bar{t}$ *associated production.*

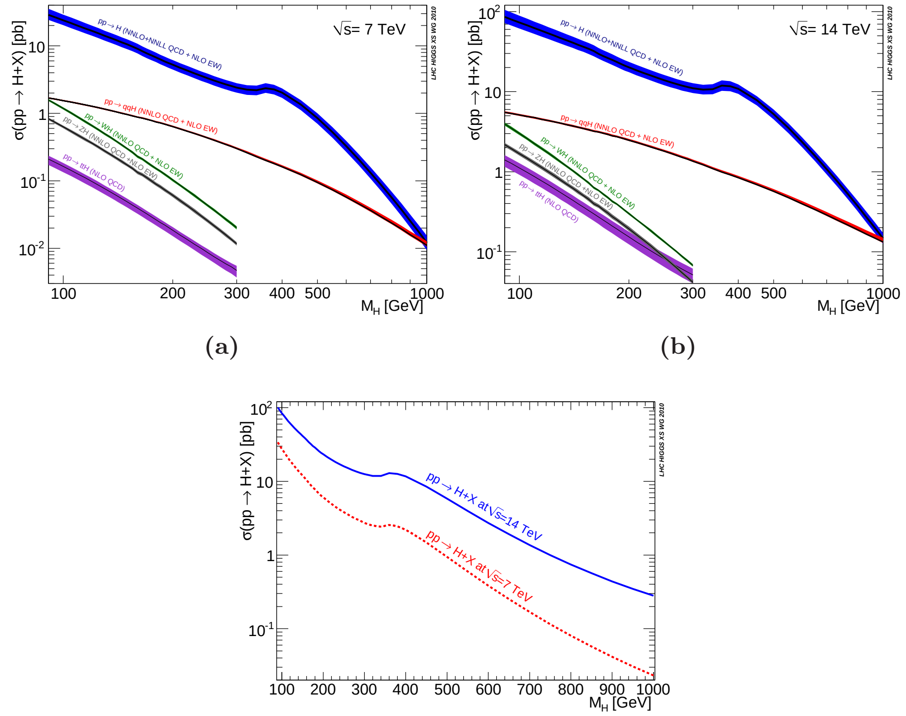

(a) **(b)**

(c)

Figure 1.6: *Cross sections for the different Higgs boson production channels, as functions of the Higgs boson mass, at (a) 7 TeV and (b) 14 TeV LHC centre-of-mass energy. (c) Comparison between the total cross sections at the two different energies. These cross sections include QCD contributions up to NNLO and EW contributions up to NLO.*

Gluon-Gluon Fusion

The gluon-gluon fusion is the dominating mechanism for the Higgs boson production at the LHC over the whole mass range, because of the high luminosity of gluons. The process is shown in Figure 1.5a with a t quark-loop, which is the main contribution, due to the large coupling constant $g_{\mathrm{H}t}$ (Equation 1.27). The latest results in the computation of the cross section for this process, shown in Figures 1.6a and 1.6b and used in Chapter 5 of this thesis, include next-to-next-to-leading order (NNLO) QCD contributions, complemented with next-to-next-to-leading log (NNLL) resummation, and next-to-leading order (NLO) electroweak corrections. An uncertainty of 15-20% on the calulation of this cross section is assumed, mostly depending on the choice of the *parton density functions* (PDFs, *cf.* Section 2.1.3) and on the uncalculated higher-order QCD radiative corrections.

Vector Boson Fusion

The vector boson fusion (VBF, Figure 1.5a) is the second contribution to the Higgs boson production cross section. It is about one order of magnitude lower than gg-fusion for a large range of m_{H} values, and the two processes become comparable only for masses of the order of 1 TeV/c^2. Nevertheless, this channel is very interesting because of its clear experimental signature: the presence of two spectator jets with high invariant mass in the forward region provides a powerful tool to tag the signal events and discriminate the backgrounds, thus improving the signal to background ratio, despite the low cross section. Also for this process, NNLO QCD and NLO EW calculations are available. The uncertainties are in general lower than for the gluon fusion mode, of 10% order.

Associated Production

In the *Higgsstrahlung* process (Figure 1.5c), the Higgs boson is produced in association with a $\mathrm{W}^{\pm}$ or Z boson, which can be used to tag the event. The cross section for this process is several orders of magnitude lower than those of gg-fusion and VBF. The cross section for this process is known at the NNLO QCD and NLO EW level. The inclusion of all available contributions increases the LO cross section by about 20-25%.

The last process, illustrated in Figure 1.5d, is the associated production of a Higgs boson with a $t\bar{t}$ pair. Also for this process, the cross section is orders of magnitude lower than those of gluon and vector boson fusion. The presence of the $t\bar{t}$ pair in the final state can provide a good experimental signature. For this cross section, NLO QCD calculation are available.

1.4.2 Higgs Decay

The branching ratios of the different Higgs boson decay channels are shown in Figure 1.7 as functions of the Higgs mass. Fermion decay modes dominate the branching ratio in the low mass region (up to about 150 GeV/c^2). In particular, the channel $\mathrm{H} \to b\bar{b}$ is the most important contribute, since the b quark is the heaviest fermion available. When the decay channels into vector boson pairs open up, they quickly dominate. A peak in the $\mathrm{H} \to \mathrm{W}^+\mathrm{W}^-$ decay is visible around 160 GeV/c^2, when the production of two on-shell W bosons becomes possible and the production of a real ZZ pair is still not allowed. At high masses, above 350 GeV/c^2, also $t\bar{t}$ pairs can be produced.

The most promising decay channels for the Higgs discovery do not only depend on the corresponding branching ratios, but also on the capability of experimentally detecting the signal rejecting the backgrounds. Such channels are illustrated in the following for different mass ranges.

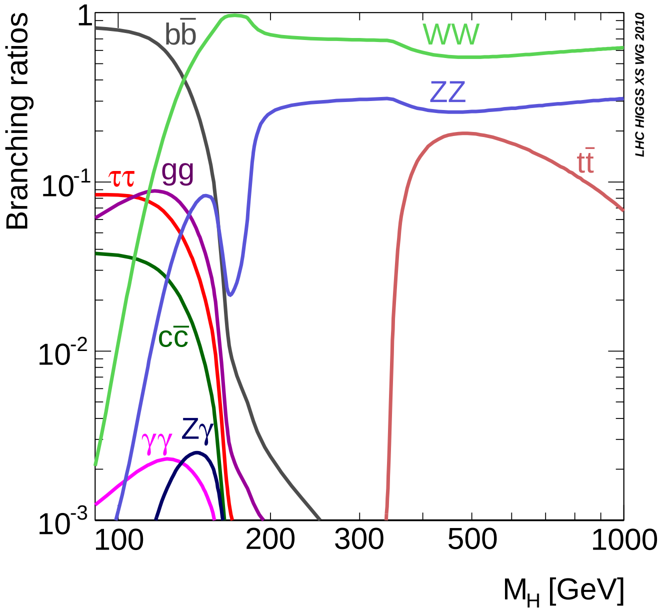

Figure 1.7: *Branching ratio of different Higgs boson decay channels as a function of the Higgs boson mass.*

Low Mass Region

Though the branching ratio in this region is dominated by the decay into $b\bar{b}$, the background constituted by the di-jet production makes it quite difficult to exploit this channel for a discovery. Some results from this channel can be obtained when the Higgs boson is produced in association with a $t\bar{t}$ or via *Higgsstrahlung*, since in this case the event has a clearer signature, despite its low cross section.

For masses below 130 GeV/c^2, instead, the channel $\mathrm{H} \to \gamma\gamma$ seems to be the most promising. In spite of its lower branching ratio, the two high energy photons constitute a very clear signature, which only suffers from the $q\bar{q} \to \gamma\gamma$ and $\mathrm{Z} \to e^+e^-$ backgrounds.

Intermediate Mass Region

For mass values between 140 and 180 GeV/c^2, the Higgs boson decays into $\mathrm{WW}^{(*)}$ and $\mathrm{ZZ}^{(*)}$ open up and their branching ratios quickly increase, so the best channels in this mass region are $\mathrm{H} \to \mathrm{WW}^{(*)} \to 2\ell 2\nu$ and $\mathrm{H} \to \mathrm{ZZ}^{(*)} \to 4\ell$. The branching ratio of $\mathrm{H} \to \mathrm{WW}^{(*)}$ is higher, because of the stronger coupling of the Higgs boson to charged current than to neutral current. Moreover, this decay mode becomes particularly important in the mass region between $2m_{\mathrm{W}}$ and $2m_{\mathrm{Z}}$, where the Higgs boson can decay into two real W's and not yet into two real Z's, and its branching ratio is close to one. On the other hand, this channel is disfavoured because of the presence of the two neutrinos in the final state, which makes it impossible to reconstruct the Higgs mass. Such measurement is possible, instead, if one W decays leptonically and the other one decays into two quarks. In this case, though, the final state suffers from the abundant hadronic background.

The decay channel $\mathrm{H} \to \mathrm{ZZ}^* \to 4\ell$, despite its lower branching ratio, offers a very clear experimental signature and high signal to background ratio. Furthermore, it allows to reconstruct the Higgs mass with high precision. Therefore, this channel is a good candidate for a discovery in this mass range.

High Mass Region

This region corresponds to mass values above the $2m_{\mathrm{Z}}$ threshold, where the Higgs boson can decay into a real ZZ pair. Though the $\mathrm{H} \to \mathrm{ZZ}$ width is still lower than the $\mathrm{H} \to \mathrm{WW}$ one, the decay into four charged leptons (muons or electrons) is certainly the "golden channel" for a high mass Higgs boson discovery.

Higgs Total Decay Width

The total width of the Higgs boson resonance, given by the sum of the partial widths of all possible decay channels, is shown in Figure 1.8 as a function of m_{H}. Below the $2m_{\mathrm{W}}$ threshold, the Higgs boson width is of the order of the MeV/c^2. Then it rapidly increases, but remains below 1 GeV/c^2 up to $m_{\mathrm{H}} \sim 200$ GeV/c^2. The low mass range is therefore the most challenging region, because the Higgs width is dominated by the experimental resolution.

In the high mass region, $m_{\mathrm{H}} > 2m_{\mathrm{Z}}$, the total Higgs boson width is dominated by the $\mathrm{W}^+\mathrm{W}^-$ and ZZ partial widths, which can be written as follows:

$$\Gamma(\mathrm{H}{\to}\mathrm{W}^+\mathrm{W}^-) = \frac{g^2}{64\pi}\frac{m_{\mathrm{H}}^3}{m_{\mathrm{W}}^2}\sqrt{1-x_{\mathrm{W}}}\left(1-x_{\mathrm{W}}+\frac{3}{4}x_{\mathrm{W}}^2\right) \tag{1.28}$$

$$\Gamma(\mathrm{H}{\to}\mathrm{ZZ}) = \frac{g^2}{128\pi}\frac{m_{\mathrm{H}}^3}{m_{\mathrm{W}}^2}\sqrt{1-x_{\mathrm{Z}}}\left(1-x_{\mathrm{Z}}+\frac{3}{4}x_{\mathrm{Z}}^2\right) \tag{1.29}$$

where

$$x_{\mathrm{W}} = \frac{4m_{\mathrm{W}}^2}{m_{\mathrm{H}}^2}\,, \qquad x_{\mathrm{W}} = \frac{4m_{\mathrm{Z}}^2}{m_{\mathrm{H}}^2}\,.$$

As the mass grows, $x_{\mathrm{W}}, x_{\mathrm{Z}} \to 0$ and the leading term in Equations 1.28 and 1.29 grows proportionally to m_{H}^3. Summing over the $\mathrm{W}^+\mathrm{W}^-$ and ZZ channels, the Higgs resonance width in the high mass region can be written

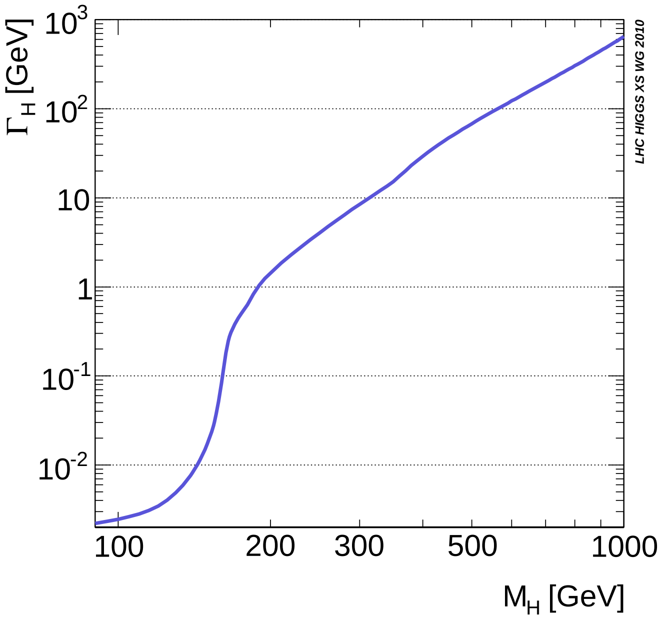

Figure 1.8: *Total decay width of the Higgs boson as a function of its mass.*

as

$$\Gamma(\mathrm{H}\rightarrow\mathrm{VV}) = \frac{3}{32\pi}\frac{m_{\mathrm{H}}^3}{v^2}\,. \tag{1.30}$$

From Equation 1.30, it results that $\Gamma_{\mathrm{H}} \simeq m_{\mathrm{H}}$ for $m_{\mathrm{H}} \simeq 1.4$ TeV/c^2. If m_{H} is larger than about 1 TeV/c^2, therefore, it becomes experimentally very problematic to separate the Higgs resonance from the VV continuum. Actually, being the resonance width larger than its own mass, the Higgs boson cannot be properly considered as a particle any more. In addition, if the Higgs mass is above 1 TeV/c^2, the SM predictions violate unitarity. All these considerations suggest the TeV/c^2 as a limit to the Higgs boson mass: at the TeV scale at least, the Higgs boson must be observed, or new physics must emerge.

1.5 Motivation for the LHC

The discovery of the mechanism that gives origin to the mass of all known particles requires a machine able to span the energy range from about 100 GeV to 1-2 TeV, and to investigate processes with cross sections down to some tens of fb.

The main goal of the LHC project is certainly the search for the SM Higgs boson and the study of its properties, or the investigation of some alternative EWSB mechanism. Other physics motivations for the LHC are summarised in the following.

Physics beyond the SM. There are strong motivations to think that the SM is not the ultimate theory of particle interaction, but only a well tested low energy approximation of some more fundamental theory. One reason is the presence in the SM of "too many" free parameters for a fundamental theory: there are at least 19 of them, 7 more if non-vanishing neutrino masses are assumed, and most of these are introduced by the Higgs mechanism.
A stronger reason is that, unless some fine tuned cancellation took place, the Higgs boson mass suffers from a divergent radiative correction proportional to a high energy cut-off. The presence of new physics, such as the *Supersymmetry* (SUSY), can give physical reasons to the cancellation of the Higgs mass divergent correction (SUSY, on the other hand, introduces even more free parameters than the SM, at least 124, depending on the models).
Moreover, *Grand Unification Theories* (GUTs) predict that the running coupling constants of the three fundamental interactions, extrapolated to a very high energy scale (10^{16} GeV), unify to a single value: this does not occur, unless some new phenomena arise at an intermediate scale. SUSY, e.g., predicts the existence of a number of new particles at the TeV scale, which are thus accessible at the LHC: particles with masses up to 3-5 TeV/c^2 can be observed, depending on the total integrated luminosity.

Precision Measurements. The LHC is a factory of heavy particles, such as W and Z bosons and t and b quarks: the huge amount of events that can be collected, thanks to the high luminosity and centre-of-mass energy, allows all sort of precision measurements: W mass, WWγ and WWZ triple gauge couplings, mass and decay properties of t quarks, measurement of the strong coupling constant α_S, CP violation, and many others.

Heavy ion physics. When running as a heavy ion ($^{208}\mathrm{Pb}^{82+}$) collider, the LHC allows to study the phase transition from hadronic matter to a plasma of deconfined quarks and gluons, the *quark-gluon plasma* or QGP.

Chapter 2

The CMS detector at the LHC

2.1 The Large Hadron Collider

The LHC [20] is an unprecedent machine in terms of energy, luminosity, size and complexity of experiments, cost and human resources.

On 23 November 2009, the accelerator produced the first proton-proton collisions. After few pilot runs at energies of 450 GeV and 1.18 TeV per beam, the energy was ramped up to 3.5 TeV and, on 30 March 2010, the first collisions at a centre-of-mass energy of 7 TeV, the highest ever reached at a particle collider, were recorded by the four main experiments. With this energy, about 47 pb^{-1} of integrated luminosity were delivered during 2010 (see Figure 2.1a), with a maximum instantaneous luminosity of $2 \cdot 10^{32}\ \mathrm{cm}^{-2}\,\mathrm{s}^{-1}$.

In November 2010, the first lead ion beams were circulated in the LHC. In one month, between November and December, about 8 $\mu\mathrm{b}^{-1}$ of Pb-Pb collisions were delivered (see Figure 2.1b), at a centre-of-mass energy of 574 TeV (7 TeV per proton pair, 2.76 TeV per nucleon pair), the highest ever touched in heavy ion experiments.

In the next years, the LHC will progressively increase its energy and instantaneous luminosity, reaching eventually the design values of 14 TeV, 7 times the highest energy reached so far at Tevatron, and $10^{34}\ \mathrm{cm}^{-2}\,\mathrm{s}^{-1}$, about two orders of magnitude more than the luminosity of previous machines. The design lifespan of LHC is of 10 years.

2.1.1 The Accelerator

The LHC is placed in the already existent 26.7 km long LEP tunnel, situated about 100 m depth underground on the French-Swiss border. The main design characteristics of the machine are listed in Table 2.1.

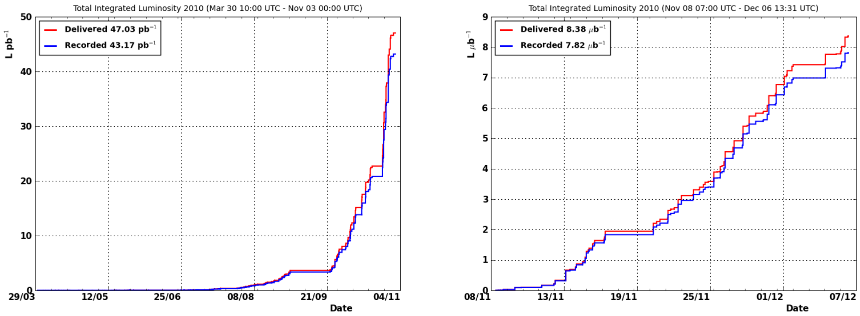

(a) **(b)**

Figure 2.1: *Integrated luminosity delivered by the LHC (in red) and recorded by CMS (in blue) in (a) proton-proton and (b) lead-lead collisions.*

Parameter	p-p	Pb-Pb
Circumference [km]	26.659	
Beam radius at interaction point [μm]	15	
Dipole peak field [T]	8.3	
Design centre-of-mass energy [TeV]	14	1148
Design Luminosity [$\text{cm}^{-2}\,\text{s}^{-1}$]	10^{34}	$2 \cdot 10^{27}$
Luminosity lifetime [h]	10	4.2
Number of particles per bunch	$1.1 \cdot 10^{11}$	$\sim 8 \cdot 10^{7}$
Number of bunches	2808	608
Bunch length [mm]	53	75
Time between collisions [ns]	24.95	$124.75 \cdot 10^{3}$
Bunch crossing rate [MHz]	40.08	0.008

Table 2.1: *LHC design parameters for p-p and Pb-Pb collisions.*

Since collisions occur between particles of the same charge, two separate acceleration cavities with two different magnetic field configurations are required. The bending power needed to keep the beam circulating is the limiting factor to the achievable centre of mass energy. In fact, from the equation

$$p\,[\text{TeV}/c] = 0.3 \cdot B\,[\text{T}] \cdot \rho\,[\text{km}]\,,$$

where p is the beam momentum, B the magnetic field and ρ the radius of the ring, one can deduce that the bending power required for $p = 7$ TeV/c is about 5.4 T. In practice, since it is not possible to fill the whole machine with magnets, the needed power is obtained by using about 1200 superconducting dipoles operating at 1.9 K, each providing a field of about 8.3 T. Boosts will be given by 400 MHz superconducting radiofrequency cavities with a voltage ranging between 8 and 16 MV. The channels for the two beams acceleration are inserted in a single cryostat.

The event rate R of a process with cross section σ is given by

$$R = \mathcal{L} \cdot \sigma ,$$

where $\mathcal{L}$ is the instantaneous luminosity of the machine, defined as the number of collisions per unit time and cross-sectional area of the beams [21]:

$$\mathcal{L} = f \frac{n_1 n_2}{4\pi\sigma_x\sigma_y} ;$$

σ_x and σ_y characterise the Gaussian transverse beam profiles in the horizontal and vertical directions.

Cross sections and event rates for the main processes produced at the LHC are reported in Figure 2.2 as functions of the centre-of-mass energy. The high LHC luminosity, already mentioned in previous sections, is a fundamental requirement to compensate for the low Higgs boson production cross sections. Such luminosity has the drawback that the total event rate becomes so high that several interactions overlap in the same bunch crossing. This effect is referred to as *pile-up*, and also accounts for the overlap in the detector of signals from different bunch crossings, due to the limited velocity of detector response and read-out. At the design luminosity, about 20 interactions per bunch crossing will occur.

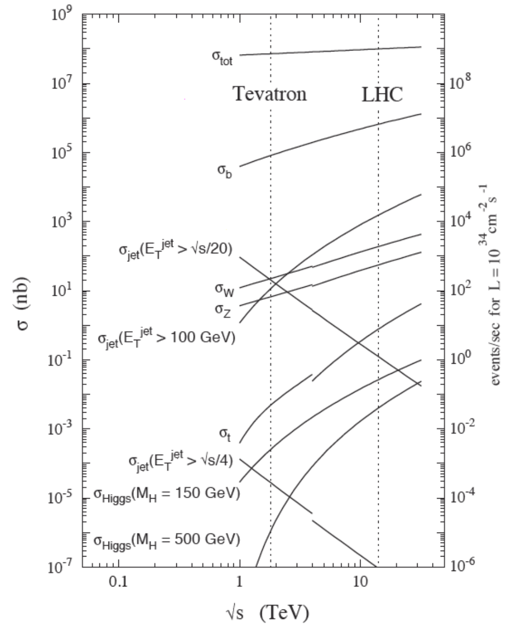

Figure 2.2: *Cross sections and event rates of several processes as functions of the centre-of-mass energy of p-p collisions. The LHC design luminosity is considered.*

2.1.2 Definition of Kinematic Variables

Before proceeding, it is useful to introduce some general definitions and variables, largely used to describe the phenomenology at hadron colliders.

As will be shown in Section 2.2 and in Figure 2.4 for the case of CMS, the kinematics of the particles produced in collisions can be described by means of a Cartesian reference frame, centered in the interaction point and with the z axis tangent to the beam line. The x axis is chosen to be horizontal and pointing towards the centre of the ring, and the y axis is vertical and pointing upwards. The direction of the z axis, i.e. the direction of the beam, is referred to as *longitudinal*. The x-y plane, orthogonal to the beam line, is called *transverse* plane.

Based on these definitions, the momentum of a particle can be divided in two components: the *longitudinal momentum* p_z and the *transverse momentum* p_{T}, defined as

$$p_{\mathrm{T}} = \sqrt{p_x^2 + p_y^2}\,. \tag{2.1}$$

The *rapidity* of a particle of energy E is defined as

$$y = \frac{1}{2}\ln\frac{E + p_z}{E - p_z}\,. \tag{2.2}$$

Rapidity has the property of being *additive* under Lorentz boosts along the z direction, i.e. it is simply shifted by a constant when subjected to such transformations. For high energy particles, rapidity can be approximated by *pseudorapidity*

$$\eta = -\ln\left(\tan\frac{\theta}{2}\right)\,, \tag{2.3}$$

which only depends on the polar angle θ of the particle momentum, i.e. its angle with respect to the z axis.

2.1.3 Phenomenology of Proton-Proton Collisions

At the nominal centre of mass energy of 14 TeV, the total inelastic proton-proton cross section σ_{pp} is about 80 mb, therefore an interaction rate of about 10^9 Hz is foreseen. These events include two classes of interaction:

- soft collisions: large distance collisions between two incoming protons, in which only a small momentum is transferred; particle scattering at large angle is thus suppressed, and the final state particles have small transverse momentum, $\langle p_{\mathrm{T}} \rangle \simeq 500$ MeV/c, so that most of them escape down the beam pipe;

- hard collisions: since protons are not elementary particles, occasionally collisions with high transferred p_{T} occur between two of their constituents (*partons*, i.e. quarks and gluons). These interactions represent the interesting physics events, where massive particles may be created. The rate of hard interactions, though, is several orders of magnitude lower than that of soft interactions.

In hard interactions, the *effective* centre-of-mass energy $\sqrt{\hat{s}}$, i.e. the centre-of-mass energy of the two interacting partons, is proportional to the fractions x_a and x_b of proton energy carried by the two partons:

$$\sqrt{\hat{s}} = \sqrt{x_a\, x_b\, s}\,,$$

where $\sqrt{s}$ is the centre-of-mass energy of the proton beams. The distributions of the fractional momentum of partons inside the protons are called *parton distribution functions* (PDFs). They are different for each type of parton and are functions of the exchanged momentum, Q^2. At high Q^2, the contribution of gluons and sea quarks increases with respect to that of valence quarks. PDFs are measured in Deep Inelastic Scattering (DIS) experiments and different models are available. In Figure 2.3, for example, the CTEQ4M PDFs [22] are shown for two different values of Q^2.

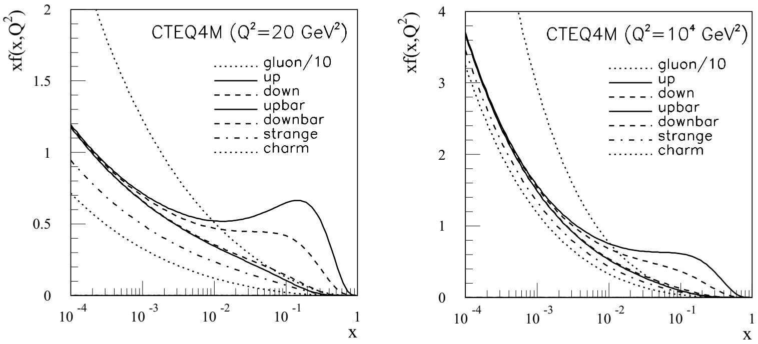

Figure 2.3: *CTEQ4M PDFs for* $Q^2 = 20\,\mathrm{GeV}^2/c^2$ *(left) and* $Q^2 = 10^4\,\mathrm{GeV}^2/c^2$ *(right).*

The event reconstruction is limited by the fact that the two interacting partons have variable and unknown momenta, so no constraints can be applied on the total momentum of final state particles. Assuming that the transverse momenta of partons are negligible, though, the total transverse momentum in the final state must be zero. The longitudinal momentum, instead, remains unconstrained.

Another important consequence is that the centre of mass of the interaction may be boosted along the beam direction. For this reason, it is necessary to use quantities which have invariance properties under boosts along this direction, such as the transverse momentum (Equation 2.1) and the rapidity (Equation 2.2). Given the high energy of the particles under study, rapidity is usually replaced by pseudorapidity (Equation 2.3).

Particles produced in soft collisions are mostly distributed at high rapidity. However, the soft interaction rate is so large that the residual tail at high p_{T} is competitive with the hard interaction rate, and constitutes a background to high p_{T} signal events.

2.2 The CMS Experiment

The Compact Muon Solenoid (CMS) [23][24] is one of the two general purpose detectors which will operate at LHC. Its physics goals range from the search for the Higgs boson to the searches for new physics beyond the SM and to precision measurements of already known physics. To achieve these goals, excellent lepton reconstruction and particle identification are required. The main features of the CMS detector are the 4 T superconducting solenoid, which allows a compact design with a strong magnetic field, a robust and redundant muon system, a good electromagnetic calorimetry and a high quality tracking system.

The overall structure of CMS consists of several cylindrical layers coaxial to the beam axis (the *barrel layers*), closed at both ends by detector disks orthogonal to the beam direction (the *endcaps*), to ensure an optimal hermeticity. The overall length is 21.6 m, the diameter 14.6 m and the total weight about 14 500 t. Schematic views of the CMS detector are shown in Figures 2.5 and 2.6.

The CMS coordinate system (see Figure 2.4) used to describe the detector geometry is a right-handed Cartesian frame, with the z axis coincident with the beam direction, the z axis pointing to the centre of the LHC ring and the y axis directed upwards. Because of the cylindrical symmetry of the CMS design, the reconstruction algorithms use a cylindrical coordinate system (r, ϕ, η), r being the distance from the z axis, ϕ the azimuthal coordinate with respect to the x axis, and η the pseudorapidity defined by Equation 2.3.

As already mentioned, the core of the apparatus is the magnet, which contains, from inside out, the following detectors:

- the *tracker*, made of a silicon *pixel detector* in the inner region, closest to the beam, and of silicon *microstrip detectors* in the outer region, used to reconstruct charged particle tracks and primary and secondary interaction vertices;

- the *electromagnetic calorimeter* (ECAL), which allows for precise measurement of electron and photon energies; it is made of lead tungstate ($\mathrm{Pb\,W\,O_4}$) scintillating crystals, both in the barrel and in the endcaps, and extended by a forward *preshower detector*;

- the *hadron calorimeter* (HCAL), used for jet direction and transverse energy measurements, extended in the forward region with the *“very forward calorimeter”*.

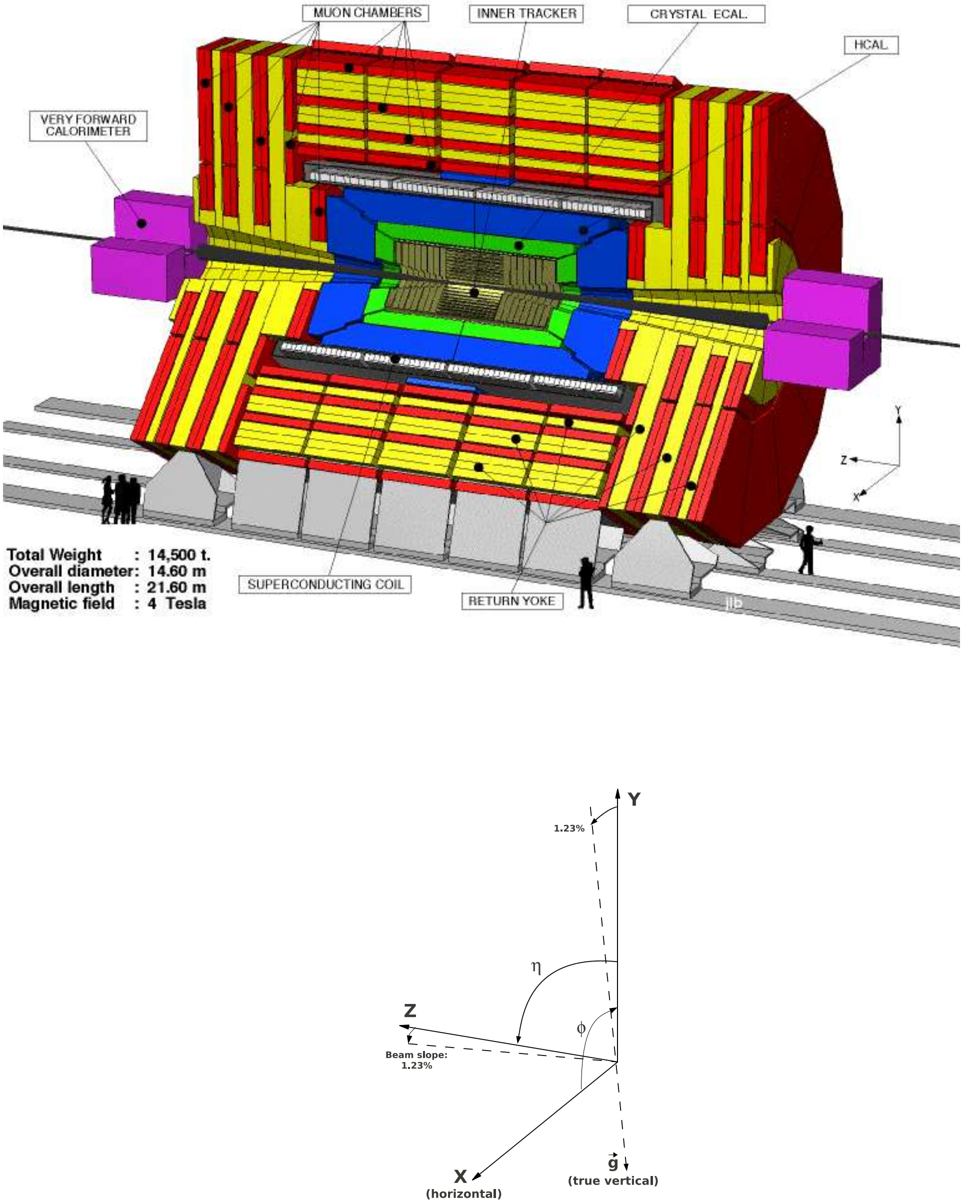

Figure 2.4: *A three dimensional view of the CMS detector with the conventional coordinate system.*

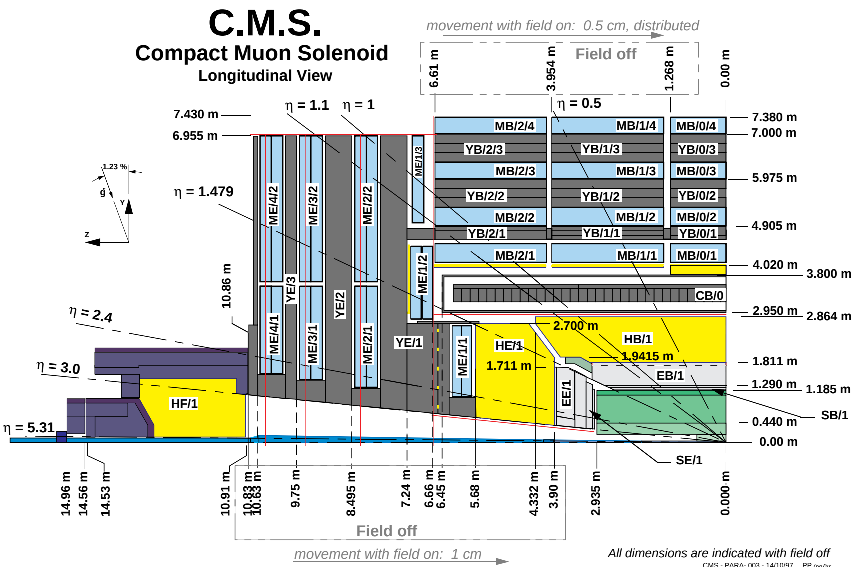

Figure 2.5: *Longitudinal view of one quarter of the CMS detector.*

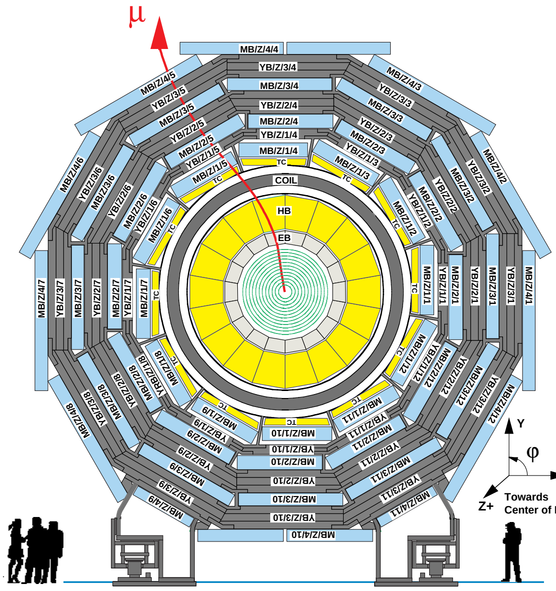

Figure 2.6: *A transverse view of the CMS barrel region.*

Outside the magnet coil, the iron return yoke of the magnet hosts the *muon spectrometer*, used for reconstruction of muon tracks: *drift tubes* (DT) in the barrel and *cathode strip chambers* (CSC) in the endcaps, complemented overall by *resistive plate chambers* (RPC), to ensure redundancy and robustness to the muon trigger.

2.2.1 The Magnet

The CMS magnet [25] is a 13 m long superconducting solenoid, the largest ever built. It is able to generate a uniform magnetic field of 4 T in the inner region, storing about 2.5 GJ of energy (Figure 2.7).

It operates at a temperature of 4 K, ensured by a sophisticated helium cooling system. At such temperature, the flat Ni Tb cable becomes superconducting, allowing a 20 kA current to flow without appreciable loss. The whole magnet is then contained in an enormous vacuum cylinder, which isolates it from the external environment.

Outside, an iron structure composed by five barrel layers and three disks for each endcap constitutes the iron yoke, needed to bridle the return magnetic field, which otherwise would get lost, causing disturbances.

The CMS magnet provides a large bending power, allowing a precise measurement of the transverse momentum of charged particles. A further and independent p_{T} measurement outside the solenoid is possible thanks to the iron yoke, which surrounds the muon chambers.

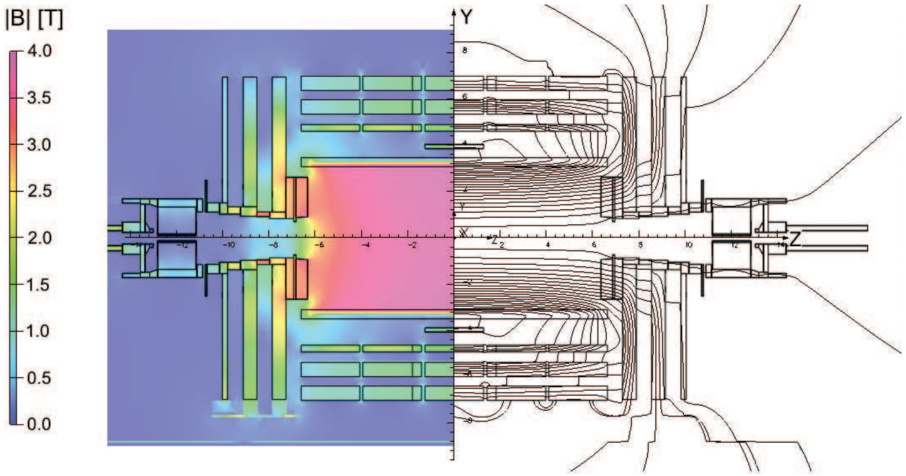

Figure 2.7: *Layout of the magnetic field of CMS [26].*

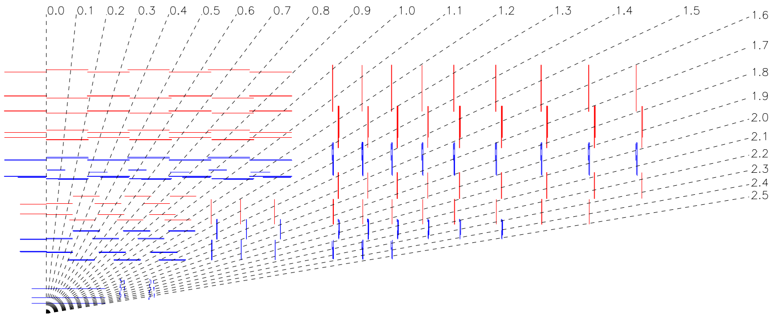

Figure 2.8: *Longitudinal view of one quarter of the silicon tracker, including the pixel detector.*

2.2.2 The Tracker

The tracker [27] (see Figure 2.8), which is the innermost subdetector and the closest to the interaction point, is dedicated to track and vertex reconstruction. It extends in the region $|\eta| < 2.5$, $r < 120$ cm, $|z| < 270$ cm, and it is completely based on silicon detectors, covering a surface of 210 m^2, the largest ever designed for detectors of this kind.

The CMS tracker has to satisfy some important physics requirements:

- an efficient reconstruction of isolated lepton tracks: in the $|\eta| < 2$ region, the efficiency is close to 100% (Figure 2.9a);

- a good lepton momentum resolution: for $|\eta| < 2$, $\sigma(p_{\mathrm{T}})/p_{\mathrm{T}} < 4\%$ for single muons in a large range of p_{T} values (Figure 2.9b and also Sections 4.2.4 and 4.3.2);

- reconstruction of interaction vertex and identification of secondary vertices (Figures 2.9c and 2.9d): this task is essential for tagging and reconstruction of b-jets and, therefore, for top physics, CP violation and new physics studies.

In order to fulfill all these tasks and perform a good pattern recognition, two main properties have driven the tracker design:

- low cell occupancy: this requires high granularity detectors, especially those closer to the interaction point, and fast primary charge collection, obtained by using thin detectors and overdepleting the silicon bulks;

- large hit redundancy: ten layers of silicon detectors provide many measured hits (12-14) per track.

These properties allow for a high tracking efficiency and a low rate of fake tracks.

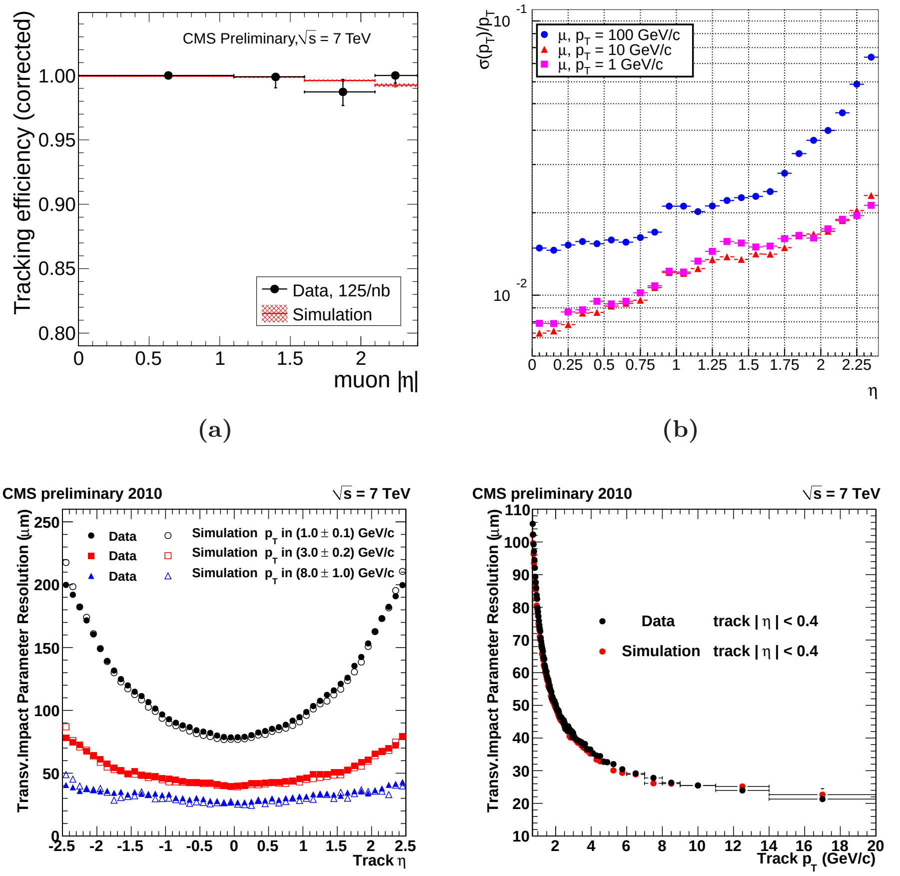

(a) **(b)**

(c) **(d)**

Figure 2.9: *(a) Tracking efficiency vs. $|\eta|$, in data and simulation, estimated using the tag-and-probe method with muons from J/ψ decays [28]. (b) Transverse momentum resolution vs. $|\eta|$ for simulated muons with $p_{\mathrm{T}} = 1$, 10 and 100 GeV/c. (c) Transverse impact parameter resolution vs. $|\eta|$, in data and simulation, for different muon momenta. (d) Transverse impact parameter resolution vs. p_{T}, in data and simulation, for $|\eta| < 0.4$ [29].*

Moreover, several material budget constraints are imposed by the necessity to minimise electron *bremsstrahlung* and hadronic interactions, not to degrade tracking and ECAL performances. The region with the highest amount of material is the transition region between barrel and endcap ($1 < |\eta| < 2$), due to the high density of cables.

Finally, both pixel and microstrip detectors have to be kept at a working temperature of -10 °C for the whole tracker volume, in order to limit the radiation damage to silicon sensors, due to the high flux of hadrons and backscattered neutrons[1].

Pixel Detector

The pixel detector (Figure 2.10) consists of three barrel layers and two endcap disks for each side. The barrel layers, 53 cm long, are placed at $r = 4.4$, 7.3 and 10.2 cm. The first layer will be replaced by an outer layer at $r = 13$ cm during the high luminosity phase, to reduce the radiation damage. The two disks of each endcap consist of 24 blades, arranged in a turbine-like shape, having the inner radius of 6 cm and the outer of 15 cm. The total area covered with pixels is about 0.92 m^2.

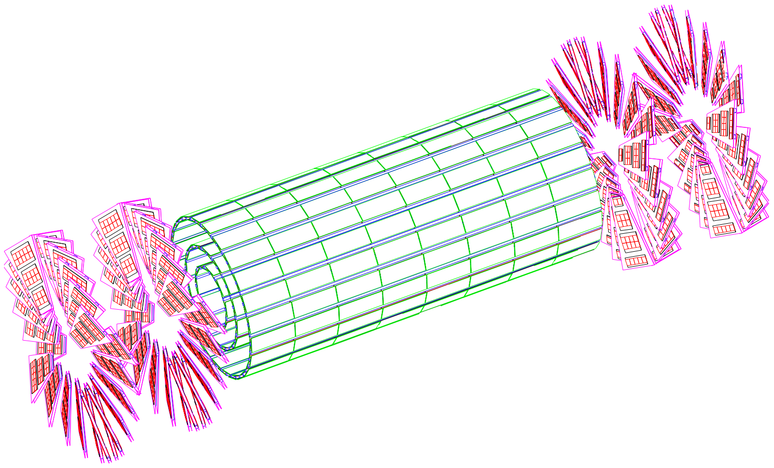

Figure 2.10: *The pixel detector. The barrel section and the two disks of the endcaps are visible.*

The inner detector provides at least two hits for tracks originating within $2\,\sigma_z$ from the nominal interaction vertex, in the pseudorapidity region $|\eta| < 2.2$. Due to the high density of tracks, 100×150 μm^2 pixels are used to ensure low cell occupancy. A spatial resolution of about 10 μm in the r-ϕ plane and 15 μm in the z coordinate can be achieved in the barrel, about 15 μm and 20 μm respectively in the endcaps.

---

[1] Backscattering of neutrons from nuclear interactions in the material of ECAL.

Silicon Microstrip Detector

The silicon microstrip detector is divided in two main regions. The inner region is made of 4 barrel layers (*tracker inner barrel* or TIB) and 3 disks at each side (*tracker inner disks* or TIDs). The outer system, instead, consists of 6 barrel layers (*tracker outer barrel* or TOB) and 9 disks for each endcap (*tracker endcaps* or TECs). It covers a radial region between 20 and 120 cm and the pseudorapidity region $|\eta| < 2.5$.

All four regions (TIB, TID, TOB, TEC) are provided with both single-sided and double-sided microstrip modules. The strips are oriented along the z direction in the barrel and along the r coordinate in the endcaps. The microstrip detector is designed to provide a spatial resolution of about 40-60 μm in the r-ϕ plane and about 500 μm along z. The occupancy is lower than 1%.

2.2.3 The Electromagnetic Calorimeter

The electromagnetic calorimeter (ECAL) [30] is made of 74 848 lead tungstate ($PbWO_4$) crystals, chosen because of their excellent energy resolution.

The lead tungstate is characterised by a high density (8.28 g/cm^3) and a short radiation length ($X_0 = 0.89$ cm), so the calorimeter is very compact and can be placed inside the magnetic coil. Furthermore, it has a small Molière radius (2.2 cm), which gives the ECAL a very fine granularity, needed because of the high particle density produced at the LHC. Moreover, these crystals are characterised by a very short scintillation decay time, which allows to collect about 80% of the light within 25 ns, so that they can be used at the crossing rate of 40 MHz.

The ECAL barrel covers the central rapidity region ($|\eta| < 1.48$) and the two ECAL endcaps extend the coverage up to $|\eta| = 3$ (Figure 2.11).

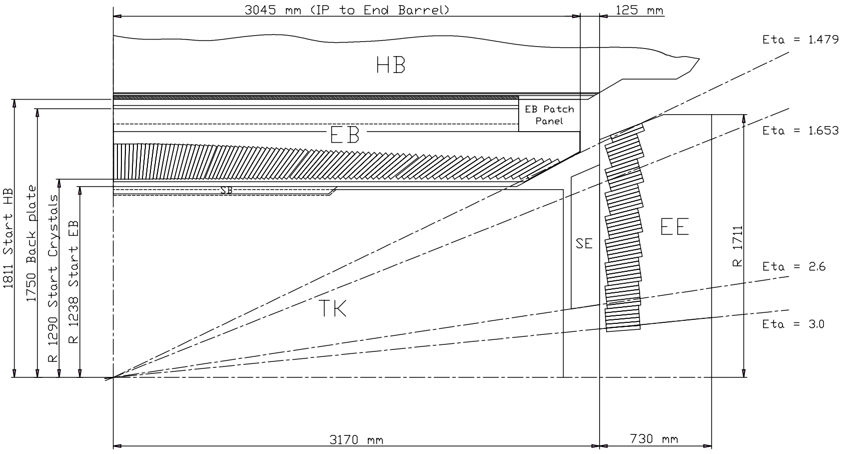

Figure 2.11: *Longitudinal view of one quarter of the CMS ECAL.*

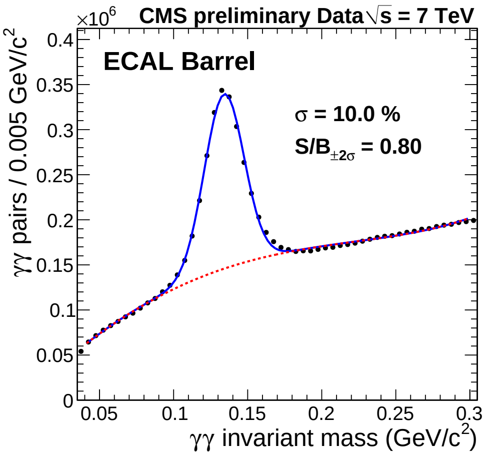

Figure 2.12: *Di-photon invariant mass spectrum reconstructed by ECAL with about 250 nb^{-1} of data at 7 TeV. The π^0 peak is visible. The mass resolution is of the order of 10%.*

The crystals have a trapezoidal shape and are arranged in a η-ϕ grid in the barrel and a x-y grid in the endcaps. The barrel crystals have a front face area of 2.2 × 2.2 cm^2 (thus matching the Molière radius), 23 cm length and are positioned at $r = 1.29$ m. Hence the total depth of ECAL barrel is $25.8\,X_0$, and the transverse granularity is $\Delta\eta \times \Delta\phi = 0.0175 \times 0.0175$ rad. In the endcaps, crystals have 2.47 × 2.47 cm^2 front face, 22 cm length (corresponding to $24.7\,X_0$) and are positioned at $z = 3.17$ m. Both in the barrel and in the endcaps, the crystals are tilted of about 3° in η and in ϕ, thus giving the structure a geometry slightly off-pointing from the interaction region, in order to improve the hermeticity of the detector.

For trigger purposes, the ECAL crystals are grouped together into 68 *trigger towers*, whose boundaries line up with the subdivisions of the HCAL.

In the endcaps, a *preshower* device with higher granularity, consisting of two lead radiators and two planes of silicon strip detectors, are used to distinguish between showers initiated by neutral pions and photons, or charged pions and electrons.

The relatively low light yield of the crystals (about 30 γ/MeV) requires photodetectors with intrinsic high gain that can operate in a magnetic field. Silicon Avalanche Photodiodes (APDs) and Vacuum Phototriodes (VPTs) are used to collect the scintillation light in the barrel and in the endcaps, respectively.

The energy resolution of a calorimeter can be parametrised as

$$\left(\frac{\sigma}{E}\right)^2 = \left(\frac{a}{\sqrt{E}}\right)^2 + \left(\frac{\sigma_n}{E}\right)^2 + c^2$$

where a is called stochastic term and includes the effects of fluctuations in the number of photo-electrons, as well as in the shower containment; σ_n is the noise from the electronics and pile-up; and c is a constant term related to the calibration of the calorimeter. The values of the three constants measured on test beams are reported in Table 2.2. The different contributions are shown in Figure 2.13.

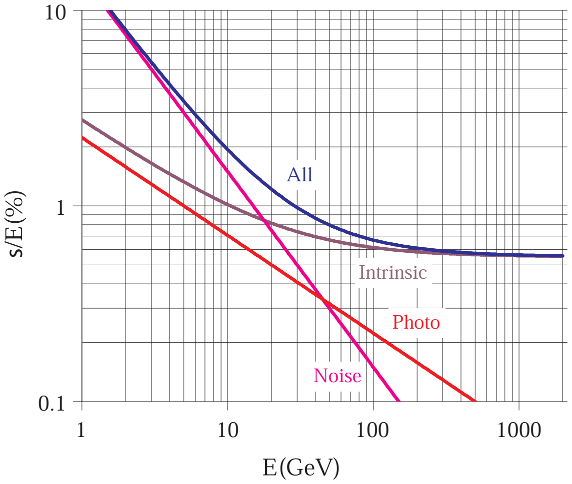

Figure 2.13: *Different contributions to the energy resolution of the ECAL. The curve labelled "intrinsic" includes the shower containment and a constant term of 0.55%.*

Contribution	Barrel (η =0)	Endcap ($\lvert\eta\rvert$ =2)
Stochastic term	$2.7\%/\sqrt{E}$	$5.7\%/\sqrt{E}$
Constant term	0.55%	0.55%
Noise (high luminosity)	0.155 GeV	0.205 GeV
Noise (low luminosity)	0.210 GeV	0.245 GeV

Table 2.2: *Contribution to the energy resolution of ECAL (the energy E is expressed in GeV).*

2.2.4 The Hadronic Calorimeter

The hadronic calorimeter (HCAL) [31] plays an essential role in the identification and measurement of hadrons and neutrinos by measuring the energy and direction of jets and missing transverse energy flow in the event. One of the main design requirements for the HCAL is therefore a high hermeticity. In particular, the HCAL angular coverage must include the very forward region, since the identification of forward jets is very important for the rejection of many backgrounds.

The CMS HCAL is thus subdivided in four regions, which provide a good segmentation, a moderate energy resolution and a full angular coverage up to $|\eta| = 5$. The *barrel hadronic calorimeter* (HB) surrounds the electromagnetic calorimeter and covers the central pseudorapidity region up to $|\eta| = 1.3$. The end regions are covered up to $|\eta| = 3$ by the two *endcap hadron calorimeters* (HE). The HB and HE are located inside the solenoid magnet. To satisfy the hermeticity requirements, then, two *forward hadronic calorimeters* (HF) surround the beam pipe at $|z| = 11$ m, extending the pseudorapidity coverage up to $|\eta| = 5$. Finally, an array of scintillators located outside the magnet, which is referred to as the *outer hadronic calorimeter* (HO), is used to improve the central shower containment.

The overall HCAL is assembled with essentially no uninstrumented cracks or dead areas. Even the gap between the HB and the HE, through which the services and cables of the ECAL and the tracker pass, is inclined at 53° and points away from the centre of the detector.

The HB and HE are sampling calorimeters with active plastic scintillators interleaved with brass plates. This absorber material has been chosen because of its reasonably short interaction length. Moreover, it is non-magnetic.

The read-out system is composed of wavelength-shifting fibres. Apart from the first layer, which is read out separately, all the other layers are read out together in towers of $\Delta\eta \times \Delta\phi = 0.087 \times 0.087$ rad.

The HCAL depth, in terms of nuclear absorption length, goes from $5.15\,\lambda_0$ at $\eta = 0$ to $9.1\,\lambda_0$ at $|\eta| = 1.3$, and is $10.5\,\lambda_0$ in the endcaps. In the barrel region, such depth is not enough to contain the full shower. This is the reason why an additional "tail catcher", the HO, is placed outside the magnet.

The energy resolution (epressed in GeV) is

$$\sigma_E/E \ \sim \ 65\%\sqrt{E} \oplus 5\%$$

in the barrel,

$$\sigma_E/E \ \sim \ 85\%\sqrt{E} \oplus 5\%$$

in the endcaps, and

$$\sigma_E/E \ \sim \ 100\%\sqrt{E} \oplus 5\%$$

in the very forward calorimeter.

2.2.5 The Muon System

The muon spectrometer [32] is placed outside the magnet and is embedded in the iron return yoke (see Figure 2.14), so that the 1.8 T average magnetic return flux can be used as bending field to enhance muon p_{T} measurements.

The muon spectrometer has three purposes:

- muon identification: muons are the only charged particles which can go through the whole detector, thanks to their high penetrating power;

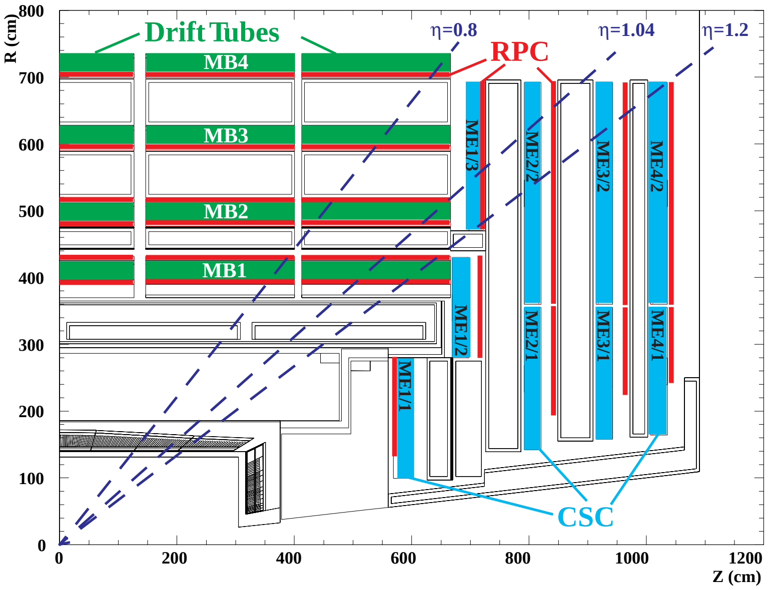

Figure 2.14: *Longitudinal view of one quarter of the CMS muon spectrometer.*

- muon trigger: high p_{T} muons provide a clear signature for many physics processes;
- muon momentum measurement: in combination with the tracker, the muon spectrometer is used to determine muon p_{T}.

Both the barrel and the endcaps of the muon system are made up of four stations. Three different and complementary detection technologies have been used: the barrel muon system uses *drift tube chambers* (DTs), while the endcaps use *cathode strip chambers* (CSCs); in both regions, the tracking detectors are complemented with the use of *resistive plate chambers* (RPCs). The reason for these different choices lies in the different particle rates and occupancies, both higher in the endcaps, and in the intensity of the magnetic field, lower in the barrel.

Drift Tubes Chambers

In the barrel region, the expected occupancy is low (< 10 Hz/cm^2), allowing for the use of drift tubes as detection element. In Figure 2.15, a section of a drift tube cell is illustrated.

The DT chamber design is very redundant: each chamber is made up of twelve layers of DTs, grouped in three independent subunits, called *superlayers* (SLs). Two of them have the anode wires parallel to the beam axis, to measure the transverse coordinate r-ϕ; the remaining SL is placed between the other two and is orthogonal to them, in order to determine

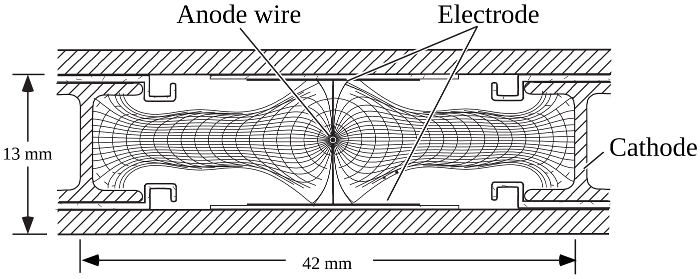

Figure 2.15: *Section of a drift tube cell.*

the longitudinal coordinate z. The structure of a DT chamber is shown in Figure 2.16.

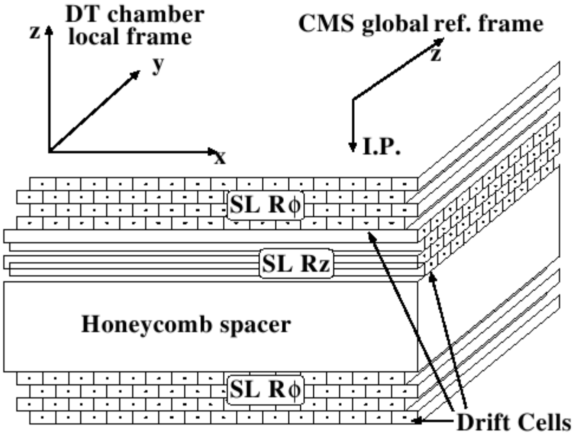

Figure 2.16: *Schematic view of a DT chamber, also showing the different orientation of the SLs.*

The DTs are made of parallel aluminium plates, with cells obtained with perpendicular “I” shaped aluminium cathodes. The anodes are 50 μm diameter steel wires placed between the cathodes. Field shaping is improved with two biased and insulated strips in correspondence to the wire. The internal volume is filled with a gas mixture of Ar (85%) and CO_2 (15%) at atmospheric pressure, because this gas is non-flammable and can be safely used in underground operations in large volumes, as required in CMS.

The single hit position resolution is about 260 μm at nominal voltage values, with a single cell efficiency close to 100%. The angular resolution of the full chamber is about 1.8 mrad in the bending plane [33].

Cathode Strip Chambers

Due to the larger occupancy of the endcap regions, from few Hz/cm^2 to more that 100 Hz/cm^2, and the intense and non uniform magnetic field, cathode strip chambers have been chosen in this region. The CSCs are multiwire proportional chambers with one cathode plane segmented in strips running orthogonal to the wires. An avalanche developed on a wire induces a distributed charge on the cathode plane. The orthogonal orientation of the cathode strips with respect to the wires allows the determination of two coordinates from a single plane (see Figure 2.17). Each chamber is formed by six trapezoidal layers, with strips in the radial direction for a precise measurement of the azimuthal coordinate ϕ.

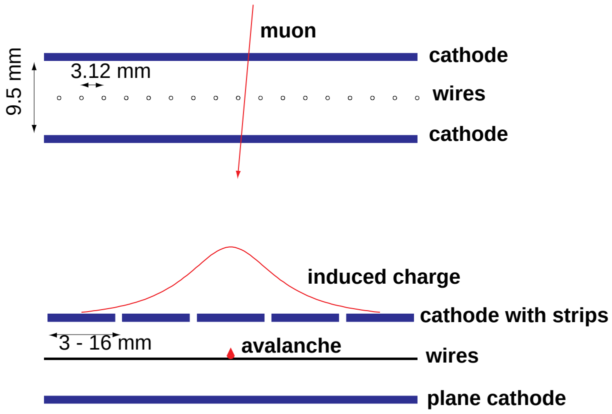

Figure 2.17: *Orthogonal sections of a cathode strip chamber.*

Wires have a resolution of about 0.5 cm, strips about 50 μm. The full chamber spatial resolution varies from about 50 μm in the first CSC station to about 250 μm in the fourth [34].

Resistive Plate Chambers

Resistive plate chambers are installed both in the barrel and the endcap regions. They have a limited spatial resolution, but an excellent time resolution, thanks to their fast response of about 3 ns. This feature makes the RPCs suitable for trigger purposes: they are used as a dedicated trigger subsystem, mainly for unambiguous bunch crossing identification.

The RPCs (Figure 2.18) used in CMS are “double-gap” RPCs, made of four bakelite planes forming two coupled gaps 2 mm thick, filled with a $C_2H_2F_4$ and C_4H_{10} gas mixture. They operate in avalanche mode: a moderate electric field across the gap allows to sustain a higher rate, but a robust front-end signal amplification is needed, since the gas multiplication is reduced.

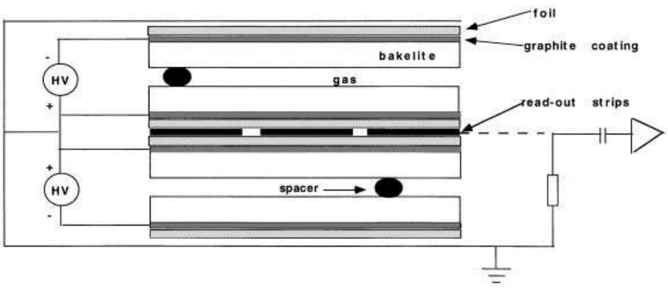

Figure 2.18: *Section of a double gap resistive plate chamber.*

2.2.6 The Trigger System

At the nominal luminosity of 10^{34} cm^{-2} s^{-1}, an average of 17 interactions per bunch crossing are expected, resulting in an event rate of 10^9 Hz. Technical difficulties in handling, storing and processing extremely large amounts of data impose a limit of about 100 Hz on the rate of events that can be written to permanent storage. The goal of the CMS trigger system is therefore to reduce the data by a factor of 10^7 (see Figure 2.19).

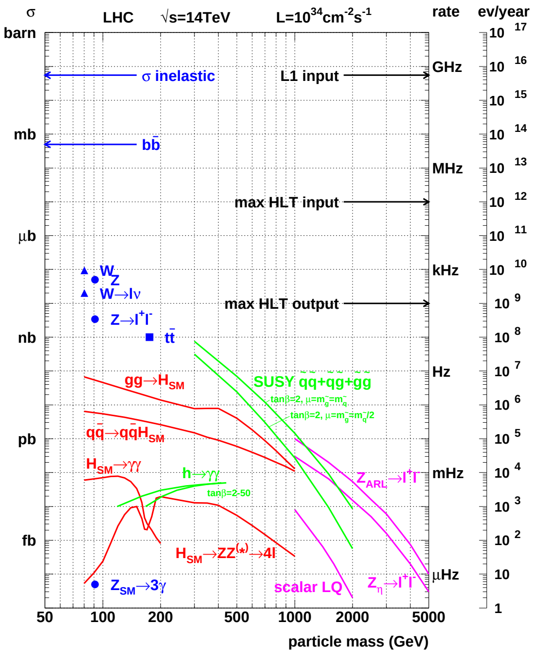

Figure 2.19: *Cross sections and event rates at the LHC design luminosity as functions of particle masses. The L1 and HLT input and output rates are indicated.*

The selection of the events is based on their physics content, so the on-line algorithms must have a level of sophistication comparable to that of the off-line reconstruction. On the other hand, the time available to accept or reject an event is extremely limited, given the bunch crossing time of 25 ns. In such a short time interval, it is impossible to read out all raw data from the detector. For this reason, CMS adopts a multi-level trigger design, where each step of the selection uses only part of the available data. In this way, higher trigger levels have to process fewer events and can use more refined algorithms to perform a detailed reconstruction.

The CMS trigger is structured in two physical levels: the *Level-1 Trigger* (L1) [35] and the *High Level Trigger* (HLT) [36]. The L1 is based on custom-made hardware and uses only coarsely segmented data from calorimeters and muon detectors, while all the high-resolution data is held in pipeline memories in the front-end electronics. A schematic representation of the L1 trigger is provided in Figure 2.20. The HLT, instead, is software implemented in a single processor farm, and is organised in several logical levels of increasing complexity, each accessing more data than the previous one. A more detailed description of the muon HLT is given in Section 3.8.

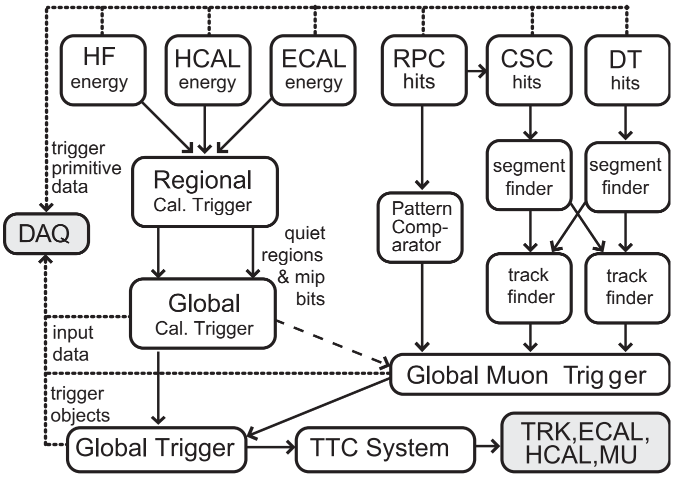

Figure 2.20: *Structure of the Level-1 Trigger system.*

Chapter 3

Muon Reconstruction

Muon detection and reconstruction play a key role in the CMS physics program, both for the discovery of new physics and for precision measurements of SM processes. CMS has been designed for a robust detection of muons over the entire kinematic range of the LHC and in a condition of very high background. The muon system allows an efficient and pure identification of muons, while the inner tracker provides a very precise measurement of their properties. An excellent muon momentum resolution is made possible by the high-field solenoidal magnet. The steel flux return yoke provides additional bending power in the muon spectrometer, and serves as a hadron absorber to facilitate the identification of muons.

Several muon reconstruction strategies are available in CMS, in order to fulfill the specific needs of different analyses. The reconstruction of muons consists of three main stages:

- local reconstruction (Section 3.2): in each muon chamber, the raw data from the detector read-out are reconstructed as individual points in space; in CSC and DT chambers, such points are then fitted to track stubs (*segments*);
- stand-alone reconstruction (Section 3.3): points and segments in the muon spectrometer are collected and fitted to tracks, referred to as "stand-alone muon tracks";
- global reconstruction (Section 3.4): stand-alone tracks are matched to compatible tracks in the inner tracker and a global fit is performed using the whole set of available measurements: the resulting tracks are called "global muon tracks".

Muon identification (Section 3.5) represents a complementary approach with respect to global reconstruction: it starts from the inner tracker tracks and flags them as muons by searching for matching segments in the muon spectrometer. The muon candidates produced with this strategy are referred to as "tracker muons".

After the completion of both algorithms, the reconstructed stand-alone, global and tracker muons are merged into a single software object, with the addition of further information, like isolation and energy collected in matching calorimeter towers. This information can be used for further identification, in order to achieve a balance between efficiency and purity of the muon sample.

The three steps of global muon reconstruction and the muon identification are discussed in more detail in Sections 3.2 to 3.5. Particular emphasis is placed on the description of stand-alone reconstruction and of its development, which represents an important part of the work reported in this thesis.

3.1 Simulation of Muon Samples

Throughout this chapter, several samples of simulated muons are used. All samples are produced with a full Monte Carlo simulation of the CMS detector response, based on GEANT [37].

The performance of the reconstruction algorithms (Sections 3.3 to 3.5) is tested on single-muon Monte Carlo samples, generated with PYTHIA [38] at different transverse momentum values. These samples are produced with "ideal conditions", i.e. using the CMS design geometry and considering perfect detector alignment and calibration. Muons have a flat η distribution, between -2.5 and 2.5.

In Section 3.7, the performance of muon reconstruction observed in 2010 CMS data is compared with the expected performance in simulation. For this purpose, $J/\psi \rightarrow \mu^+\mu^-$ and $Z \rightarrow \mu^+\mu^-$ events are generated with a "start-up scenario", i.e. with the realistic alignment and calibration conditions at the beginning of data taking [39][40][41]. The J/ψ samples are generated with PYTHIA, and contain both *prompt* and *non-prompt* J/ψ, in proportion to the respective cross sections. Non-prompt J/ψ from decays of B_+, B_0 and B_s are considered. The Z samples are generated with ALPGEN [42], but using PYTHIA for the hadronisation and showering phases.

3.2 Local Reconstruction

Local reconstruction is the reconstruction of basic hits and segments in individual muon chambers, starting from the output of the Data Acquisition system. The results are track segments in the DTs and CSCs and individual points in the RPCs.

All the measurements reconstructed in the muon system, as well as in the inner tracker, are generally referred to as "reconstructed hits" and implemented in the reconstruction software with a common interface, called

“`TrackingRecHit`”. Points and segments, despite their differences, are all instances of this general class, giving great flexibility to the fitting algorithm.

3.2.1 Local Reconstruction in the DTs

Local reconstruction in the DTs [33] begins with the reconstruction of mono-dimensional hits in individual drift cells. The only information contained in these hits is their distance from the anode, with an intrinsic left/right ambiguity and without any information about their position along the wire.

The cell hits are the starting point for the reconstruction of segments in the r-ϕ and r-z projections separately. These two-dimensional segments still do not provide any information about the coordinate along the sense wires, but they allow the measurement of the track angle in the measurement plane (orthogonal to the wires).

The 3D position and direction of the muon crossing the chamber are obtained combining the two projections. The resulting three-dimensional segments have an angular resolution of about 0.7 mrad in ϕ and about 6 mrad in θ [33].

3.2.2 Local Reconstruction in the CSCs

Each CSC plane measures a point in two dimensions. The radial coordinate r is measured by the wires, the azimuthal coordinate ϕ by the strips. To obtain a precise measurement, the charge distribution of a cluster of three neighbouring strips is assigned a position according to a look-up table. The tabulated positions are pre-determined by fits of charge distributions with the so-called “Gatti function” [43].

The hits in a chamber are used to fit a three-dimensional straight line segment (made of up to six points). The position resolution of segments varies from about 50 μm in the first CSC station to about 250 μm in the fourth [34]. The directional resolution varies with the chamber type, with an average of about 40-50 mrad in ϕ, slightly worse in θ.

3.2.3 Local Reconstruction in the RPCs

The RPCs are characterised by an excellent time resolution, of the order of few nanoseconds, while their spatial resolution is limited by the strip pitch. In each chamber, the two coordinates (ϕ and z in the barrel, ϕ and r in the endcaps) and their uncertainties are obtained by clusterising the fired adjacent strips and computing their centroid, assuming a uniform charge distribution on the area of the strips. The resolution on ϕ is around 1 cm, while the orthogonal coordinate is only constrained by the strip length [44].

3.3 Stand-Alone Reconstruction

The reconstruction of a track in the muon spectrometer starts from an initial state, called *seed*, estimated from DT and CSC segments in the off-line reconstruction (Section 3.3.1) and from the parameters of the Level-1 trigger candidates in the on-line reconstruction (Section 3.8.1). The track is then extended using an iterative algorithm which, at each step, collects the compatible hits in a chamber and updates the trajectory parameters (Section 3.3.2). Once all the tracks are built and possible duplicates or *ghosts* removed (Section 3.3.3), the remaining tracks are extrapolated to the point of closest approach to the beam line. In order to improve the momentum resolution, a beam spot contraint can be applied (Section 3.3.4).

3.3.1 Seed

The seeding algorithm takes DT and CSC segments as input and combines them to produce a set of initial states which are the starting point for the reconstruction of muon tracks.

First, a pattern of segments in the stations is searched for, using rough geometrical criteria. For a pattern, which may also consist of just one segment, the p_{T} of the seed candidate is estimated using parametrisations of the form:

$$p_{\mathrm{T}} = A - \frac{B}{\Delta\phi} \tag{3.1}$$

For DT seed candidates with segments in MB1 or MB2, $\Delta\phi$ is the bending angle of the segment with respect to the vertex direction, assuming that the muon has been produced at the interaction point. If segments from both MB1 and MB2 exist, the weighted mean of the estimated p_{T}'s is taken. If the seed candidate has only segments in MB3 and MB4, the difference in bending angle between the segments in the two stations is used to calculate the p_{T}. In the CSC and overlap region, the seed candidates are built with a pair of segments in either the first and second stations or the first and third stations. $\Delta\phi$ is the difference in the ϕ coordinate between the two segments. Otherwise, the direction of the highest quality segment is used. Although this algorithm is currently used only for the off-line seeding, its fast estimation of the muon momentum could be used in an intermediate trigger selection step between Level-1 and Level-2.

The efficiency of building a muon seed is mainly determined by detector acceptance and, in part, by the efficiency of segment reconstruction. Figures 3.1a to 3.1c show the muon seed efficiency as a function of the main kinematic variables. Muons were simulated at different transverse momenta, from 1 GeV/c to 1 TeV/c, with a uniform η distribution between -2.5 and 2.5 and assuming a perfectly aligned detector. The inefficiencies at $|\eta|$ around 0.3 and 0.8 in Figure 3.1a are due to the discontinuity of the muon detector in the barrel region, i.e. the gap between wheels. The inefficiency in ϕ between 0.8 and 1.8 rad (Figure 3.1b) is due to the presence of “chimneys” in sectors 3 and 4, used to route magnet services.

Figure 3.1d shows a distribution of the q/p_{T} resolution:

$$R_{seed}(q/p_{\mathrm{T}}) = \frac{(p_{\mathrm{T}})^{seed} - (q/p_{\mathrm{T}})^{sim}}{(q/p_{\mathrm{T}})^{sim}}\,, \tag{3.2}$$

for muons simulated with $p_{\mathrm{T}} = 20$ GeV/c. The distribution is fitted using a double Gaussian, where the larger Gaussian partly accounts for the tails arising from energy loss processes, such as ionisation, δ-rays and *bremsstrahlung*, which becomes relevant especially at high p_{T}. In Figure 3.2a, the q/p_{T} resolution of muon seeds for different p_{T} values is estimated as the smaller σ of this fit, which represents the width of the core distribution. In Figure 3.2b, the mean value of the fit is taken as a measure of the bias in the estimation of q/p_{T}.

3.3.2 Pattern Recognition and Fit

Tracks are built using the Kalman filter technique [45] (see Appendix A for a brief description), a recursive algorithm which performs the pattern recognition layer by layer and, at the same time, updates the trajectory parameters. Once all the hits have been collected, a final fitting step (*smoothing*) can be applied, updating the trajectory state at the location of all intermediate hits with the information from all the collected measurements, thus obtaining the optimal track parameters.

The algorithm is flexible enough to allow different possible strategies: the fit can be applied in either direction, from the innermost layer towards the outermost or *viceversa* (*forward* or *backward*), possibly multiple times to remove a bias from the initial seed, and using either segments or individual hits to update the trajectory parameters. In the following sections, the current strategy will be described.

Forward Filter

In the standard configuration, the parameters of the seed state are propagated to the innermost compatible muon chamber. Here the most compatible measurement is searched for on a χ^2 basis, estimating the *incremental* χ^2 ($\Delta\chi^2$) given by the inclusion in the fit of a given track segment (or individual hit, in the case of RPCs). Here, χ^2 is always understood to be normalised to the number of degrees of freedom of the segment or hit. If more than one compatible measurement is found, the one with the lowest $\Delta\chi^2$ is kept. Measurements with $\Delta\chi^2 > 1000$ are considered outliers, not *compatible* with a trajectory hypothesis, and are not taken into account. Moreover, only if $\Delta\chi^2 < 25$ the trajectory parameters are updated with the

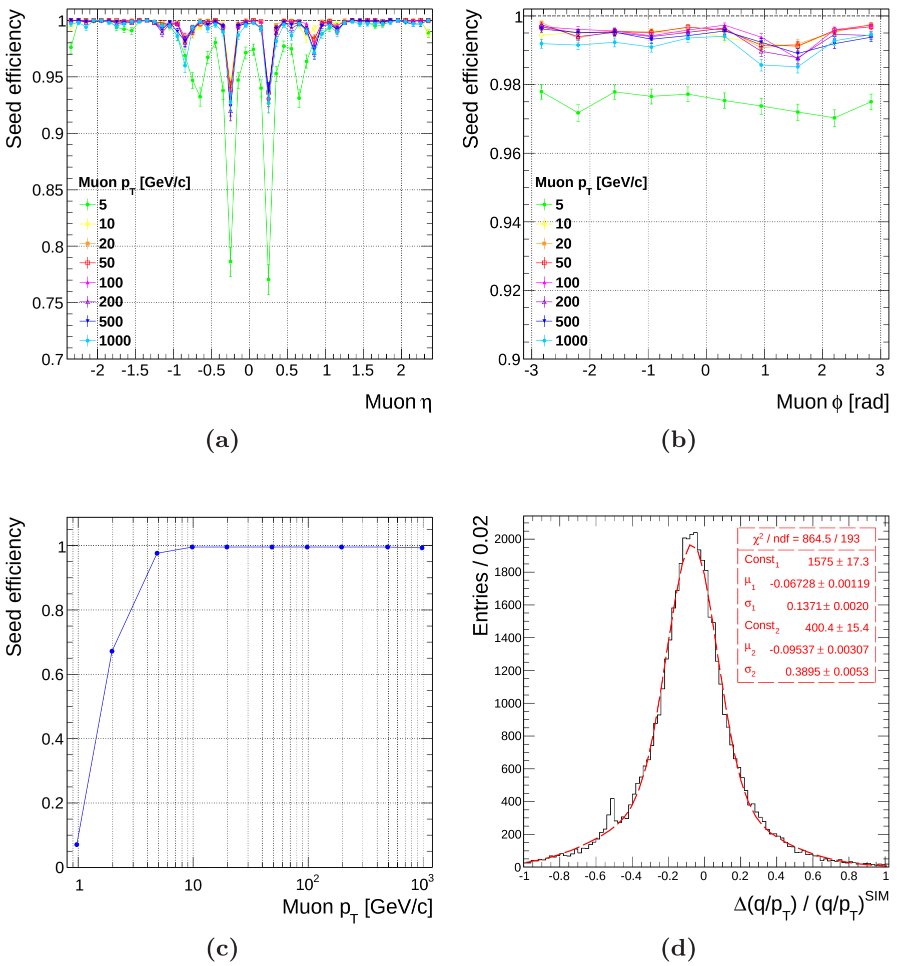

(a) **(b)**

(c) **(d)**

Figure 3.1: *Muon seed efficiencies (a) vs.* η*, (b) vs.* ϕ *and (c) vs.* p_{T}*. (d)* $R_{seed}(q/p_{\mathrm{T}})$ *distribution for muons at* $p_{\mathrm{T}} = 20$ *GeV/c. Muons are simulated with ideal conditions (cf. Section 3.1).*

new measurement information (i.e. position and direction of DT and CSC segments and position of RPC hits). Measurements failing this requirement are recorded in the trajectory, but not used to update its parameters. In the CMS jargon, such measurements are, somehow inappropriately, referred to as “invalid hits.”

The updated track parameters are then propagated to the next reachable chamber and the same procedure is repeated until no more chambers are reachable.

The forward filtering step is considered successful if compatible measurements are found in at least two muon chambers, one of them being a DT

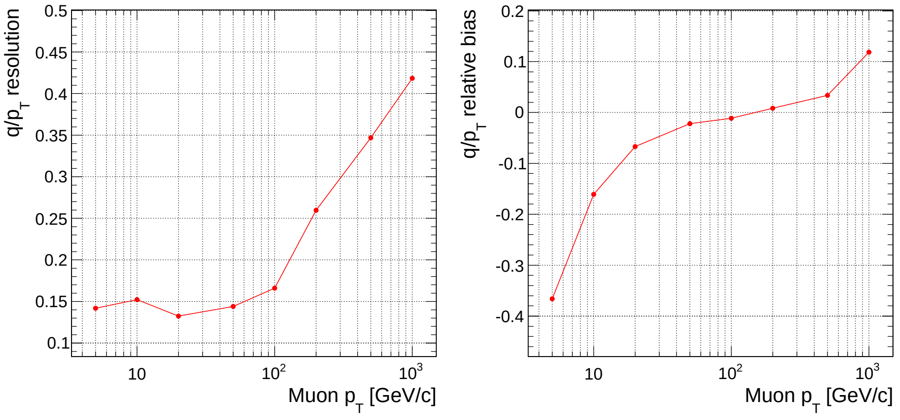

(a) **(b)**

Figure 3.2: *(a) q/p_{T} resolution and (b) relative bias of muon seed vs. p_{T}, estimated respectively as the σ and mean of the core of a double Gaussian fit to $R_{seed}(q/p_{\mathrm{T}})$ (e.g. see Figure 3.1d). Muons are simulated with ideal conditions.*

or CSC chamber. Otherwise the reconstruction algorithm is stopped and no track is produced. If measurements from at least two different chambers (one DT or CSC at least) have been used to update the trajectory parameters, the result of the forward filter is considered reliable and is passed to the following steps. Otherwise (i.e. no hits, or only hits from a single chamber have $\Delta\chi^2 < 25$), a track is built with the same parameters as the starting seed, with no contribution from the collected measurements (these are also called “zero-hit” tracks).

The use of a double $\Delta\chi^2$ threshold accomplishes two different requirements: the loose compatibility cut allows a very high efficiency, while the tighter threshold guarantees that only the most compatible measurements contribute to the determination of the trajectory parameters. This increases the quality of the reconstructed tracks and prevents the use of background hits, e.g. coming from electronic noise, punch-through or showering muons (*cf.* Section 3.6), which can spoil the parameter estimation to the point that, in the following iterations, no more measurements are collected and the track is discarded for lack of hits.

The “zero-hit” trajectories represent an extreme case. Since they are based only on the seed information, their quality is generally worse than for the other trajectories. Nonetheless they are made available for the global reconstruction, which, in some cases, can succeed even starting from a poorly reconstructed stand-alone track.

In Figure 3.3, the effect of the application of this strategy on p_{T} resolution of stand-alone (a) and global (b) tracks is shown for a sample of simulated muons with $p_{\mathrm{T}} = 100$ GeV$/c$. The blue histograms are the distributions obtained applying a single $\Delta\chi^2$ threshold in stand-alone reconstruction, the red are obtained with a double threshold. The blue distribution of stand-alone tracks shows a shoulder around -1, due to tracks reconstructed with $p_{\mathrm{T}} \ll 100$ GeV$/c$. This shoulder was found to be originated mostly by radiative processes, such as δ-rays and *bremsstrahlung*, which produce extra hits in the chambers. For this reason, this effect increases at higher p_{T}. The use of a double $\Delta\chi^2$ cut proves more effective in rejecting the extra hits, thus improving the p_{T} resolution: in the red histogram, the shoulder is essentially suppressed and the efficiency is slightly higher. The improvement in the stand-alone track quality propagates to the global reconstruction, reducing the non-Gaussian tails and slightly increasing the global efficiency.

All the thresholds discussed above, as well as several options in the application of the algorithm, can be specified through a set of configuration parameters. A complete list of the parameters used in the forward filter is reported in Appendix B (Table B.1).

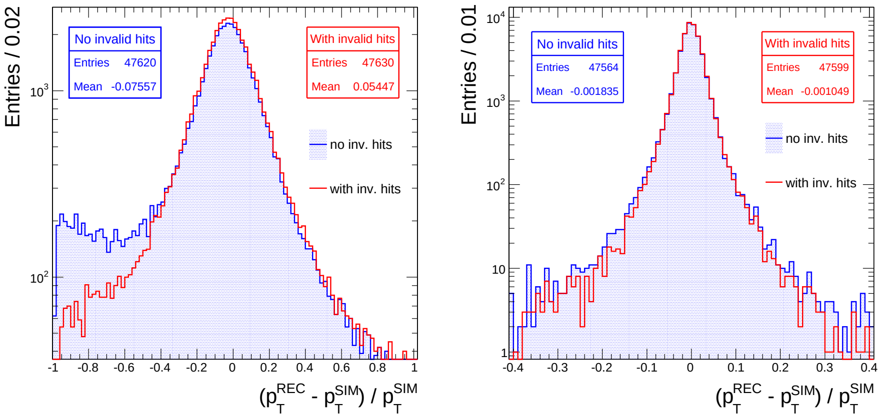

(a) **(b)**

Figure 3.3: *Muon p_{T} resolution of (a) stand-alone and (b) global tracks, using different strategies for pattern recognition and fit: in the blue histograms, a single $\Delta\chi^2$ threshold is used for the hit selection and for the update of the trajectory; in the red histograms, different cuts are used to select hits and to include them in the fit, as specified in Tables B.1 and B.2.*

Backward Filter

The outcome of the pre-filter can be affected by a significant bias from the initial seed state. For this reason, the track parameters obtained at the last update of the forward pattern recognition are used as input to a second filtering step, this time navigating inward (*backward filter* or simply *filter*). The track parameters errors can be optionally rescaled prior to doing the backward filtering.

The backward filter algorithm is similar to the forward filter, with the differece of the outside-in extrapolation direction and of the use of individual hits constituting the collected segments for the fit. Besides, tighter cuts are used in the pattern recognition.

The procedure is repeated until no more inward layers are reachable. As in the forward filter, the final track candidate is kept if compatible hits are found in at least two chambers and in at least one DT or one CSC chamber.

The complete list of parameters used in the backward filter is reported in Table B.2.

Refits

A bias coming from the seed state can still be present after the backward filter. For this reason, it is possible to refit the hits collected during the backward filter a configurable number of times, without performing the pattern recognition.

Each refit consists in a Kalman filter step without pattern recognition, followed by a smoothing step in the opposite direction (see Appendix A for more details). The starting state is the last updated state of the backward filter, with the covariance matrix rescaled by a large factor, e.g. 100. This rescale is needed to prevent an underestimation of the errors, since the initial state already includes the information of the hits to be fitted.

The complete list of parameters used in the final fit is reported in Table B.3.

3.3.3 Ghost Suppression

The trajectory building algorithm is run for each seed. If the seeding algorithm fails to merge all the track segments from the same muon, several seeds can be built from a single muon, giving rise to duplicates of the same tracks. These duplicates, called *ghosts*, usually share a fraction of their measurements. In order to remove them, all the track candidates that share at least one hit are compared with each other and only the best candidate is kept, according to the follwing criteria:

- if the difference in the number of hits is larger than four, the candidate with more hits is kept;
- otherwise, if more than 95% of the hits are shared, one candidate has $p_{\mathrm{T}} > 7$ GeV/c and the other has $p_{\mathrm{T}} < 3.5$ GeV/c, then the candidate with the lowest transverse momentum is rejected;

- otherwise, the candidate with the smallest normalised χ^2 of the fitis kept.

This step is also called trajectory *cleaning*.

In Figure 3.4, the ghost rate in stand-alone and global reconstruction is shown for a sample of simulated muons with $p_T = 100$ GeV$/c$. The blue histograms show the ghost rate obtained without the application of ghost suppression at stand-alone level, while the red histograms are the ghost rates when this cleaning is applied. The algorithm proves very effective, especially in the barrel region, where the rate of duplicate tracks is reduced by several orders of magnitude.

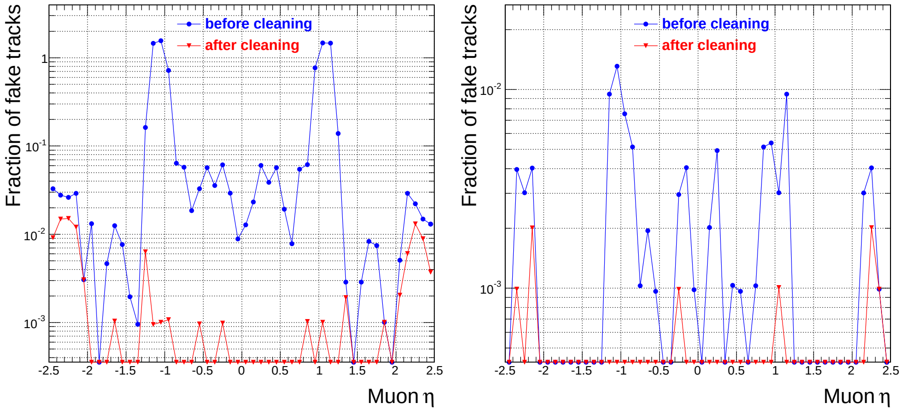

(a) (b)

Figure 3.4: *Ghost track rates vs η for (a) stand-alone and (b) global muons, without applying the stand-alone trajectory cleaner (blue) or with the standard cleaning strategy applied (red), for muons at p_T = 100 GeV/c.*

3.3.4 Beam Spot Constraint

In order to improve the momentum resolution of tracks, the beam spot position is used to constrain the track parameters. Although the beam position in the transverse plane is known within few tens of microns, the beam spot position uncertainty is set to 1 mm in the constraint. A more stringent constraint was found not to produce a significant improvement in the momentum resolution, while it would be more subject to cause a momentum bias in case of a systematic bias in the beam spot position. In the z direction, instead, the design beam spot uncertainty of 5.3 cm is used. A loose cut on the vertex-track χ^2 (see Table B.4) is applied to avoid constraining tracks that are not compatible with the beam spot position.

In Figure 3.5, the effect of the beam spot contraint on the momentum resolution is shown. The q/p_{T} resolution of stand-alone tracks is taken as the σ of the core of a double Gaussian fit to $R_{sta}(q/p_{\mathrm{T}})$ (*cf.* Equation 3.2), as described in Section 3.3.1 for the case of the seed. An improvement as large as 20% at $p_{\mathrm{T}} = 1$ TeV$/c$ is obtained.

The constrained tracks are stored and made available to the global reconstruction. The unconstrained tracks are kept for reference and saved in a separate collection.

The complete list of parameters used in the beam spot constraint is reported in Table B.4.

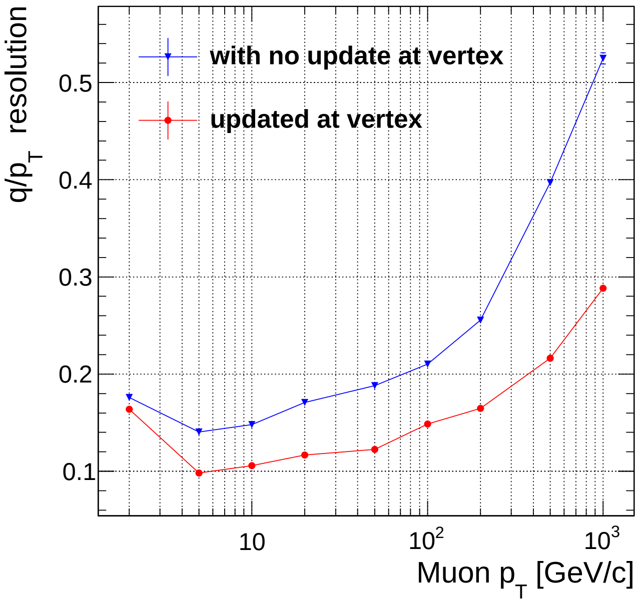

(a)

Figure 3.5: *q/p_{T} resolution of stand-alone tracks, before (blue) and after (red) the beam spot constraint, estimated as the σ of the core of a double Gaussian fit, as described in Section 3.3.1.*

In Figure 3.6, the efficiency of stand-alone track reconstruction is shown as a function of the main kinematic variables, for simulated muons at different transverse momenta, with a flat η distribution between -2.5 and 2.5 and with design geometry and alignment. The inefficiencies at $\eta \simeq 0.3$ and 0.8, and at ϕ between 0.8 and 1.8 rad are inherited from the seeding step (see Section 3.3.1). Figure 3.6c shows the stand-alone efficiency relative to the seeding step: a small loss is visible for $p_{\mathrm{T}} < 5$ GeV$/c$, while full efficiency with respect to seeding is reached at higher momentum. Figure 3.7b shows that a small bias in q/p_{T}, coming from the seed initial state, is still present, although reduced by about one order of magnitude with respect to the seed.

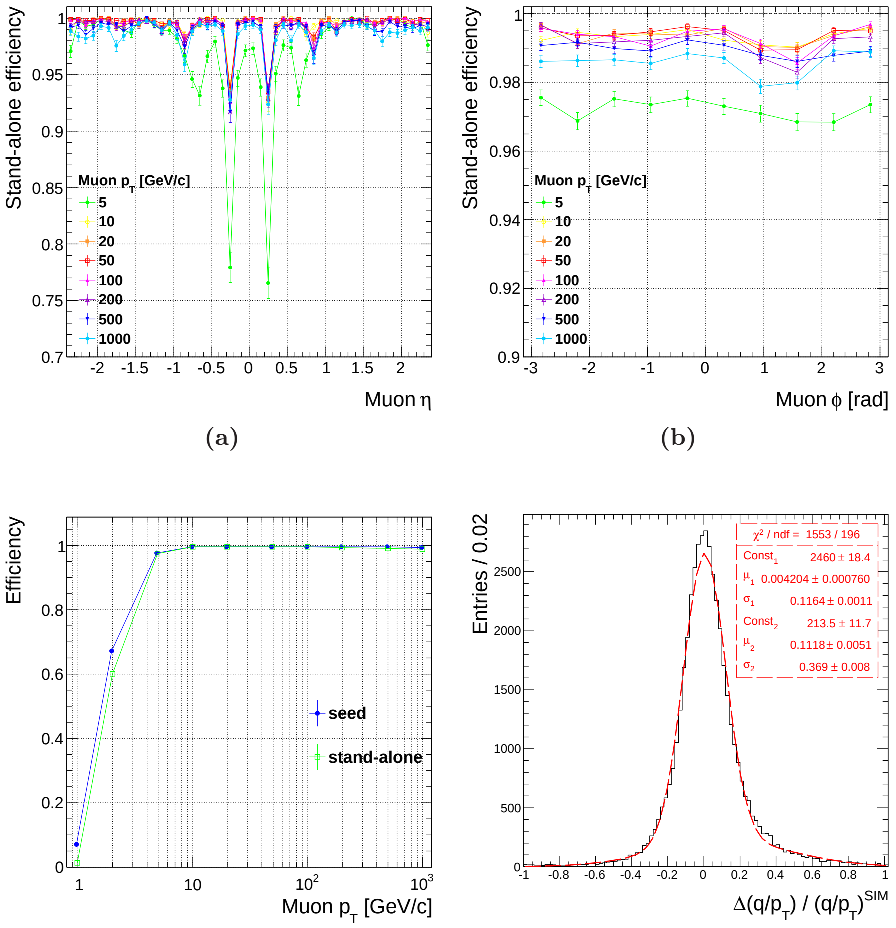

(a) (b)

(c) (d)

Figure 3.6: *Stand-alone muon track efficiencies (a) vs.* η*, (b) vs.* ϕ *and (c) vs.* p_{T}*, using simulated muons at different transverse momenta and with desing geometry and alignment. (d)* $R_{sta}(q/p_{\mathrm{T}})$ *distribution (cf. Equation 3.2) for stand-alone muons at* p_{T} *= 20 GeV/c.*

3.4 Global Reconstruction

The reconstruction of global muon tracks begins after the completion of the reconstruction of the stand-alone tracks (see Section 3.3) and the inner tracker tracks (described in Section 3.4.1). Each stand-alone track is matched to a compatible tracker track (Section 3.4.2) and a fit of all the available measurements is performed (Section 3.4.3).

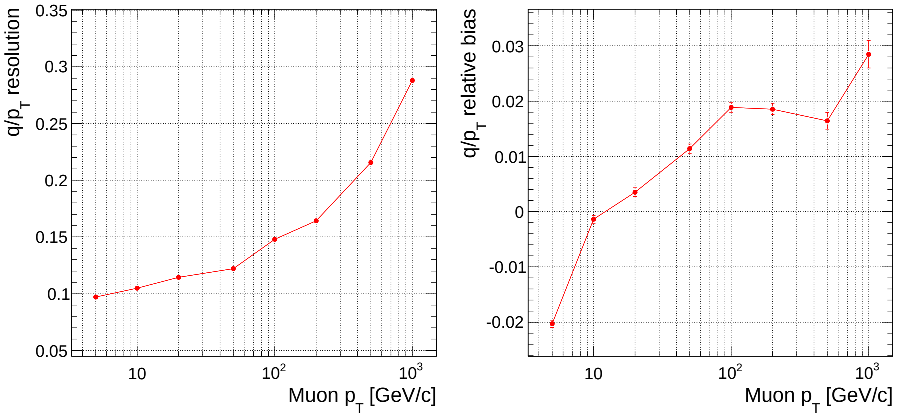

(a) **(b)**

Figure 3.7: *(a) q/p_{T} resolution and (b) relative bias of stand-alone muon tracks vs. p_{T}, estimated respectively as the core σ and mean of a double Gaussian fit to $R_{sta}(q/p_{\mathrm{T}})$ (e.g. see Figure 3.6d). Muons are simulated with ideal conditions.*

3.4.1 Track Reconstruction in the Inner Tracker

As in the muon system, the first step of the track reconstruction [46] is finding a *seed*, which is the starting point for the pattern recognition.

Two different algorithms have been implemented for pattern recognition. In the first one, seeds are built using two or three consecutive hits, in the pixel and/or in the strip detector. The pattern recognition is then performed layer by layer, with an iterative technique based on the Kalman filter, similarly to that used in the muon spectrometer alone.

The second algorithm, called *road search*, uses only the silicon strip detector to find the seeds: it takes one hit in the innermost layer and one in the outermost and considers the possible paths which can connect the two initial hits. The pattern recognition is performed collecting the measurements around the paths.

Both algorithms end with a final fit of the collected hits, followed by the suppression of ghost tracks.

In the standard muon reconstruction, only the tracker tracks obtained with the Kalman filter approach are used for the matching with the muon spectrometer and for the global fit.

3.4.2 Track Matching

The process of identifying the tracker track to combine with a given standalone muon track is referred to as *track matching* and consists of two steps. The first step is to define a *region of interest* (ROI) in the track parameter space that roughly corresponds to the stand-alone muon track, and to select the subset of tracker tracks inside this ROI. The second step is to iterate over this subset, applying more stringent spatial and momentum matching criteria to choose the best tracker track to combine with the stand-alone muon.

The ROI is defined using the stand-alone track parameters and assuming that the muon comes from the interaction point. A rectangular η-ϕ region is chosen according to the error estimates of the stand-alone muon momentum at the interaction point. The origin of the ROI is taken as a fixed r-z region around the beam spot. A minimum p_{T} limit for the tracks in the ROI is chosen as 60% of the stand-alone muon p_{T}, and is used to determine the curvature of the tracking region. The definition of the ROI has a strong impact on the reconstruction efficiency, fake rate and CPU reconstruction time.

The matching is performed by comparing the parameters of the stand-alone track with those of all tracker tracks in the ROI. This is best done by propagating the tracks onto a common reference surface, e.g. the detector layer of the innermost stand-alone track hit. In order to maximise the matching efficiency, several criteria are applied in sequence. First, the tracks with the a χ^2 compatibility with the stand-alone track[1] below a fixed threshold are chosen. If all tracks fail this cut, then the positions of the stand-alone and inner tracks on the reference plane are compared. If also this criterion fails and no pair is found within a fixed cut, the matching is attempted by comparing the track directions at the interaction point, with a very loose cut applied. If all criteria fail, the reconstruction is stopped and no global track is produced. It is clear that the matching algorithm can select more than one tracker track for a given stand-alone. In this case, all matched tracks proceed in the reconstruction chain.

3.4.3 Global Fit

The last step is to fit a global track using all hits belonging to the matching tracker and stand-alone tracks. The global refit algorithm attempts to perform a fit for each tracker-stand-alone track pair. If more than one global track is produced for a given stand-alone, the one with the best χ^2 is chosen. Thus, for each stand-alone muon there is a maximum of one global muon that will be reconstructed. The reconstruction ends with the association of energy deposits in the calorimeters to the global tracks.

Since the pattern recognition has already been performed during the reconstruction of the tracker and stand-alone muon tracks, no additional pattern recognition is done: the default global fit algorithm simply combines the tracker hits of the chosen track with the muon hits of the stand-alone

---

[1] $\chi^2 = (\mathbf{a}_{sta} - \mathbf{a}_{trk})^T \left[C_{sta} + C_{trk}\right]^{-1} (\mathbf{a}_{sta} - \mathbf{a}_{trk})$, where $\mathbf{a_i}$ is the vector of the five parameters of a track and C_i is the corresponding covariance matrix.

muon. However it is also possible to combine only a subset of the hits for the global fit. In particular, choosing a subset of the muon hits provides a better momentum resolution for high energy muons, when the measurements in the muon system are frequently contaminated by electromagnetic showers. The treatment of very energetic muons will be described in Section 3.6.

In Figure 3.8, the efficiency of global track reconstruction is shown as a function of the main kinematic variables, for simulated muons at different transverse momenta, with a flat η distribution between -2.5 and 2.5 and with design geometry and alignment. The inefficiencies at $\eta \simeq 0.3$ and 0.8, and at ϕ between 0.8 and 1.8 rad (Figures 3.6a and 3.6b) are inherited from the previous reconstruction steps (see Figures 3.1a and 3.6a). A larger inefficiency appears in the barrel region for muons with $p_{\mathrm{T}} = 5$ GeV/c, uniformly distributed in ϕ. Such inefficiency at low p_{T} is visible also in Figure 3.8c, which compares global, stand-alone and seeding efficiencies. At low p_{T}, muons easily stop in yoke without crossing all muon stations, especially in the barrel region, and stand-alone tracks are reconstructed with a relatively low number of hits and with a poorer momentum resolution. This makes the matching with tracker tracks more difficult and less efficient. As will be shown in Section 3.5, muon identification proves more efficient in this p_{T} region.

In Figure 3.9a, the resolution of global tracks is found to be between 1 and 2% up to $p_{\mathrm{T}} = 100$ GeV/c and slightly above 6% at 1 TeV/c. Figure 3.9b shows a q/p_{T} bias of the order of few permil up to 1 TeV/c.

3.5 Muon Identification

As explained in Section 3.4, the standard muon track reconstruction starts from the muon system and combines stand-alone muon tracks with tracks reconstructed in the inner tracker. This approach naturally identifies the muon tracks in the detector. However, a large fraction of muons with transverse momentum below 6-7 GeV/c (*cf.* Figure 3.8c) does not leave enough hits in the muon spectrometer to be reconstructed as stand-alone muons. Moreover, some muons can escape in the gap between the wheels.

A complementary approach has therefore been designed to identify offline these muons and hence improve the muon reconstruction efficiency: it consists in considering all silicon tracker tracks and identifying them as muons by looking for compatible signatures in the calorimeters and in the muon system.

The algorithm for the muon identification of the tracker tracks starts with the extrapolation of each silicon track outward to its most probable location within each detector of interest (ECAL, HCAL, HO, muon system). After collecting the associated signals from each detector, the algorithm determines compatibility variables corresponding to how well the observed

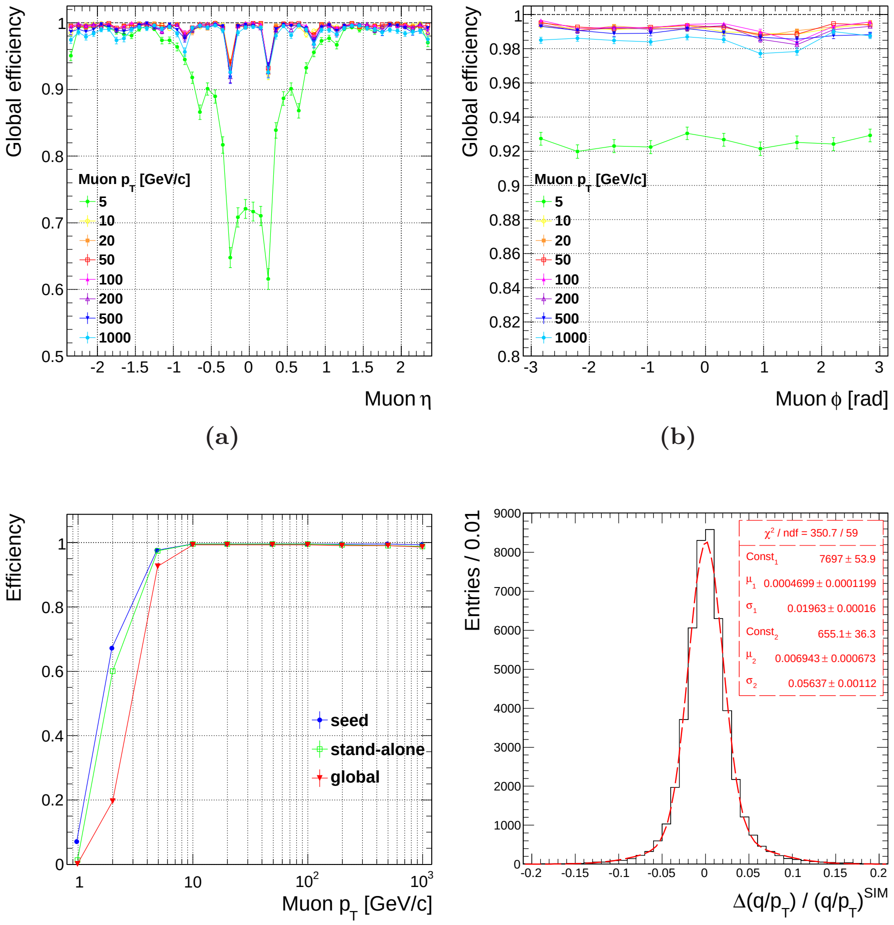

(a) **(b)**

(c) **(d)**

Figure 3.8: *Global muon track efficiencies (a) vs.* η*, (b) vs.* p_{T} *and (c) vs.* ϕ*. (d)* $R_{glb}(q/p_{\mathrm{T}})$ *distribution (cf. Equation 3.2) for global muons at* $p_{\mathrm{T}} = 100$ *GeV/c.*

signals fit with the hypothesis that the silicon track is produced by a muon. A very loose threshold on the compatibility variables is applied to select candidates that are saved in the muon collection; different physics analyses can apply further selections on the same variables, in order to balance the purity and efficiency of the muon identification.

In the calorimeters, the algorithm calculates and stores the energies in all the crystals (ECAL) or towers (HCAL) crossed by the track, as well as the energies in a 3 × 3 region. Based on these energies, a compatibility variable is determined, which describes how consistent these energies are with respect to what is expected for a muon. Muons identified through this

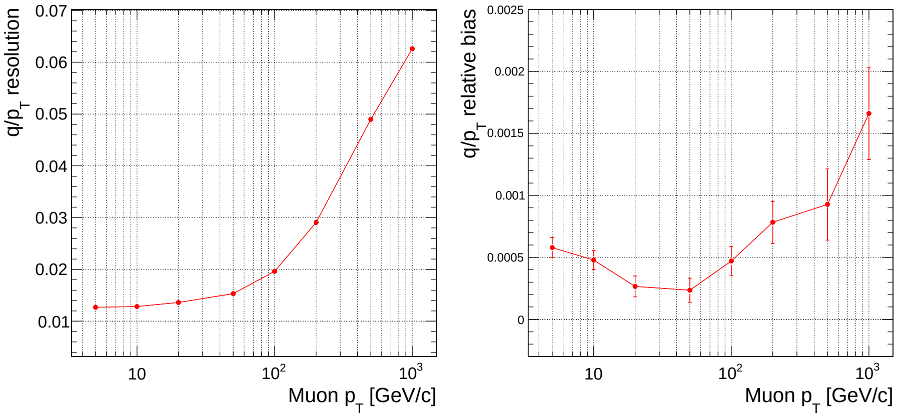

(a) **(b)**

Figure 3.9: *(a)* q/p_T *resolution and (b) relative bias of global muon tracks vs.* p_T*, estimated respectively as the core* σ *and mean of a double Gaussian fit to* $R_{glb}(q/p_\mathrm{T})$ *(e.g. see Figure 3.8d). Muons are simulated with ideal conditions.*

calorimeter-based compatibility are referred to as “calo-muons”.

In the muon system, for each crossed or nearly crossed chamber the algorithm stores the following variables:

- the distance between the propagated track and the nearest chamber edge, in both the chamber local x and y directions, with a conventional sign (negative inside the active volume, positive outside the active volume), and the corresponding 1σ uncertainty;
- the position (x, y) and slope $(dx/dz, dy/dz)$ of the extrapolated track in the local chamber coordinates and the corresponding 1σ uncertainties;
- the segments in the chamber that are near the propagated track (“associated segments”).

The above information can be employed for the purpose of muon identification. Muons identified by at least one associated segment are called “tracker-muons”.

Since each track is treated individually, if two or more tracks are near each other, it is possible that the same segment or set of segments is associated to more than one track, resulting in duplicate tracker muons. This ambiguity can be resolved by the *arbitration* algorithm, which assigns segments to tracks by looking at the best Δx or $\Delta R = \sqrt{\Delta x^2 + \Delta y^2}$ match.

Figure 3.10 shows the efficiency of the different muon reconstruction algorithms described in this and previous sections, for transverse momenta below 10 GeV/c. Since the muon identification algorithms do not need a track reconstructed in the muon system, calo-muons and tracker-muons exhibit a fairly high efficiency also in kinematical regions where the stand-alone reconstruction is not fully efficient, especially at very low p_{T}, below 3 GeV/c. The turn-on curve for tracker-muon efficiency in Figure 3.10b shows a step at 3 GeV/c, where the contribution of the muon barrel begins: in the central region ($|\eta| < 1.2$, also visible in Figure 3.10a), muons with lower transverse momentum do not reach the spectrometer, because of the energy loss in the inner detectors and the bending in the strong magnetic field. This inefficiency is significantly reduced in the case of calo-muons, which do not require an identification from the muon system. For the same reason, the calo-muon algorithm is efficienct also for $|\eta| > 2.4$, exploiting the larger coverage of the calorimeters.

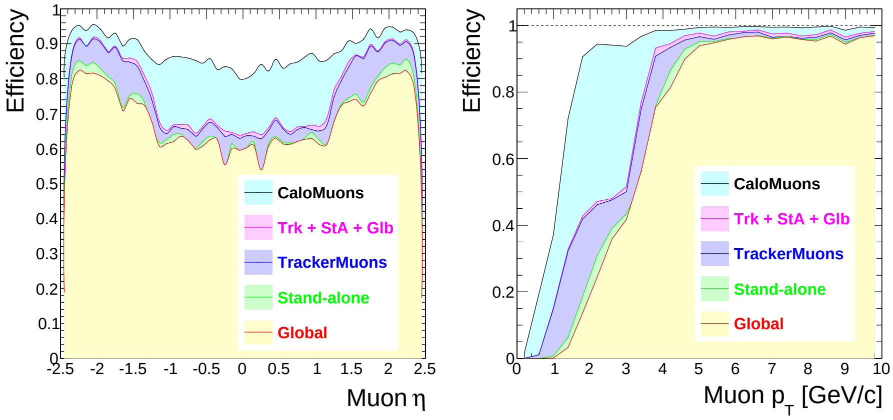

(a) (b)

Figure 3.10: *Muon reconstruction efficiencies (a) vs. η and (b) vs. p_{T}, for all the reconstruction algorithms described so far, for simulated muons with a flat η distribution between -2.5 and 2.5 and a flat p_{T} distribution between 0 and 10 GeV/c.*

Figure 3.11 shows the q/p_{T} resolution of muon tracks resulting from different fits: stand-alone, tracker-only and global. In the entire η range, the resolution of global tracks is clearly dominated by the tracker resolution, up to $p_{\mathrm{T}} \simeq 200$ GeV/c. For higher p_{T}, the contribution of the muon system becomes significant, and improves the global resolution by 10-20% at 1 TeV/c.

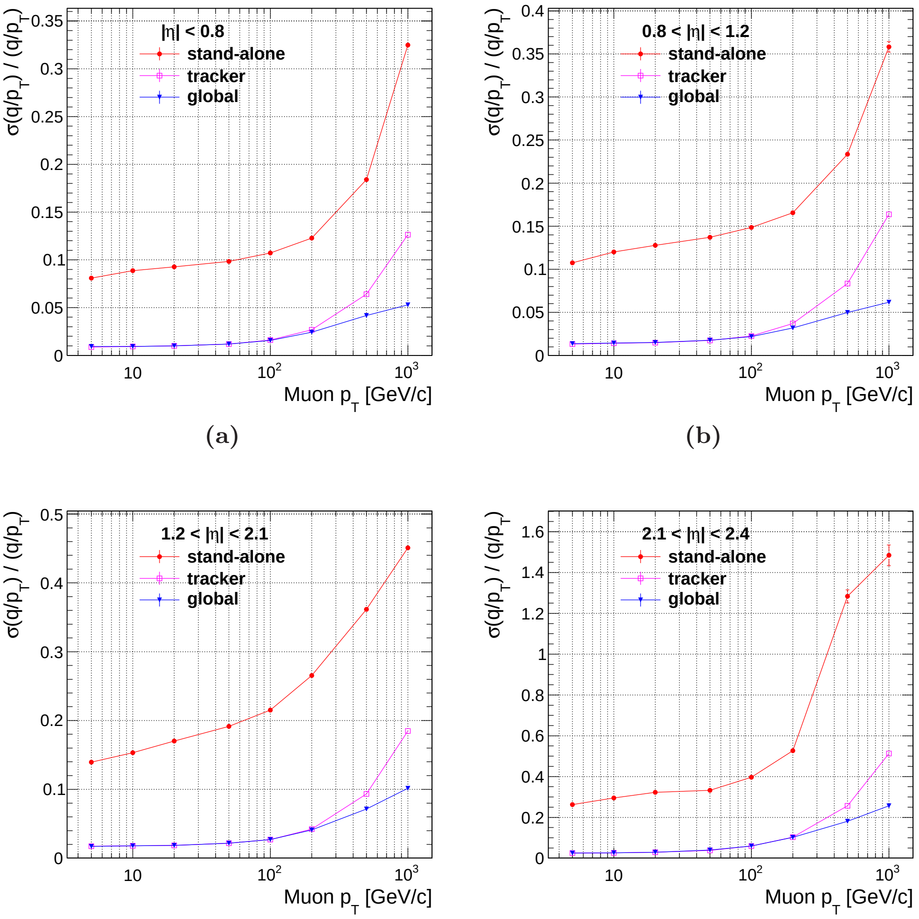

(a) (b)

(c) (d)

Figure 3.11: *Muon q/p_T resolution vs. p_T for the three different types of fit: stand-alone (red), tracker-only (magenta) and global (blue). Different pseudorapidity regions are considered separately: (a) $|\eta| < 0.8$, (b) $0.8 \leq |\eta| < 1.2$, (c) $1.2 \leq |\eta| < 2.1$ and (d) $|\eta| \geq 2.1$.*

3.6 Reconstruction of Very High Momentum Muons

Muons with energies of several hundred GeV and more have a high probability of producing electromagnetic showers in the iron of the CMS magnet return yoke. These large energy losses can significantly degrade the performance of the muon track fit. Two main effects can contribute to this degradation:

- the muon can lose a large fraction of its energy; in this case, the part of the track following the energy loss should be discarded as the particle momentum has changed;

- the shower can contaminate the muon detectors, causing the local reconstruction algorithms to return incorrect trajectory measurements. Including these measurements in the track fit can lead to incorrect reconstructed momentum values.

The approach chosen to minimise the negative effect of showers on muon momentum estimation consists in performing several refits of the global muon trajectory, selecting different sets of hits.

"First Muon Station." A fit with the hits from the tracker and the first muon station where hits are available. This selection minimises the effect of a large change in muon momentum after showering.

"Picky Muon Reconstructor." A fit with the hits selected by an algorithm applying tight cuts for hit compatibility with the trajectory, but only in muon stations with high multiplicity of reconstructed hits. This approach minimizes the influence of contaminated chambers, while preserving the hits from chambers providing good trajectory measurement, despite containing a shower.

These two refits are performed for each global muon. The resulting tracks are compared with the global and tracker-only tracks to determine the best fit based on goodness-of-fit variables.

3.7 Performance of Muon Reconstruction in 2010 Data

In this section, the performance of muon reconstruction is tested on samples of data taken during the 2010 LHC collision runs at 7 TeV. The events are selected using unprescaled muon triggers.

The Z candidates used for the efficiency measurements (Section 3.7.1) are selected with single-muon triggers, requiring the presence of a *Level-3 muon* (*cf.* Section 3.8) with a p_T threshold of 15 GeV/c (see Table 3.1). The Z samples used for the measurement of resolution and other track properties (Sections 3.7.2 and 3.7.3), in addition, exploit also a double-muon trigger, which requires two Level-3 candidates with p_T thresholds of 3 GeV/c.

For the J/ψ sample, special triggers are used, which require the presence of a Level-3 candidate with a low p_T cut, plus a tracker track with no p_T requirements.

3.7.1 Muon Efficiency

The efficiency is estimated using the *tag-and-probe* method, briefly explained in Appendix C and in [47][28][48]. In general, a “tag” is defined as a muon with tight identification requirements, while a “probe” is a simple track with possible quality cuts. A “passing probe” is a probe that satisfies the selection criteria whose efficiency is to be measured. Additionally, the tag muon must be associated to a muon trigger object, so that the probe is not biased by the need for a trigger in the event. The association is defined by a cut on $\Delta R = \sqrt{\Delta\phi^2 + \Delta\eta^2}$ between the muon track and the trigger candidate.

For low transverse momentum, below 15 GeV/c, the efficiency is probed using muons from J/ψ decays, while the higher momentum region is investigated with Z $\rightarrow \mu^+\mu^-$ events. In the plots shown in this section, whenever the efficiency is plotted as a function of η, only the high p_T muons from Z decays are used. The muon efficiencies in data are compared with the results obtained in simulation with the same tag-and-probe method, along with the simple “counting efficiency”, defined as the fraction of passing probes relative to the number of selected probes in a sample of simulated signal events.

In J/$\psi \rightarrow \mu^+\mu^-$ events, muons have a rather soft p_T spectrum. Global muons are used as tags and tracks with no further requirements are used as probes. The tag is also required to be associated to the Level-3 muon candidate produced by the J/ψ trigger, described above.

In the Z case, muons are expected to have higher p_T values, so tighter quality and identification criteria can be required, to reduce the background level to a minimum and restrict the analysis to a sample of very high quality muons. The tag is a global muon with the following quality requirements:

- it must be both a global and a tracker muon;
- its track must have more than ten hits in the silicon tracker, at least one of which in the pixel detector, and at least one valid hit in the muon chambers;
- transverse impact parameter lower than 2 mm;
- normalised χ^2 of the global track lower than 10.

In addition, the tag must be associated to the Level-3 candidate. The probe is a simple tracker track with a minimum p_T of 5 GeV/c.

In Figures 3.12 and 3.13, the efficiency of different muon categories are reported. In each case, a passing probe is defined as a probe track associated with the muon candidate in question. The association is checked with a ΔR cut.

In Figure 3.12, the efficiency of stand-alone muons is reported as a function of $|\eta|$ and p_{T}. The agreement between the tag-and-probe efficiency in simulation and the Monte Carlo truth shows the validity of the method. The efficiency measured in data is in fairly good agreement with the expectations, except for small discrepancies at low p_{T}.

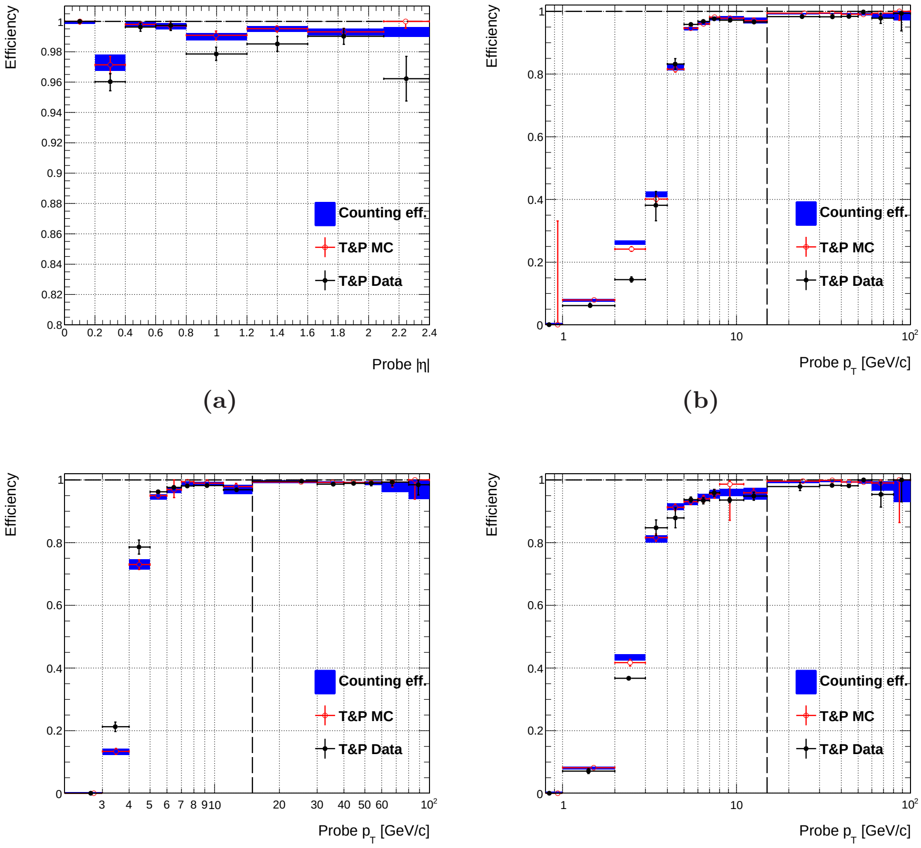

(a) **(b)**

(c) **(d)**

Figure 3.12: *Stand-alone muon efficiency vs. (a)* $|\eta|$*, (b)* p_{T} *in the whole* η *range, or limited to (c) the barrel or (d) endcap regions. The blue bands represent the “counting efficiency” in simulation, the red points the efficiency obtained with the tag-and-probe method applied to the same Monte Carlo samples, and the black points are the result on data. In (a), only* $\mathrm{Z} \to \mu^+\mu^-$ *events are considered. In (b), (c) and (d),* $\mathrm{J}/\psi \to \mu^+\mu^-$ *events are used below 15 GeV/c, Z above. The dashed, vertical line separates the two regions.*

In Figures 3.13a and 3.13b, the efficiency of global muons is shown as a function of $|\eta|$ and p_{T}. In Figures 3.13c and 3.13d, the same efficiencies are shown for global muons with a set of standard quality cuts, the same described above for the tag selection, used in many CMS analyses involving high-p_T muons. With these quality cuts, the agreement betweeen data and simulation is further improved.

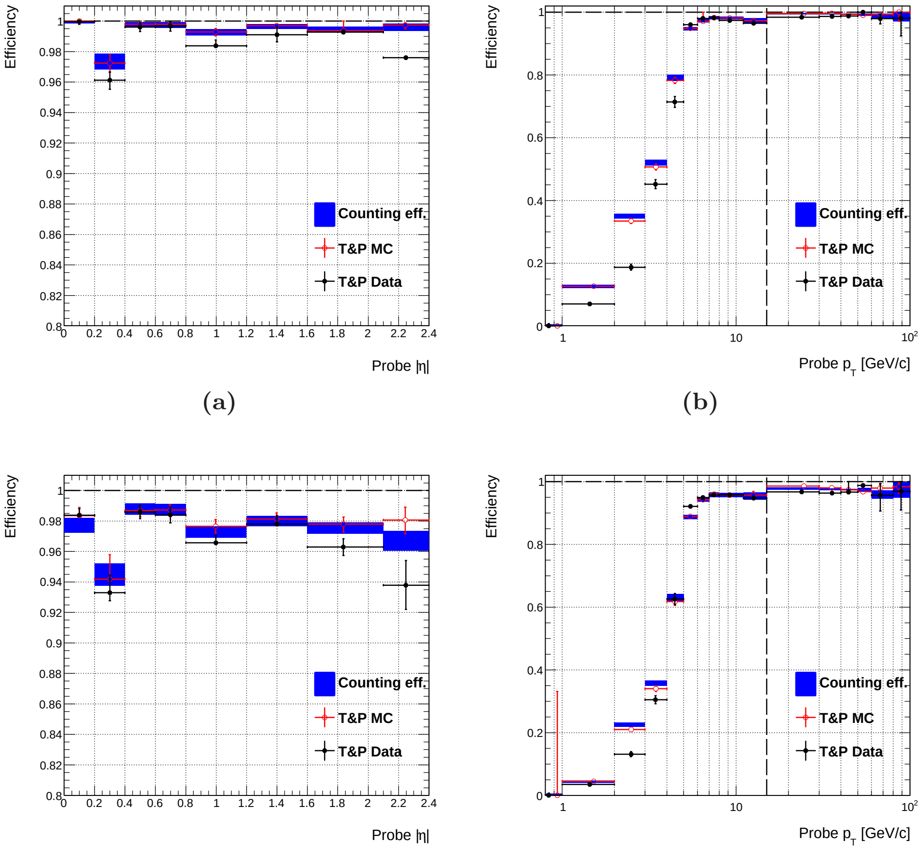

(a) (b)

(c) (d)

Figure 3.13: *Global muon efficiency vs. $|\eta|$ (left) and p_T (right), for plain global tracks (above) and after a set of quality cuts (below). In the plots vs. $|\eta|$, only $\mathrm{Z} \to \mu^+\mu^-$ events are used.*

3.7.2 Stand-alone Muon Resolution

The resolution on the measurement of stand-alone track parameters (p_T, η, ϕ) is obtained from data using the inner track as reference:

$$\begin{aligned} R_\mathrm{sta}(q/p_\mathrm{T}) &= \frac{(q/p_\mathrm{T})^\mathrm{sta} - (q/p_\mathrm{T})^\mathrm{trk}}{(q/p_\mathrm{T})^\mathrm{trk}} \\ R_\mathrm{sta}(\eta) &= \eta^\mathrm{sta} - \eta^\mathrm{trk} \\ R_\mathrm{sta}(\phi) &= \phi^\mathrm{sta} - \phi^\mathrm{trk}\,. \end{aligned} \tag{3.3}$$

This is an acceptable approximation, given that the resolution for the inner track is one order of magnitude better than the resolution of the stand-alone track. A more sophisticated algorithm to measure the resolution of global and tracker tracks from data will be described in Chapter 4.

A sample of muons coming from the decay of Z boson candidates is used. The same quality requirements listed for the selection of tags from Z in Section 3.7.1 are here applied to both muons. The resolutions measured on data are compared with the results obtained using a sample of simulated $Z \to \mu^+\mu^-$ events, with a realistic scenario of the detector alignment and calibrations at the start of data taking, and selected with the same requirements applied on data. The results for data and simulation are compared in Figure 3.14. Some discrepancies between data and simulation are visible, especially in the low p_T region and the ϕ spectrum. In general, however, the agreement is fairly good.

3.7.3 Muon Track Hits and χ^2

Using the same Monte Carlo and data samples of Z candidates described in Section 3.7.2, other properties of the stand-alone and global tracks can be probed.

In Figure 3.15, the number of hits in global tracks are shown for data and simulation. In Figure 3.15b, the groups of peaks represent the structure of the muon spectrometer, organised in four stations. The agreement between data and simulation is good, even though data show on average one hit less per track than simulation. This loss is likely due to dead channels in the muon chambers that are not correctly modelled in Monte Carlo, or to an imperfect description of the detector material budget or magnetic field, which can reduce the pattern recognition efficiency in the extrapolation through the detector layers. In the inner tracker detectors (Figures 3.15c and 3.15d), the discrepancy in the number of hits per track is even lower. As a consequence, the total number of hits per global track (Figure 3.15a) is between one and two.

In Figure 3.16, the normalised χ^2 distributions of stand-alone and global tracks are shown for data and simulation. In both cases, the distribution in data has a longer tail than in simulation. Possible causes for this difference are the accuracy of alignment and calibration scenarios used in the simulation, as well as the modelling of measurement uncertainties and of material material effects in the track fit.

3.8 Muon Trigger

The CMS muon trigger, as explained in Section 2.2.6, is structured in a first hardware level, the Level-1 Trigger (L1), and a software part, the High Level Trigger (HLT).

The Level-1 electronics uses groups of segments from DTs and CSCs, and hit patterns from RPCs. It identifies muon candidates, determines

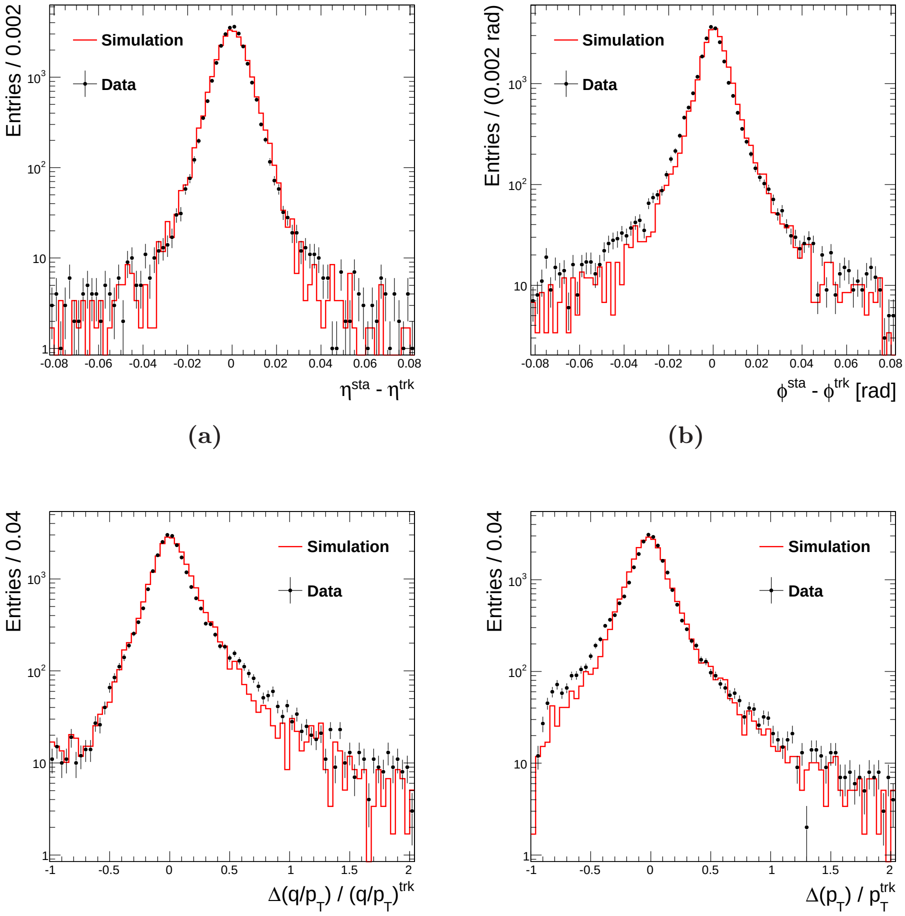

(a) **(b)**

(c) **(d)**

Figure 3.14: *Resolution of stand-alone muon track (a) η, (b) ϕ, (c) q/p_{T} and (d) p_{T}, in simulation (red line) and data (black markers), according to the difeinitions provided in Equation 3.3. A sample of* Z *boson candidates is used.*

their position and quality, and provides a transverse momentum estimate in a discretely binned form, based on segment slopes in DTs and CSCs, and on predefined hit patterns in RPCs. It also provides event timing and assigns events to a particular bunch crossing. Finally, the *Global Muon Trigger* (GMT) matches DT, CSC and RPC candidates, and rejects unconfirmed candidates of low quality. Up to four muon candidates, satisfying some minimal quality criteria and with the highest p_{T}, are transmitted to the HLT for further processing. More information about the Level-1 muon trigger can be found in [49].

The HLT is implemented in software and runs on the CMS on-line filter farm. Muon HLT performs a full track reconstruction, using the same

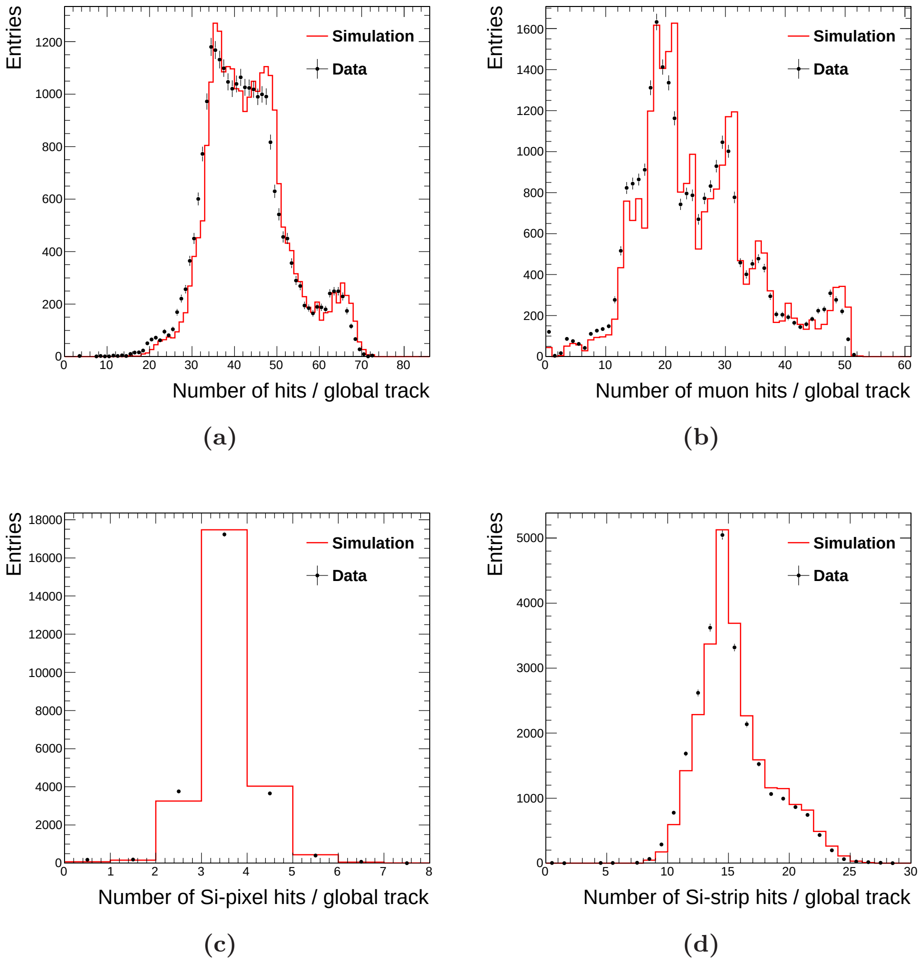

(a) (b)

(c) (d)

Figure 3.15: *(a) Total number of hits per global track and number of hits in the (b) muon, (c) pixel and (d) strip detectors per global track. Simulation (red line) and data (black markers) are compared.*

algorithms and software employed in the off-line reconstruction, with the differences described in the next section.

The muon HLT is structured in two main levels. This allows for a first reduction of the rate, based on a limited part of the information, which saves time for a more detailed reconstruction of the selected events. The *Level-2* (L2) uses muon system information to perform a stand-alone reconstruction, as in Section 3.3. A separate module in L2 computes the *isolation* of each muon candidate using calorimeter information.

The *Level-3* (L3) performs reconstruction in the silicon tracker and merges tracker tracks with L2 tracks, performing a global fit, as in Section 3.4. To keep execution time low, tracker reconstruction is regional, i.e.

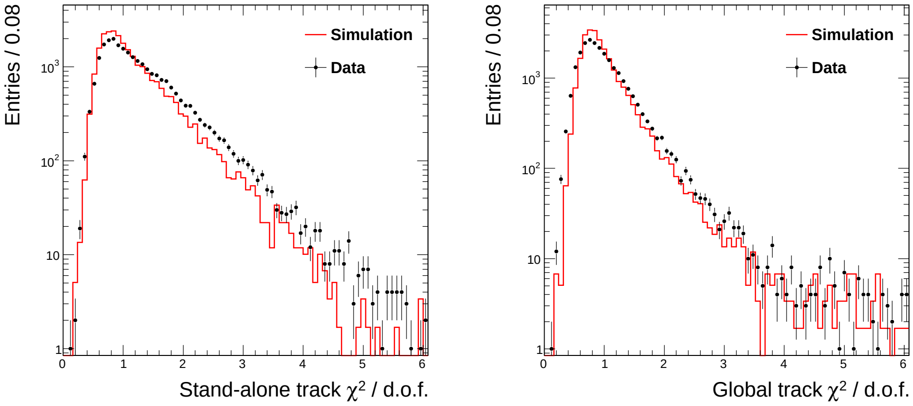

(a) **(b)**

Figure 3.16: *Normalised χ^2 distribution of (a) stand-alone and (b) global tracks, in simulation (red line) and data (black marker).*

the pattern recognition and track fitting are performed only in a small slice of the tracker (the ROI, *cf.* Section 3.4.2). The L3 isolation algorithm uses information from nearby pixel detector hits.

After each reconstruction level, a selection is applied on the reconstructed muon candidates. The main selection variables that can be used are the number of muon candidates in the event, their quality, p_{T}, η, impact parameter, and isolation variables. The trigger requirements are implemented in software modules called *filters*. A sequence of reconstruction steps and filters is called *trigger path*. Different trigger paths can be defined by varying the filter cuts. In such a way, the muon trigger can be specialised to fulfill the needs of different physics analyses. As an example, in Table 3.1 the requirements of four of the most basic trigger paths for 2010 data taking are listed.

It is important to stress that a trigger path is considered successful only if the requirements of all the three levels are satisfied. When a muon candidate passes a trigger level, all the candidates in the event are transmitted to the following level, even those that failed the selection. In particular, a muon candidate failing to pass the L1 filter of a given path may still be reconstructed at L2 and L3, if the event passes to the next trigger levels because of another trigger requirement; such a candidate (“volunteer”) is not considered for the trigger path which failed at L1.

In Section 3.8.1, muon reconstruction is described in the context of the HLT, stressing in particular the differences with the off-line reconstruction.

	HLT_Mu15	HLT_DoubleMu3
L1	$\geq$ 1 muon with $p_T > 7$ GeV/c, quality > 3	$\geq$ 2 muons with $p_T > 0$ GeV/c, quality ≥ 3
L2	$\geq$ 1 muon with $p_T > 7$ GeV/c	$\geq$ 2 muons with $p_T > 0$ GeV/c
L2 iso	N/A	N/A
L3	$\geq$ 1 muon with $p_T > 15$ GeV/c, $\lvert d_0\rvert \leq 2$ cm	$\geq$ 2 muons with $p_T > 3$ GeV/c, $\lvert d_0\rvert \leq 2$ cm
L3 iso	N/A	N/A

Table 3.1: *Thresholds and requirements of the basic muon triggers for 2010 data taking. The unsigned impact parameter, $|d_0|$, is calculated w.r.t. the beam spot. For the meaning of L1 quality, see [49]. Note that these paths do not include isolation requirements.*

3.8.1 Muon Reconstruction in the High Level Trigger

Level-2 Muon Seeding

The L2 muon reconstruction starts from an initial seed state. Unlike the off-line case, where seeds are obtained combining segments in the muon system, in the on-line reconstruction the L1 muon candidates are used as *external seeds*, with a significant reduction of seeding time. The full muon reconstruction is then performed on a regional basis, only where a L1 candidate is found. Although faster, this approach limits the HLT efficiency to the L1 efficiency: there cannot be a L2 muon reconstructed if no corresponding L1 muon object is present.

For each L1 muon candidate promoted by the GMT to the HLT, a L2 seed is built. An initial state is created from the position and momentum of the L1 candidate and fixed errors are assigned to all the parameters. Finally, the seed state is propagated to the innermost compatible muon chamber.

Level-2 Muon Trajectory Building

Starting from each L2 seed, the reconstruction of L2 tracks proceeds exactly as in the off-line case, described in Section 3.3. The local reconstruction and trajectory building are performed only in those regions of the muon system where a L1 candidate/L2 seed was built, in order to comply with the time requirements of the trigger. The flexibility of the software allows a variety of different reconstruction schemes: it is possible to configure which muon detectors to use, the direction and granularity of the pattern recognition, whether to apply the final fitting-smoothing step, etc. The configuration that is currently used is the same employed in the off-line reconstruction. It comprises two trajectory building steps: the first in the inside-out direction and using segments, the second in the opposite direction and using single hits.

Once the trajectories are built, ghost suppression is applied as described in Section 3.3.3, and a beam spot constraint is imposed (Section 3.3.4). Each trajectory preserves a link to its own seed, hence to the corresponding L1 candidate. This is particularly important to allow the suppression of volunteers.

A notable difference from the off-line reconstruction is present in the application of ghost suppression. This peculiar behaviour was expressly introduced to address a specific problem concerning volunteers, arising at cleaning level. A single muon can generate more than one L1 candidate, e.g. if the L1 trigger fails to merge candidates from different sub-detectors. In this case, several tracks will be produced, and the cleaner is designed to keep only one. Suppose e.g. that two L1 objects, t_1^a and t_1^b, are ghosts of the same muon, and only t_1^a passes the L1 trigger filter. The corresponding L2 tracks, t_2^a and t_2^b, share hits and undergo the usual ghost suppression algorithm. If the cleaner selects t_2^b, the L2 trigger filter will treat it as a volunteer and reject it. Figure 3.17 illustrates this mechanism. In this case, though, t_1^a-t_1^b and t_2^a-t_2^b represent the same muon candidate, and it is reasonable to use either L1 object to validate either L2 track. For this purpose, the cleaner produces a map that links each L2 track to the seeds of all its duplicates. In such a way, the L2 filter can accept a L2 track if any of the corresponding L1 candidates has passed the L1 filter. Figure 3.18 shows the gain in L2 reconstruction efficiency obtained using this strategy, compared with the efficiency of L2 seeding.

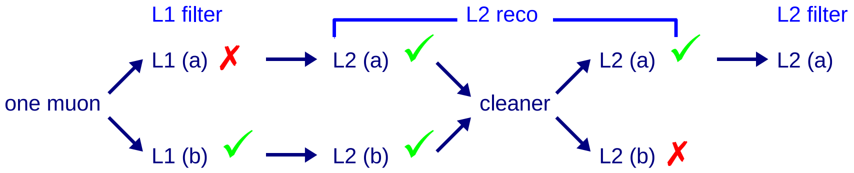

Figure 3.17: *The flowchart illustrates how the trajectory cleaner handles ghost L2 tracks. Without a special handling, the L2 filter rejects the L2(a) candidate, since the corresponding L1 failed. With the new strategy, a map links the two ghost L1 candidates, L1(a) and L1(b). Thus, the L2 filter uses the successful L1(b) to validate L2(a).*

Level-3 Muon Seeding

After the completion of Level-2 muon reconstruction and Level-2 filtering steps, the algorithm proceeds to reconstruct Level-3 muon candidates. In the HLT environment, the full tracker reconstruction cannot be performed because it is too CPU intensive. Therefore, track reconstruction is done in small regions of the central tracker corresponding to likely muon candidates.

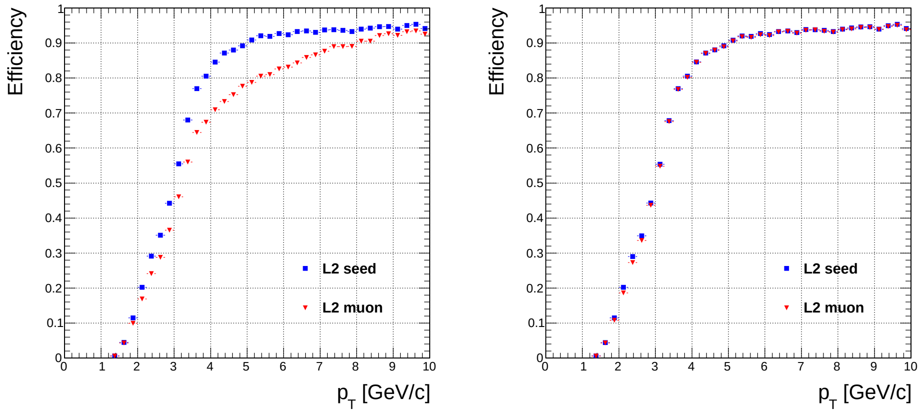

(a) (b)

Figure 3.18: *L2 reconstruction efficiency vs.* p_T *(a) without and (b) with the use of the mechanism described in Section 3.8.1 (in red), compared with the efficiency of L2 seeding (in blue). The L2 seeds are built from L1 candidates passing a* p_T *threshold of 3 GeV/c.*

This restrictive reconstruction is accomplished by a proper selection of trajectory seeds which limits the track reconstruction to a region consistent with the L2 muon, i.e. the ROI described in Section 3.4.2.

In the following paragraphs, different L3 seeding algorithms are described. The *hit-based seeds* use combinations of hits found on the tracker layers to estimate the initial position and direction. *State-based seeds*, instead, use a trajectory state, without information from the tracker measurements, to find the initial position and direction.

Hit-Based Seeding The inside-out hit-based seed option (*IOHit*) selects pairs or triplets of hits in the pixel detector, as in the off-line seeding (Section 3.4.1). The inner hit is required to be in the ROI. In the case of L2 muons with $|\eta| > 2$, the hit-pairs can be a combination of pixel and strip layers. In the outside-in hit-based seed option (*OIHit*), the L2 trajectory state is propagated to the outer tracker bound. From here, compatible measurements are looked for in TOB and TEC layers and used to update the predicted state from L2.

State-Based Seeding The track parameters obtained from the L2 measurement are propagated to the first compatible layer of the pixel detector (inside-out state-based seed or *IOState*) or to the outermost layer of TOB and TEC (outside-in state-based seed or *OIState*). The state given at the innermost (or outermost) layer of the tracker is used to proceed with pattern recognition from the inside-out (or outside-in).

Cascade algorithm Each of the L3 seeding algorithms described above performs differently in different parts of the detector and has advantages and disadvantages. For this reason, a combined seeding sequence is used in order to benefit from the advantages of each one, while minimising the disadvantages. Three of the four algorithms, the OIState, OIHit and IOHit, are run in a sequence, starting with the fastest (OIState) and finishing with the slowest (IOHit). In order to save CPU time, the slower algorithms are never called if the faster algorithms have a favourable outcome: if a L3 muon is successfully reconstructed from the seed, then the sequence for that L2 muon is stopped; otherwise, the sequence continues to the next seed generator and L3 reconstruction module.

Level-3 Muon Trajectory Building

Once the L3 seeding is completed, tracks are reconstructed in the tracker with the same procedure described in Section 3.4.1, only inside the ROI determined by each L2 muon. The best tracker tracks to be combined with a given L2 muon are then selected, following the same matching criteria as in the off-line reconstruction (*cf.* Section 3.4.2). Finally, for each L2-tracker match, a global fit is performed, using the whole set of hits in the tracker and muon system. If more than one global L3 track is built from the same L2 muon, only the one with the best χ^2 is kept. Thus, for each L2 muon, there is a maximum of one global L3 muon that is reconstructed.

In Figure 3.19, the efficiency of single-muon HLT path “Mu3” is shown as a function of η and p_{T}. The Mu3 path has no p_{T} cut at L1, and requires $p_{\mathrm{T}} > 3$ GeV/c at L2 and L3. The efficiencies are obtained with the tag-and-probe method, applied to muons from J/ψ and Z decays in data collected by CMS in 2010. The tags are defined by the the same requirements used in Section 3.7.1 for J/ψ (below $p_{\mathrm{T}} = 15$ GeV/c) and Z (above). The probes are required to be global muons, so these are trigger efficiencies with respect to off-line global muons. The on-line reconstruction efficiency is essentially equal to the off-line efficiency, thus the inefficiencies are introduced by the trigger requirements.

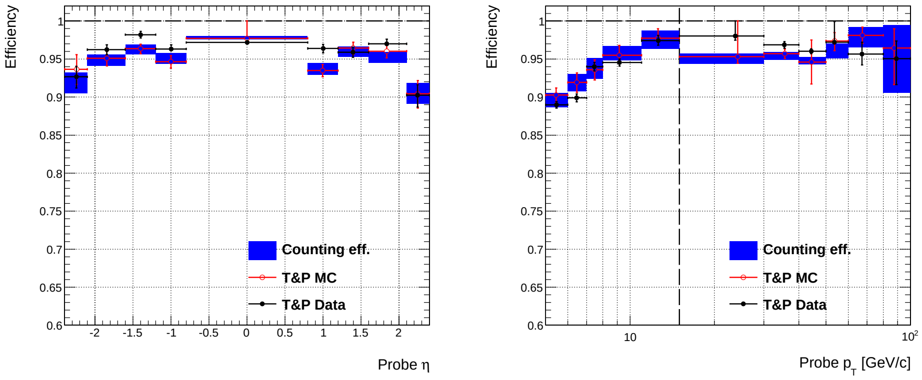

(a) (b)

Figure 3.19: *Efficiency vs. (a) η and (b) p_T (for $1.2 < |\eta| < 2.1$) of the HLT single-muon path Mu3. The efficiencies are obtained using the tag-and-probe method with J/ψ and $Z \to \mu^+\mu^-$ events, in simulation (red) and 2010 CMS data (black). The blue bands represent the counting efficiency of simulated signal events. Plot (a) is made using only muons from Z decays. Plot (b) is obtained using muons from J/ψ decays below 15 GeV/c, from Z decays above.*

Chapter 4

Momentum Scale Calibration

The CMS detector is designed to provide a reliable identification of tracks from pp collisions and a precise measurement of their momentum in the solenoidal magnetic field. The momentum measurement of charged particles is affected by systematic uncertainties due to the imperfect knowledge and modeling of the detector and magnetic field. Great effort is spent to ensure a precise alignment of the silicon sensors of the tracker [39] and of the muon chambers [40], a detailed description of the material budget in the detector [50] and of the magnetic field inside and outside the solenoid volume [26]. Nevertheless, residual effects can still lead to a systematic bias in the measurement of the track momentum and broaden its resolution. Moreover, the reconstruction algorithms used to fit the track trajectory can suffer from intrinsic biases (e.g. see Figure 3.9b). All these effects, if properly detected and quantified, can be absorbed by properly modeling a scale factor for the momentum as a function of the measured kinematic variables (p_{T}, η and ϕ).

An accurate calibration of track momentum and the investigation of residual systematic effects is essential in order to perform precision measurements, like top quark and W boson masses, B hadron spectroscopy, etc. This calibration is made feasible by the availability of reconstructed resonance decays, typically those involving two-body decays of neutral particles. The calibration procedure described in the following sections exploits all particles with an easily detectable decay to muon pairs: the J/ψ and $\psi(2S)$ mesons, the three narrow Υ states, and the Z^0 boson. The muon pairs originated from the decays of these particles have momenta in a range from a few GeV/c to a few hundred GeV/c, while they are hardly useful for a direct check of the momentum measurement of TeV-energy tracks. Nevertheless, they do constitute an invaluable tool to spot deficiencies in the Monte Carlo description of the detector, and their input is thus beneficial to improve the reconstruction of tracks of any momentum. They also allow a precise determination of track momentum resolution, whose knowledge is no less important than that of the momentum scale in several precision measurements.

The reference quantity which provides sensitivity, on an event-by-event basis, to the possible biases on the reconstructed muon track parameters is the parent's invariant mass. This is not a per-track variable, so a probabilistic approach is necessary in order to relate the difference between expected and observed mass with an hypothetical bias on the measured parameters of either or both daughter tracks. Once a set of functions describing the dependence of the bias and resolutions on track kinematics is established, the best estimate of the parameters of those functions can be determined from a likelihood minimisation, provided that a sufficient set of homogeneous data is used. An algorithm that uses this approach to correct the momentum of muons has been developed, and is described in detail in Section 4.1.

First, the algorithm mentioned above is used to find corrections for low p_T muons from J/ψ, up to about 10-15 GeV/c. This work is reported in Figure 4.2. The strategy to calibrate the momentum scale and measure the momentum resolution is developed using simulated J/ψ samples (Sections 4.2.2 and 4.2.3), then applied to about 19 pb^{-1} of J/$\psi \to \mu^+\mu^-$ events selected from 2010 CMS data (Section 4.2.4).

In order to calibrate the momentum of muons in a higher p_T range, Z $\to \mu^+\mu^-$ events can be exploited. In this case, the available statistics in data is clearly lower, so a simpler strategy has to be conceived. The calibration is applied both to tracker tracks and global tracks of muons. This work and its results are reported in Section 4.3.

4.1 The `MuScleFit` Algorithm

The `MuScleFit` algorithm [51][52] is conceived to correct the muon momentum measurement and determine its resolution, combining the reconstructed kinematics of the muon pair with the supposed knowledge of the parent particle species. Since the invariant mass of the muon pair depends on the scale of the muon momenta, the average difference between the reconstructed dimuon mass and the nominal resonance mass can be used to determine the momentum scale and its dependence on each muon kinematic variable. The algorithm is based on a multi-dimensional likelihood fit that uses as input the decay to muon pairs of the aforementioned resonances, along with some probability density functions describing the shape of each resonance, and a set of *ansatz functions* for correcting the muon momentum and estimating its resolution.

For a given resonance, the reconstructed mass distribution can be modelled as the theoretical line-shape, $\sigma(m;\, m_0)$, where m_0 is the nominal resonance mass, convoluted with a Gaussian to account for the detector resolution s:

$$P_{sig}(m, s) = \int dm' \, \frac{\sigma(m'; m_0)}{\sqrt{2\pi} s} \, e^{-\frac{(m'-m)^2}{2s^2}}. \tag{4.1}$$

Apart of a normalisation factor, Equation 4.1 can be regarded as the probability density function of muon pairs from decays of the resonance in question, with reconstructed mass m and mass resolution s. In Figure 4.1, the probability density functions for J/ψ and Z are shown. Since the nominal J/ψ width is very small, i.e. less than 100 keV [21], the intrinsic J/ψ line-shape is modelled with a very narrow ("δ-like") function, plus a triple-exponential tail extending towards low masses, which accounts for the effect of the *final state radiation*. The Z line-shape instead is modelled with the HORACE Monte Carlo generator [53], which includes the exact $\mathcal{O}(\alpha)$ electroweak calculation plus higher order QED corrections. As explained above, the models are then convoluted with a Gaussian of given width s.

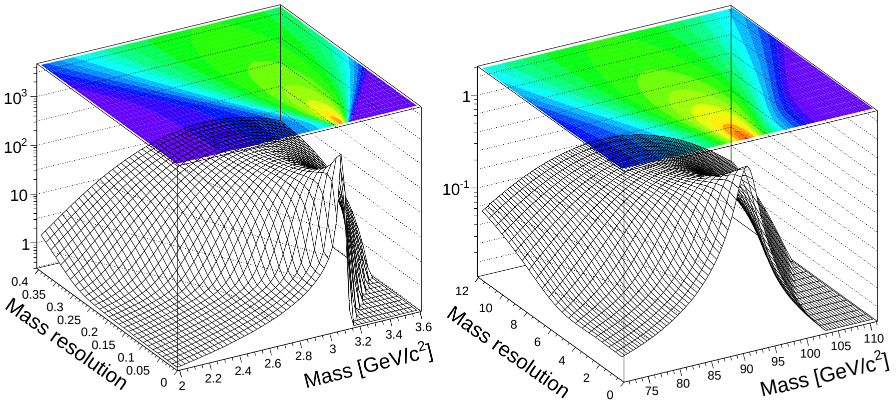

(a) **(b)**

Figure 4.1: *Probability density functions for* J/ψ *and Z resonances.*

An ansatz function is needed to parametrise the momentum scale correction

$$p_T^{corr} = F(\mathbf{x}; \mathbf{a}) \cdot p_T, \tag{4.2}$$

where the vector $\mathbf{x}$ contains the kinematic variables on which the p_T bias is found to be dependent, usually (p_T, ϕ, $\cot\theta$), and $\mathbf{a}$ is the set of free parameters of the function. Other ansatz functions are used to parametrise the resolution of each kinematic variable x_i

$$\sigma(x_i) = G_i(\mathbf{x}; \mathbf{b}_i) \tag{4.3}$$

and will depend on as many sets of parameters. A last function is introduced to model the non resonant background shape: $P_{bkg}(m; \mathbf{c})$.

Given a muon pair, with kinematics defined by $\mathbf{x}_a$ and $\mathbf{x}_b$, the momenta of the two muons are corrected accordingly to Equation 4.2 and the invariant mass of the pair is computed:

$$m_{a,b} = m(p^{corr}_{\mathrm{T},a},\, \phi_a,\, \cot\theta_a;\, p^{corr}_{\mathrm{T},b},\, \phi_b,\, \cot\theta_b). \tag{4.4}$$

The mass resolution of the muon pair can be formally written, neglecting the covariance terms, as

$$s_{a,b} = \sqrt{\sum_{\alpha=a,b} \sum_{i=1}^{3} \left(\frac{\partial m}{\partial x_i}\right)^2 \sigma^2(x_{i,\alpha})}\,, \tag{4.5}$$

where $\sigma(x_{i,\alpha}) = G_i(\mathbf{x}_\alpha;\, \mathbf{b}_i)$. Under the hypothesis that the muon pair comes from the decay of a given resonance, the event can be assigned a probability $P_{sig}(m_{a,b},\, s_{a,b})$, accordingly to Equation 4.1.

From a sample of dimuon events, assumed to originate from decays of the chosen resonance, a likelihood function can be defined as

$$-\ln L = -\sum_{k=1}^{N_{evt}} \ln\left[f_{sig} \cdot P_{sig}(m_k, s_k) + (1 - f_{sig}) \cdot P_{bkg}(m_k)\right] \tag{4.6}$$

where m_k and s_k are computed with the measured muon momenta of event k and are functions of $\mathbf{a}$, $\mathbf{b}_i$ and $\mathbf{c}$; f_{sig} is the fraction of signal events and is a nuisance parameter in the fit. The minimisation of $-\ln L$ with respect to all these parameters allows the simultaneous determination of scale, resolution and background modelling, given the observed distribution of the reconstructed dimuon mass in the sample. The fit to the parameters can be repeated to check its stability. The algorithm even allows to perform a multi-resonance fitting, taking into account more than one resonance at a time and the corresponding backgrounds.

Mass Resolution

Equation 4.5 is used in `MuScleFit` to compute the resolution of the dimuon invariant mass from the resolution of the kinematic variables of each muon. This formula is valid under the assumption that the covariance between each pair of variables gives a negligible contribution to the mass resolution. The complete expression is

$$s_{a,b} = \sqrt{\sum_{\alpha,\beta=a,b} \sum_{i,j=1}^{3} \frac{\partial m}{\partial x_{i,\alpha}} \frac{\partial m}{\partial x_{j,\beta}} \sigma(x_{i,\alpha},\, x_{j,\beta})}\,, \tag{4.7}$$

where $\sigma(x_{i,\alpha},\, x_{j,\beta})$ is the covariance between the observables x_i of muon α and x_j of muon β. It is implied that $\sigma(x_{i,\alpha},\, x_{i,\alpha}) = \sigma^2(x_{i,\alpha})$ is the variance of the observable x_i of muon α.

In Figure 4.2, the variance of the J/ψ mass, $\sigma^2(m) = s^2_{a,b}$, is shown as a function of η and p_T of the muon tracks, along with the separate contributions from the variances of each kinematic variable, $(\partial m/\partial x_i \cdot \sigma(x_i))^2$, where $x_i = p_\mathrm{T}$, $\cot\theta$ and ϕ. The mass variance is clearly dominated by the muon p_T term, while the $\cot\theta$ and ϕ contributions are two orders of magnitude lower. In Figure 4.3a, the absolute value of the $p_{\mathrm{T},a}$-$p_{\mathrm{T},b}$ covariance term is shown, and in Figure 4.3b the sum of all the remainder covariances, again in absolute value. $\sigma(p_{\mathrm{T},a},\, p_{\mathrm{T},b})$ is the most relevant covariance, and its contribution to $\sigma^2(m)$ is of the same order as $\sigma^2(\cot\theta)$ and $\sigma^2(\phi)$ or higher, especially in the high $|\eta|$ regions.

Since the mass resolution $\sigma(m)$ is largely dominated by the p_T resolution $\sigma(p_\mathrm{T})$, some features of the ansatz function $\sigma(p_\mathrm{T})/p_\mathrm{T}$, in particular its dependence on muon kinematics, can be deduced directly from the mass resolution on data.

Although ϕ and $\cot\theta$ resolutions and all covariances are orders of magnitude lower than $\sigma(p_\mathrm{T})$, their contribution may be relevant with sufficient statistics, i.e. when the likelihood fit becomes sensitive to details of the mass resolution of the same order. In particular, this is the case for J/ψ, as will be shown in Section 4.2.3.

4.2 Momentum Scale Calibration Using J/ψ

J/$\psi \to \mu^+\mu^-$ decays represent the largest source of dimuons in the early data taking. In order to be identified, the muons must reach the muon stations, and this implicitly imposes a transverse momentum threshold of about 3 GeV/c in the barrel (see Figure 3.10). Therefore, the transverse momentum and pseudorapidity of the muons coming from low-momentum J/ψ are highly correlated, with the low p_T muons populating only the endcap region.

4.2.1 Signal Selection

Since the muon momentum resolution is dominated by the tracker fit up to $p_\mathrm{T} \simeq 200$ GeV/c (see Figure 3.11), in the present analysis only the track built with the silicon hits is considered for the momentum scale and resolution measurement, also for muons reconstructed by the global algorithm. In such a way, global and tracker muons can be analysed together.

The global muon algorithm (Section 3.4) provides pure identification and good quality track reconstruction, but low efficiency at low momentum. Therefore, in the selection of J/ψ candidates, muons reconstructed by the tracker muon algorithm (Section 3.5) are also considered: if a global muon pair satisfying the selection requirements is not found in an event, also global-tracker and tracker-tracker muon pairs are subsequently searched for. This approach increases the efficiency at low p_T, but leads to a larger

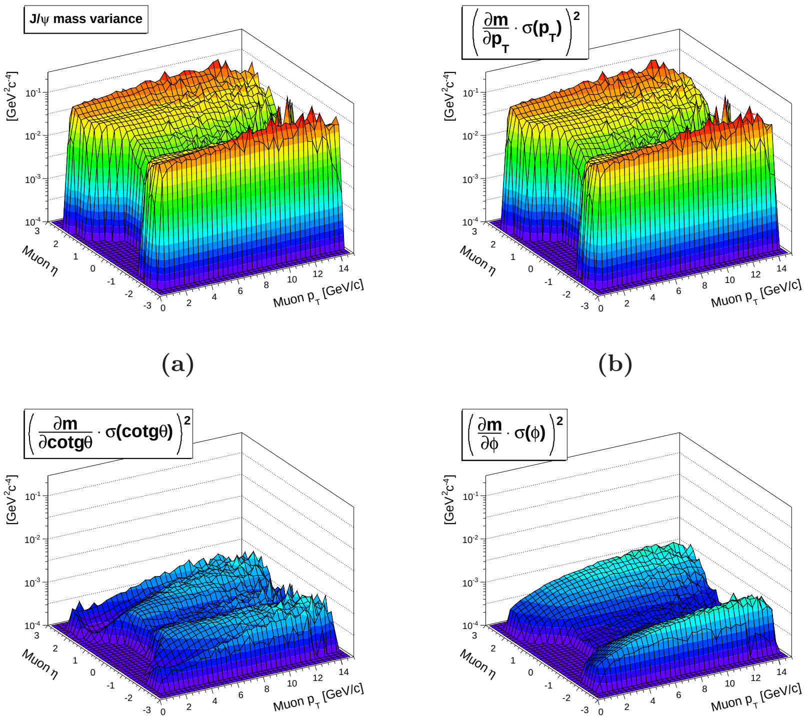

(a) (b) (c) (d)

Figure 4.2: *(a) Variance of the* J/ψ *mass vs.* η *and* p_{T}*; contributions to* $\sigma^2(m)$ *from (b)* p_{T}*, (c)* $\cot\theta$ *and (d)* ϕ*.*

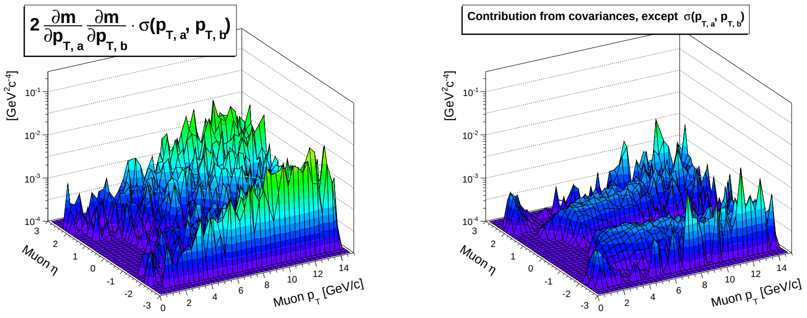

(a) (b)

Figure 4.3: *Contribution to the variance of the* J/ψ *mass from (a)* $\sigma(p_{\mathrm{T},a}, p_{\mathrm{T},b})$ *and (b) all the other covariances, in absolute value.*

background from punch-through and decays in flight of hadrons. Further selection for tracker muons is thus necessary.

An initial suppression of beam background is performed by applying the following quality cuts to each event:

- at least one vertex of good quality, with a number of degrees of freedom > 4, longitudinal position $|z| < 15$ cm and transverse position $r < 2$ cm;
- if more than ten tracks are reconstructed, at least 25% of them must be of "high-purity" quality, i.e. satisfy quality requirements described in [29]

The inner tracker track of each muon is required to pass the following selection:

- number of hits in the silicon detectors > 11;
- number of hits in the pixel detector > 1;
- normalised χ^2 of the track fit < 4;
- transverse impact parameter $|d_0| < 3$ cm and longitudinal impact parameter $|d_z| < 30$ cm.

In order to ensure a high purity sample, tracker muons are further selected by requiring a satisfactory matching in direction and position between the track extrapolated from the inner tracker and the segments reconstructed in the muon stations (*cf.* Section 3.5). For global muons, the combined fit of tracker and muon hits must have a normalised $\chi^2 < 20$.

When a pair of opposite sign muons satisfy the above requirements, their tracks are fitted together to reconstruct a common vertex. The resulting J/ψ candidate is retained if the normalised χ^2 of the fit has a probability above 0.1%.

The dimuon invariant mass spectrum obtained with ~ 19 pb^{-1} integrated luminosity after the above selection is shown in Figure 4.4.

The invariant mass distribution of the selected muon pairs is divided into bins of the main kinematic variables of the single tracks and fitted with a *Crystal-Ball* function [54], summed with an exponential for the background. The Crystal-Ball mean and standard deviation for each bin provide an estimation of the scale and resolution, respectively, for that kinematic configuration. The scale and resolution of single tracks, instead, are obtained using the `MuScleFit` algorithm, as explained in Section 4.1. Throughout this chapter, whenever J/ψ quantities are shown *vs.* single track variables, the distributions are filled twice per event, using both muons.

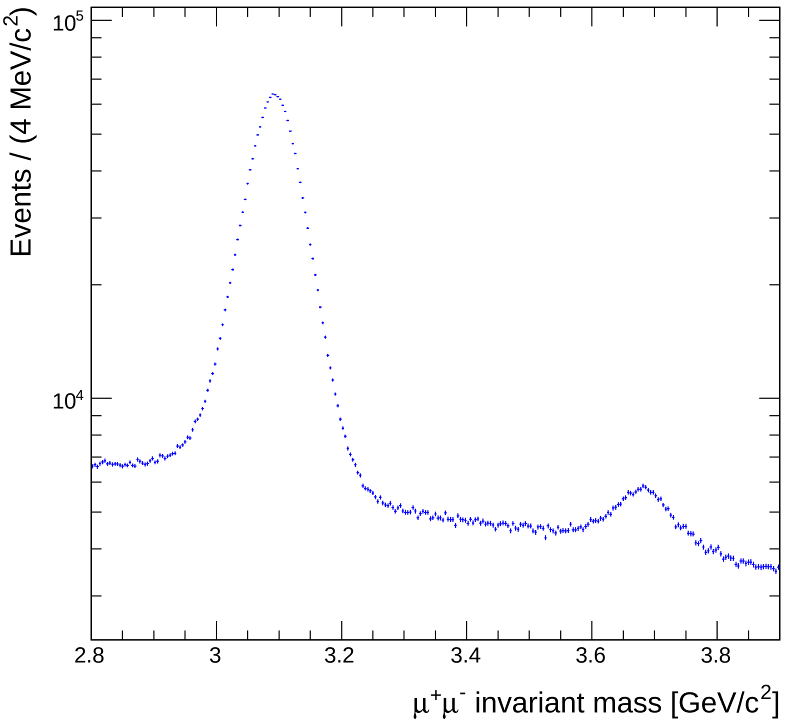

Figure 4.4: *$\mu^+\mu^-$ invariant mass spectrum after the selection described in Section 4.2.1, for an integrated luminosity of about 19 pb^{-1} and a centre-of-mass energy of 7 TeV. The J/ψ and $\psi(2S)$ peaks are visible.*

4.2.2 Preliminary Studies on Simulated J/$\psi \to \mu^+\mu^-$ Events

Before applying the `MuScleFit` algorithm on LHC collision data, preliminary studies are performed using simulation, in order to assess the effects of material modeling, magnetic field, alignment and reconstruction algorithms on the momentum scale. Simulated J/$\psi \to \mu^+\mu^-$ decays with systematically altered detector configurations help in disentangling the different sources of momentum bias, and motivate the assessment of each potential cause individually. The simulated data samples are reconstructed perturbing, one by one, the relevant detector parameters, and the changes in J/ψ mass and width are studied as functions of the muon kinematic variables. The description of these preliminary studies can be found elsewhere [55]. In the following, a brief summary of the main results is reported.

Detector Material Description The reconstruction algorithm is based on an approximated description of the material budget. Such approximation, combined with other systematics in the reconstruction algorithm, introduces biases with complicated patterns and magnitude of up to 0.1% (Figure 4.5a), especially in the transition and endcap regions, where the amount of material is larger and not uniform. The distribution of materials is also responsible for the dependence of the momentum resolution on pseudorapidity (Figure 4.5b). To assess the sensitivity of reconstruction to such approximations, different models [50] were used, with different amounts of material. In Figure 4.5, the standard material budget is compared with a model having about 8% more material, in terms of radiation length. The difference in J/ψ mass is found to be of the order of 1-2 MeV/c^2, uniform in η. The mass resolution is only slightly broadened.

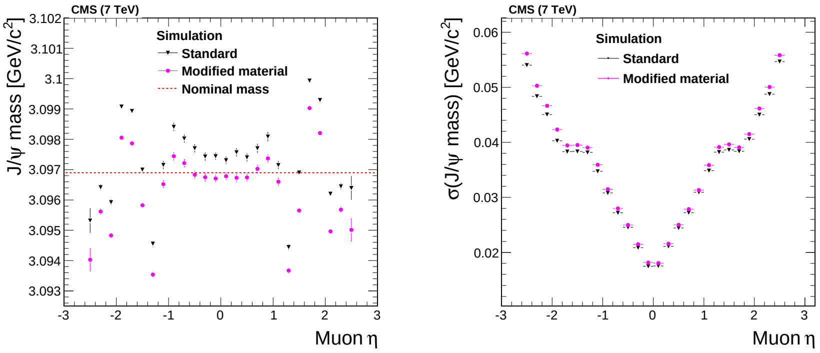

(a) (b)

Figure 4.5: *(a)* J/ψ *mass and (b) mass resolution as functions of* η*, for the standard material budget model (black triangles) and for a modified model with a larger amount of material (magenta circles). The mass and resolution are estimated as the peak and* σ *of a Crystal-Ball fit.*

Magnetic Field To study the effect of the description of the magnetic field, the standard model used in CMS was compared with a different map, based on a parametrisation, with differences of up to 0.1% [26][56]. The main effect of the modified map is to introduce a bias increasing with $|\eta|$, from 0.01% in the barrel to 0.1% in the endcaps, indicating that the reconstruction is more sensitive to possible errors in the magnetic field mapping at high $|\eta|$ and low p_{T} (see Figure 4.6). No relevant differences are found instead in mass resolution.

Misalignment To study the systematic effects related to detector misalignment, the "ideal" and "start-up" alignment scenarios (*cf.* Section 3.1) are compared. The start-up misalignment introduces a small mass bias (< 1 MeV/c^2) for low muon p_{T} and high $|\eta|$, and degrades the mass resolution, especially at high p_{T} (Figure 4.7). The most notable effect of misalign-

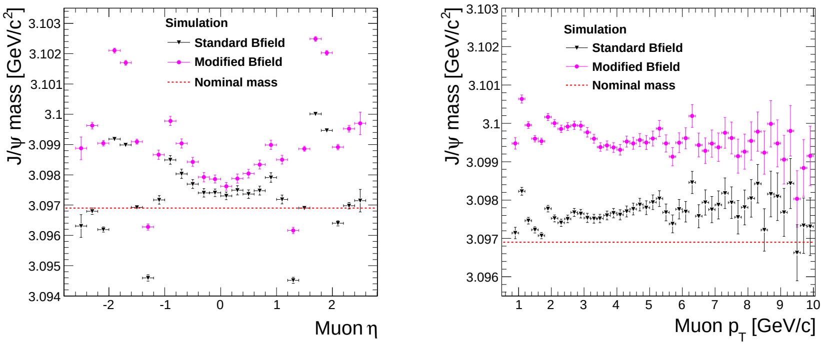

(a) **(b)**

Figure 4.6: J/ψ *average mass as a function of (a)* η *and (b)* p_{T}*, for the nominal magnetic field map and for the modified one.*

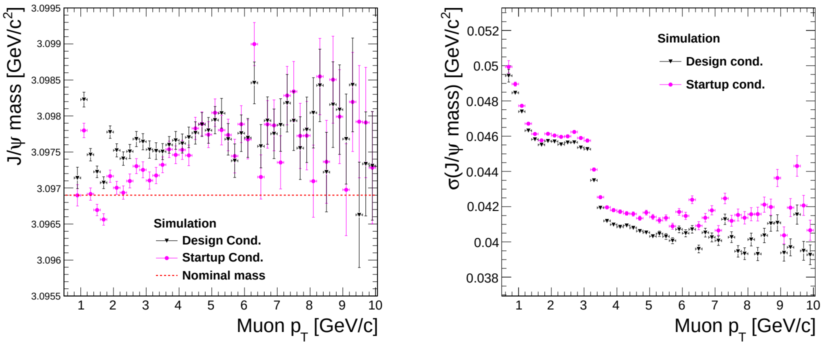

(a) **(b)**

Figure 4.7: *(a)* J/ψ *mass and (b) mass resolution as a function of* η p_{T} *of both muons in an event, for the ideal (black triangles) and start-up alignment scenarios (magenta circles). Mass and resolution are estimated as the peak and width of a Crystal-Ball fit. The largest biases are found at low* p_{T}*, while the degradation in resolution increases with the muon* p_{T}*.*

ment is a large bias in ϕ. This effect becomes visible when plotting the J/ψ mass as a function of the ϕ angle of positive and negative charged muons separately. As an example, Figure 4.8 shows the J/ψ mass for $\phi(\mu^{+})$ and $\phi(\mu^{+})$, for ideal conditions (in black) and for a modified geometry containing a *radial* distortion (in red), corresponding to a transformation $\Delta r = k \cdot r$ in the radial coordinate. A sinusoidal-like bias is observed, with opposite phase for μ^{+} and μ^{-}. When the distributions for μ^{+} and μ^{-} are plotted together, as explained in previous section, the opposite effects cancel out. Hence, in all the studies presented in this chapter, the ϕ-dependance of bias and resolution will be always analysed separately for positive and negative muons.

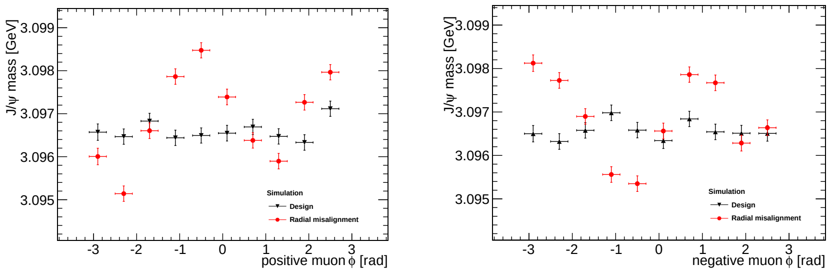

(a) **(b)**

Figure 4.8: J/ψ *average mass as a function of the azimuthal angle* ϕ*, separately for (a) positive and (b) negative muons, for a perfectly aligned geometry (black triangles) and for the case of a radial distortion (red circles).*

4.2.3 Calibration with a Realistic Scenario

After the dedicated studies described above, the `MuScleFit` calibration strategy is tested using simulations with realistic conditions: a sample of simulated prompt J/$\psi \rightarrow \mu^+\mu^-$ events at 7 TeV energy, corresponding to an integrated luminosity of about 13 pb^{-1}, is reconstructed with the detector alignment and calibration scenarios reproducing the conditions at the moment of the start of data taking. The transverse momentum bias and the resolution on the kinematic variables of the simulated muons before the correction (e.g., *cf.* Figure 4.9) are used to build sensible ansatz functions for the fit. Note that the bias and resolution of the dimuon mass reflect closely the bias and resolution of the single muon p_{T} (e.g. compare the black graphs in Figures 4.5a and 4.5b with Figures 4.9a and 4.9b, respectively). Thus, the dependence of the p_{T} ansatz functions on the muon kinematics can be directly deduced from mass distributions in data (*cf.* considerations in Section 4.1).

The transverse momentum resolution is modelled with the following function

$$\frac{\sigma(p_T)}{p_T} = \begin{cases} f(p_{\mathrm{T}}) + a_3 + a_4\,\eta^2 & \text{for} \quad |\eta| \le a_0 \\ (|\eta| - a_0)\,(y_2 - y_1)/(a_1 - a_0) + y_1 & \text{for} \quad a_0 < |\eta| \le a_1 \\ f(p_{\mathrm{T}}) + a_5 + a_6\,(|\eta| - a_7)^2 & \text{for} \quad a_1 < |\eta| \le a_2 \\ f(p_{\mathrm{T}}) + a_8 + a_9\,(|\eta| - a_{10})^2 & \text{for} \quad |\eta| > a_2 \end{cases}, \tag{4.8}$$

where $f(p_{\mathrm{T}}) = a_{11}\,p_{\mathrm{T}}$ for $|\eta| < 1.4$ and 0 otherwise. The values of y_1 and y_2 are chosen such that the region with $a_0 < |\eta| \le a_1$ is described by a line connecting the two adjacent parabolas, that is $y_1 = a_3 + a_4\,a_0^2$ and $y_2 = a_5 + a_6\,(a_1 - a_7)^2$.

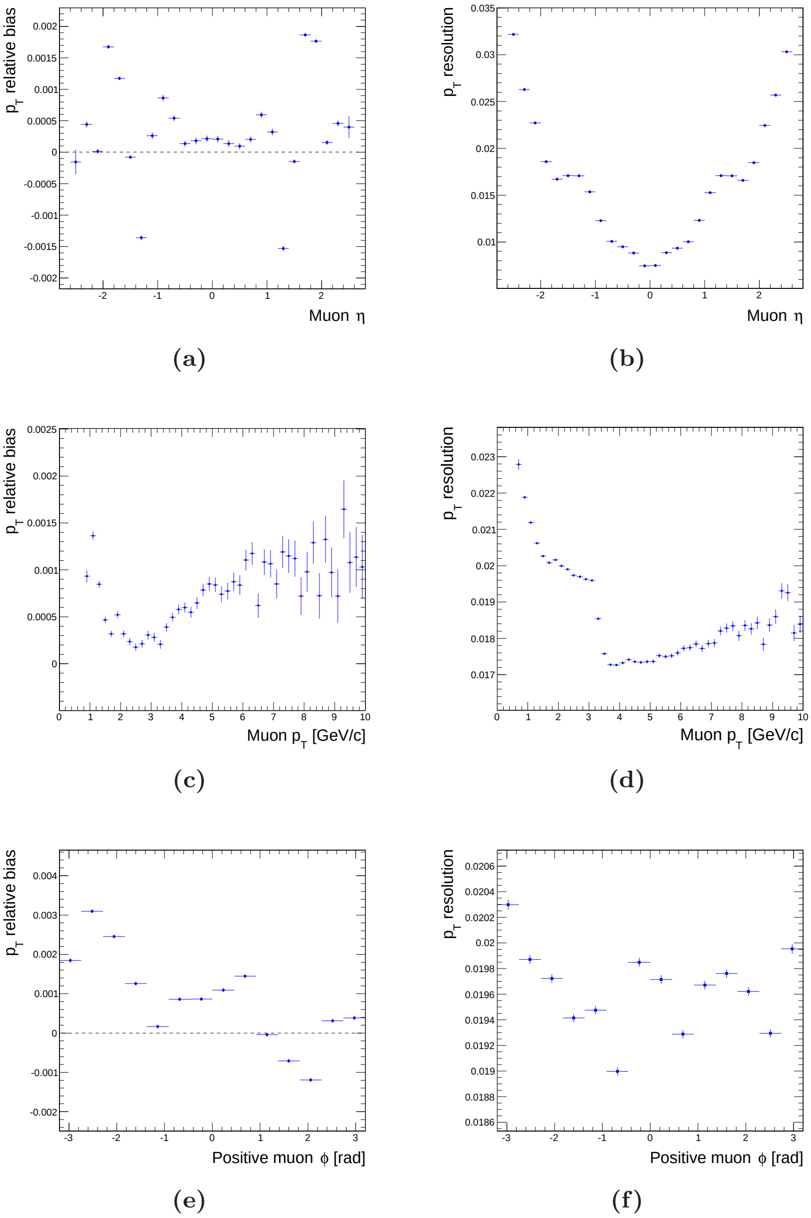

(a) **(b)**

(c) **(d)**

(e) **(f)**

Figure 4.9: *Muon* p_{T} *relative bias (left) and resolution (right) as functions of muon* η *(above),* p_{T} *(centre) and* ϕ *of the positive charged muon (below), for a sample of prompt* J/ψ *simulated with a realistic start-up scenario, before calibration.* p_{T} *relative bias and resolution are defined as the mean and width of a Gaussian fit to the distribution of* $R_{\mu}(p_{\mathrm{T}})$*, according to the definition given in Equation 3.2.*

The resolution on the polar angle is parametrised from the Monte Carlo truth as

$$\sigma(\cot\theta) = 9.9\cdot 10^{-4} - 2.3\cdot 10^{-4}\,|\eta| - 5\cdot 10^{-4}\,\eta^2 + 10.7\cdot 10^{-4}\,|\eta|^3$$

and the resolution on the azimuthal angle is fitted to an average value $\sigma(\phi) = a_{12}$.

The function used for the momentum correction is

$$p_{\mathrm{T}}^{corr} = p_{\mathrm{T}}\cdot\left(1 + A + B\,f(|\eta|) + C_{q,h}\,|\phi|\,\sin(2\phi + D_{q,h})\right)\,, \tag{4.9}$$

where $f(|\eta|)$ is tabulated from the actual mass distribution *vs.* muon $|\eta|$, subtracting the mean of the function over $|\eta|$, and has hence an average value of zero. The parameters $C_{q,h}$ and $D_{q,h}$ are different for positive and negative charge ($q = +,\, -$) and for $\phi > 0$ or $\phi \leq 0$, i.e. for the upper or lower half of the CMS detector ($h = u,\, l$). The total number of free parameters is ten. The fit strategy is to first fit the resolution and, in a second iteration, the scale correction.

In Figure 4.10, the J/ψ mass is shown as a function of η, p_{T}, ϕ of μ^+ and ϕ of μ^-, before and after the correction procedure. The biases are clearly reduced and the mass distribution is generally shifted towards the nominal value, with maximum discrepancies within 1–2 MeV/c^2. The limit on the correction is due to the choice of rather simple functions. The results can be improved by further refining the description of the biases.

The result of the resolution fit is shown in Figure 4.11 for the dimuon mass (a, b) and muon p_{T} (c, d). The mass resolution fit is in good agreement with the Monte Carlo expectation, except for small residual discrepancies at low p_{T} and high $|\eta|$. The p_{T} resolution fit, instead, shows larger discrepancies in all the p_{T} range. A detailed study showed that such discrepancies result from the covariance terms neglected in Equation 4.8, especially the covariance between the p_{T} of the two muons (*cf.* Section 4.1). The correct treatment would be to include all the covariance terms in the computation of the mass resolution, along with appropriate ansatz functions to parametrise them. However, this would increase the number of free parameters and make the fit overly complicated. Since the effect is reasonably small, the difference between the p_{T} resolution from the fit and the Monte Carlo truth can be assigned as a systematic error to the resolution measurement on data.

4.2.4 Calibration with 7 TeV Data

The calibration procedure described in the previous section is applied to a sample of dimuon events from the first year's collision data at 7 TeV centre-of-mass energy, corresponding to about 19 pb^{-1} of integrated luminosity.

One additional difficulty with respect to the simulation is the presence of the background. Even after the signal selection described in Section 4.2.1,

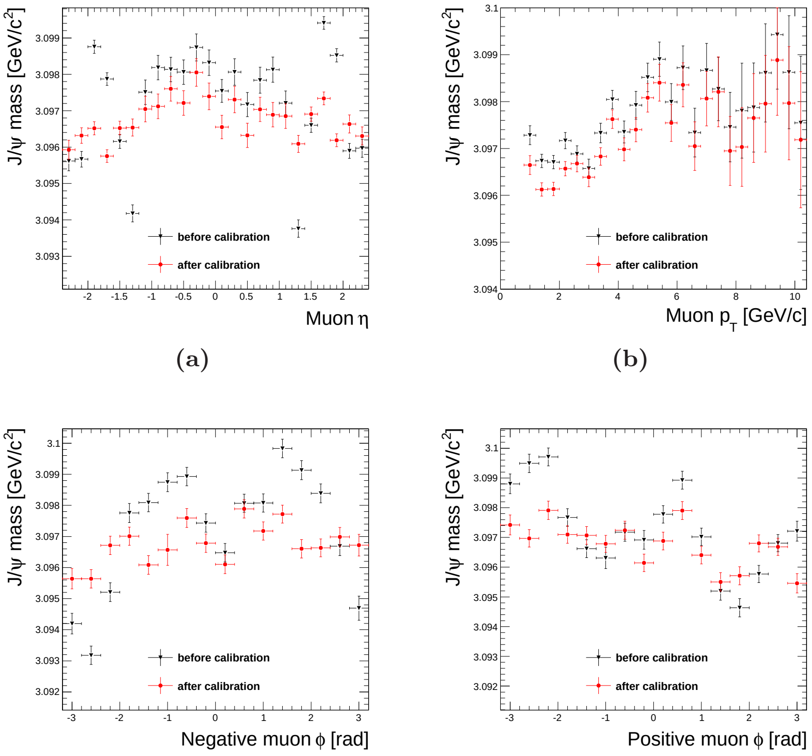

(a) **(b)** **(c)** **(d)**

Figure 4.10: *J/ψ mass vs. (a) η, (b) p_{T}, (c) ϕ of μ^- and (c) ϕ of μ^+, before and after the calibration with `MuScleFit`.*

the background level is high and varies significantly with the J/ψ and muon kinematics. In Figure 4.12, the dimuon invariant mass is fitted, in each bin of muon η, with a convolution of a Crystal-Ball function and an exponential of the form $e^{k \cdot m}$, to account for the background shape: for each bin, the fraction of signal events f_{sig} (*cf.* Equation 4.6) is reported in Figure 4.12a, and the parameter k in Figure 4.12b. The amount of background and its shape show a strong dependence on the pseudorapidity. Thus, different exponential functions must be adopted in different $(\eta(\mu_1), \eta(\mu_2))$ regions.

In Figures 4.13 and 4.14, the measured J/ψ mass and width are compared in data and simulation, before the calibration. Mass and width are obtained as the peak value and σ of a Crystal-Ball fit in each bin, plus an exponential for the background. A shift up to 6 MeV/c^2 is observed in the mass distributions, especially at high pseudorapidity and low momentum. In the same regions, the resolution in data is up to 10% worse than in simulation.

The likelihood fit is performed assuming the same ansatz functions used

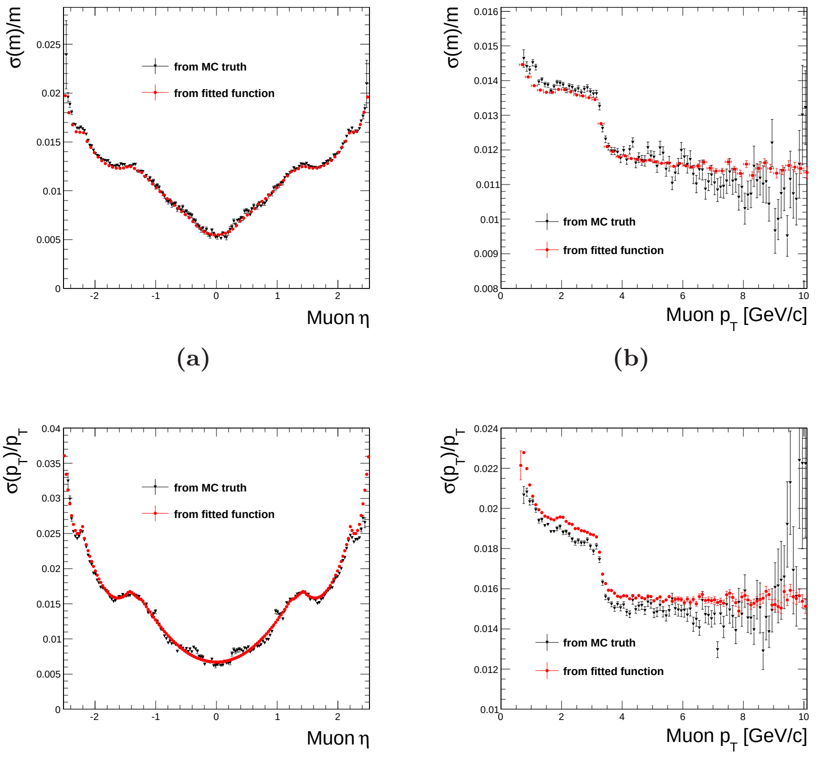

(a) **(b)**

(c) **(d)**

Figure 4.11: J/ψ *mass relative resolution (above) and* p_{T} *relative resolution (below) vs. muon* η *(left) and* p_{T} *(right), as obtained from the Monte Carlo truth (in black) and from the fitted ansatz functions (in red).*

in Section 4.2.3 for the simulated samples. These parametrisations of scale and resolution are motivated by the largest effects seen in the Monte Carlo studies (Section 4.2.2) and in the analysis of the mass average and width in data (Figures 4.13 and 4.14). The fit strategy is the same adopted with the simulated samples: first the background is determined in each η bin, then the momentum resolution is fitted with Equation 4.8 and finally the momentum scale correction is determined and applied to each muon using Equation 4.9.

The results of the momentum scale fit are reported in Table 4.1a. In Figure 4.15, the dimuon invariant mass is shown before and after the momentum calibration and fitted with the sum of a Crystal-Ball and a Gaussian having the same mean value, plus an exponential for the background. After the scale correction, the initial value of the mass peak is shifted by about 3 MeV/c^2 in the right direction. The corrected mass, (3094.97 ± 0.05) MeV/c^2, still differs from the nominal value, (3096.916 ± 0.011 MeV/c^2) MeV/c^2 [21].

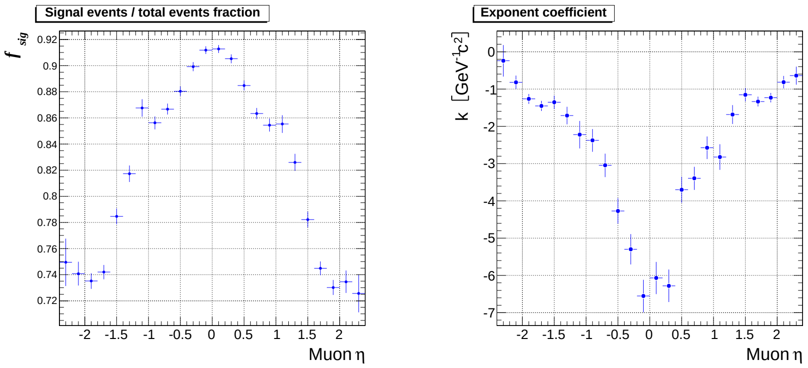

(a) **(b)**

Figure 4.12: *(a) Signal fraction f_{sig} and (b) k parameter vs. η, obtained by fitting the dimuon invariant mass distribution in each bin with a Crystal-Ball and an exponential $e^{k \cdot m}$.*

It should be noted, though, that the fit with a Crystal-Ball function is not expected to return the exact value: applying it to the J/ψ line-shape model described in Section 4.1, which includes a tail due to the final state radiation (see Figure 4.1a), a shift of a few MeV/c^2 is found, with a linear dependence on the mass resolution. Given the resolution observed in data, a shift around 2 MeV/c^2 is expected. Therefore, the mass value extracted from data after the corrections is perfectly compatible with the nominal value.

The modelling of the final state radiation tail in the J/ψ mass line-shape represents the main source of systematic uncertainty in the scale correction. Such uncertainty has been estimated, in a conservative way, by comparing the results of a Crystal-Ball fit to the used line-shape and to a model with a simplified FSR tail. The difference has been found to be below 1 MeV/c^2, corresponding to an effect lower than $1.5 \cdot 10^{-4}$ on the momentum scale.

Figure 4.16 shows the J/ψ mass as a function of the muon kinematics, before and after the scale corrections. The mass values after the corrections are in good agreement with the expected ones. Again, the shift due to the use of Crystal-Ball fits must be considered, which can be as large as 2-3 MeV/c^2 in the phase-space regions where the mass resolution is worse, i.e. at high $|\eta|$ and low p_{T}. However, all the distributions are flatter than those before the corrections and the largest biases are recovered, in particular in the endcap regions and for $p_{\mathrm{T}} < 3$ GeV/c. The ϕ modulations observed for separate charges are also partly recovered.

The result of the transverse momentum resolution fit is reported in Table 4.1b and the fitted function is shown in Figure 4.17, along with the corresponding result obtained on simulated data. As already observed in Figure 4.13, a discrepancy up to 10% in the transverse momentum resolu-

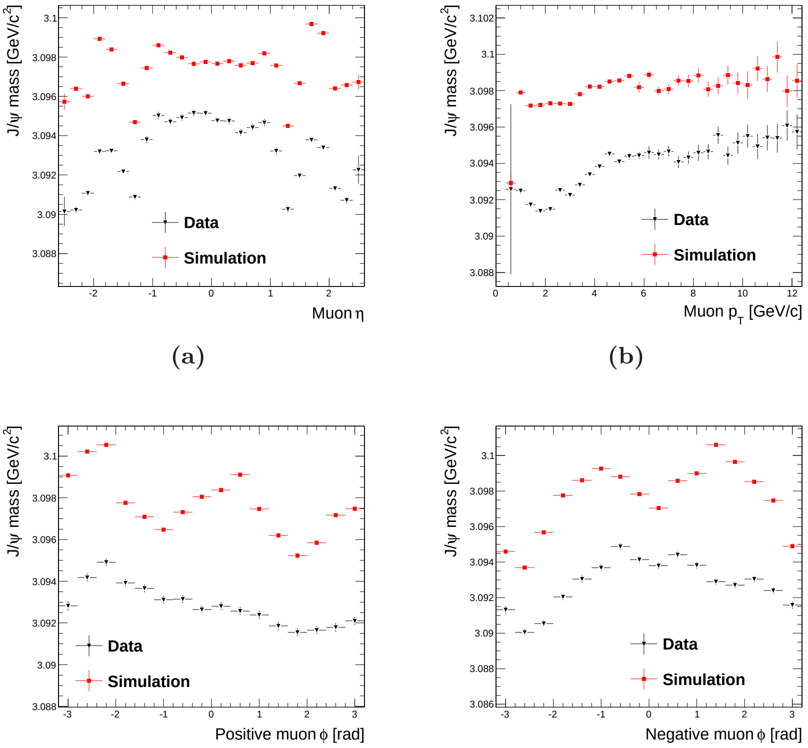

(a) **(b)**

(c) **(d)**

Figure 4.13: *Measured* J/ψ *mass in data (black) and simulation (red) vs. (a)* η*, (b)* p_{T}*, (b)* ϕ *of positive muon and (c)* ϕ *of negative muon, before the calibration.*

tion is found between data and simulation, mainly in the high $|\eta|$ and low p_{T} region.

The systematic uncertainties coming from the choice of the parametrisation function can be estimated from the Monte Carlo exercise described in Section 4.2.3: the maximum difference between the p_{T} resolution fitted on simulated data and that extracted from the Monte Carlo truth is about 20% in the barrel and 5% in the endcaps. In Figure 4.17, the sum of the systematic and statistical errors is represented by the gray band.

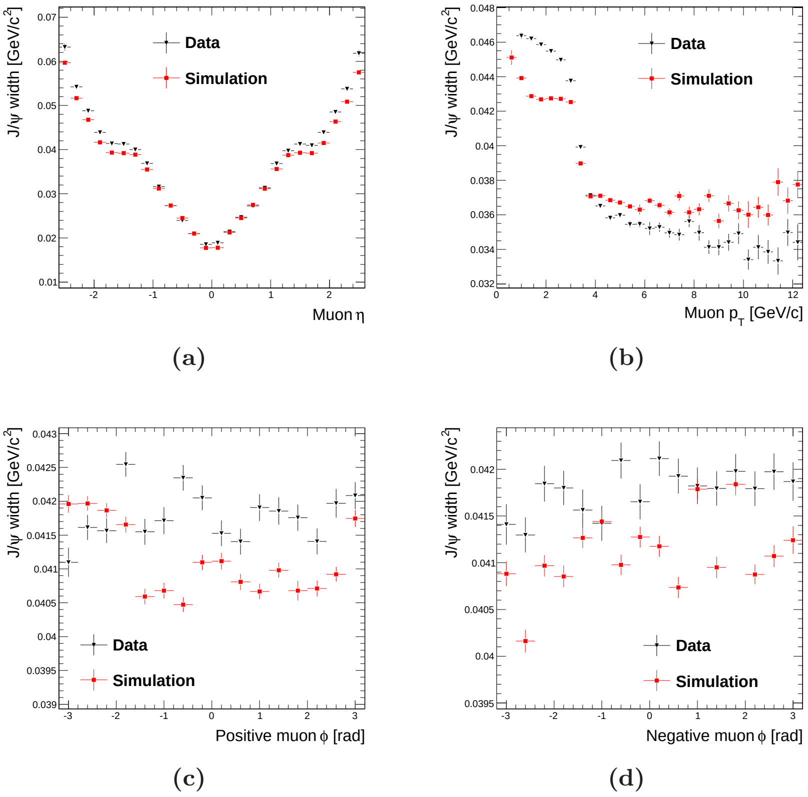

Figure 4.14: *Measured* J/ψ *width in data (black) and simulation (red) vs. (a)* η*, (b)* p_{T}*, (b)* ϕ *of positive muon and (c)* ϕ *of negative muon, before the calibration.*

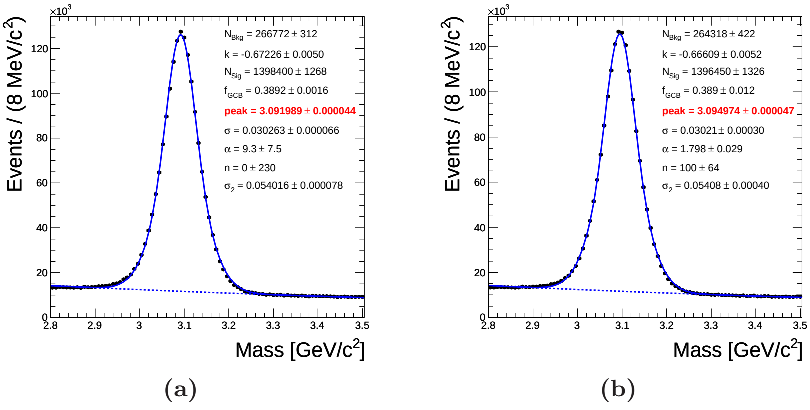

Figure 4.15: *Measured dimuon invariant mass spectrum, (a) before and (b) after the scale correction, fitted with the sum of a Crystal-Ball function and a Gaussian, plus an exponential for the background.*

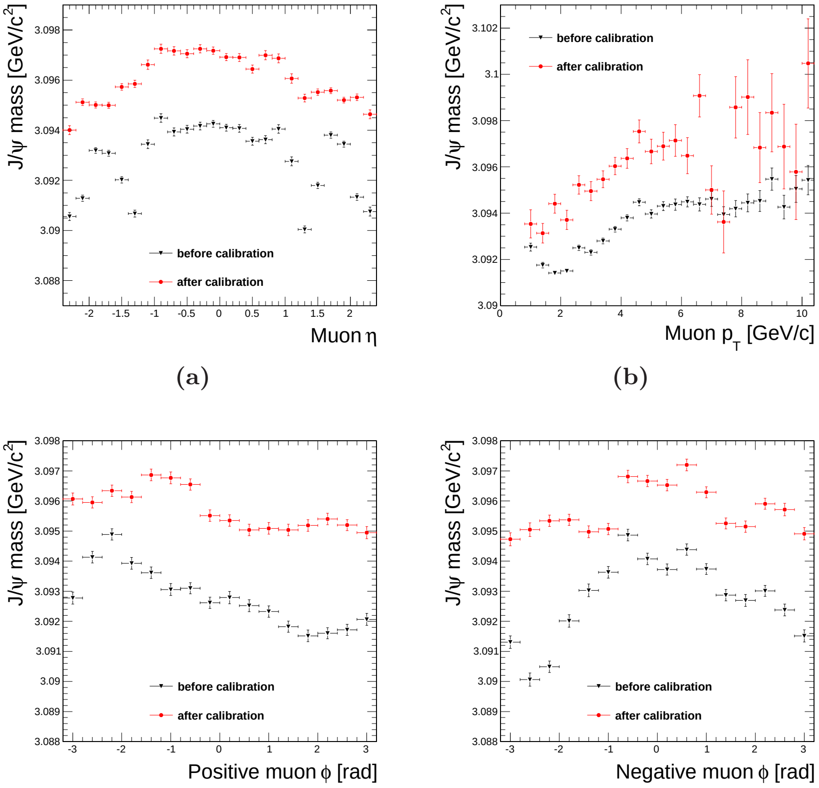

(a) (b)

(c) (d)

Figure 4.16: J/ψ *mass before (black) and after (red) the scale calibration, plotted vs. (a)* η*, (b)* p_{T}*, (b)* ϕ *of positive muon and (c)* ϕ *of negative muon.*

Parameter	Value
A	$(9.4 \pm 0.3) \cdot 10^{-4}$
B	0.49 ± 0.01
$C_{+,u}$	$(-2.2 \pm 0.3) \cdot 10^{-4}$
$D_{+,u}$	0.92 ± 0.14
$C_{+,l}$	$(-5.7 \pm 0.5) \cdot 10^{-4}$
$D_{+,l}$	-0.30 ± 0.07
$C_{-,u}$	$(-2.2 \pm 0.3) \cdot 10^{-4}$
$D_{-,u}$	2.3 ± 0.2
$C_{-,l}$	$(-7.6 \pm 0.4) \cdot 10^{-4}$
$D_{-,l}$	-0.02 ± 0.06

(a)

Parameter	Value
a_0	1.26 ± 0.06
a_1	1.83 ± 0.04
a_2	2.24 ± 0.01
a_3	$(6.73 \pm 0.06) \cdot 10^{-3}$
a_4	$(6.43 \pm 0.05) \cdot 10^{-3}$
a_5	$(8.0 \pm 7.7) \cdot 10^{-3}$
a_6	$(9.2 \pm 3.1) \cdot 10^{-3}$
a_7	0.83 ± 0.14
a_8	$(2.55 \pm 0.03) \cdot 10^{-2}$
a_9	0.19 ± 0.04
a_{10}	2.27 ± 0.01
a_{11}	$(1.2 \pm 0.7) \cdot 10^{-4}$
a_{12}	$(3.1 \pm 6.5) \cdot 10^{-5}$

(b)

Table 4.1: *Results of the transverse momentum (a) scale and (b) resolution fits on about 19 pb^{-1} of integrated luminosity, using Equations 4.9 and 4.8.*

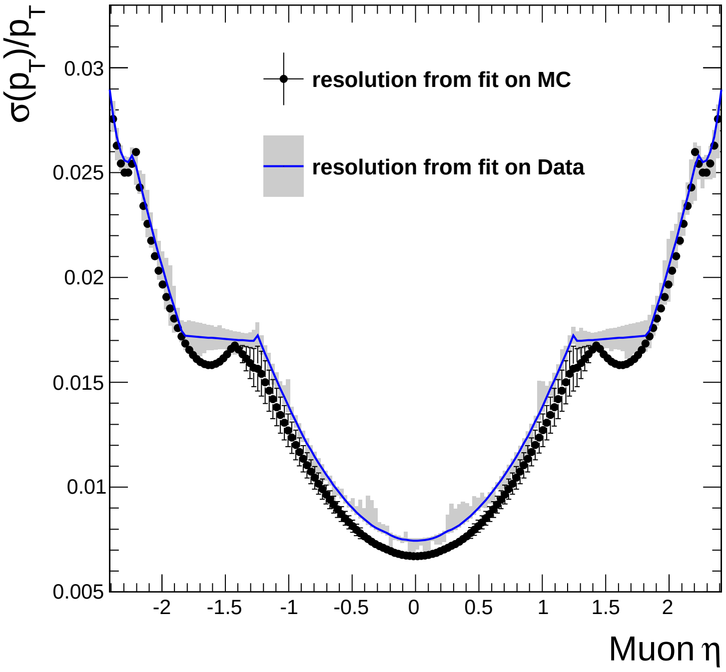

Figure 4.17: *Resolution on muon transverse momentum, measured with about 19 pb*$^{-1}$ *of integrated luminosity (blue line), compared with the results obtained with simulation (black points). In both cases, the resolution is fitted using Equation 4.8. The gray band represents the uncertainty on the function fitted on data, computed from the errors on the parameters summed in quadrature to the systematic error due to the choice of the parametrisation, as explained at the end of Section 4.2.3.*

4.3 Momentum Scale Calibration Using Z

During the first year of data taking, CMS collected about $2 \cdot 10^4$ $Z \to \mu^+\mu^-$ events, selected with the strategy described in Section 4.3.1. These events have been used to investigate possible biases and measure the resolution of muon transverse momenta in a range hardly accessible with muons from J/ψ decays, from about 10 GeV/c up to 80-100 GeV/c. Unlike the J/ψ case, the momentum of muons from Z decays allows a very tight selection, thus the Z signal has a nearly negligible background. On the other hand, the lower statistics gives less sensitivity to the details of the dependance of scale and resolution on muon kinematics. Thus, simpler functions are used to parametrise them.

In Section 4.3.2, the strategy and results of the calibration of inner tracks using $Z \to \mu^+\mu^-$ events from 2010 CMS data are presented for an integrated luminosity of about 30 pb^{-1}. In Section 4.3.3, the same strategy is applied to global tracks and the results are compared to those obtained with inner tracks.

4.3.1 Signal Selection

As a preliminary selection against beam background, the same requirements on primary vertex and quality of tracks described in Section 4.2.1 are applied.

In the transverse momentum range considered in this study, both the tracker muon (Section 3.5) and global muon (Section 3.4) reconstruction algorithms are expected to have maximal efficiency. In order to reduce the contamination from decays-in-flight and punch-through, the muons are required to be identified by both algortihms. Further selection is then applied to tracker and global tracks of both muons:

- number of hits in the silicon detectors > 10;
- number of hits in the pixel detector > 1;
- transverse impact parameter $|d_0| < 2$ mm;
- at least two muon stations included in the global track;
- normalised χ^2 of the global track fit < 10;
- transverse momentum (taken from the tracker fit alone) > 20 GeV/c;
- isolation requirements, as described in [57];
- both muons with $|\eta| < 2.1$;
- dimuon invariant mass between 60 and 120 GeV/c^2.

4.3.2 Calibration of Inner Tracks' Momentum

In Figures 4.18 and 4.19, the mass and resolution of the Z resonance are shown as functions of the muon kinematic variables, in data and simulation, as measured using the inner tracker track of muons. Mass and resolution are estimated, respectively, by the mean value and the Gaussian σ of a Voigtian fit [58] to the resonance peak. The agreement between data and simulation is good, especially in the mass resolution. The Z mass *vs.* η and p_T is well reproduced in Monte Carlo, with opposite trends in η for positive and negative muons. Sinusoidal shapes are visible in $\phi(\mu^+)$ and $\phi(\mu^-)$, but with different phases in data and Monte Carlo.

As already stated, the background level is very low and can be fitted with a single exponential in all the kinematic region. The ansatz functions are determined considering the main features observed in data and simulation (Figures 4.18 and 4.19 and Figures 4.22 and 4.23). The resolution is parametrised as

$$\frac{\sigma(p_T)}{p_T} = \begin{cases} f(p_\mathrm{T}) + a_2\,\eta^2 & \text{for } |\eta| \le a_0 \\ f(p_\mathrm{T}) + a_3\,(|\eta| - a_4)^2 & \text{for } \eta < -a_0 \\ f(p_\mathrm{T}) + a_5\,(|\eta| - a_6)^2 & \text{for } \eta > a_0 \end{cases}, \tag{4.10}$$

where $f(p_\mathrm{T}) = a_1 + 1.8{\cdot}10^{-4}\,p_\mathrm{T}$. The linear p_T dependence is fixed to a value fitted separately on Monte Carlo, to reduce the number of free paramenters in `MuScleFit`. In the external $|\eta|$ regions, two different parabolas are used, to reproduce the asymmetric trends observed both in Monte Carlo and in data. No continuity is required between the central and external parabolas. The $\cot\theta$ and ϕ resolutions are found to be negligible, and are thus fixed to 0 in the fit. In Figures 4.23c and 4.23d, a ϕ-modulation is visible also in p_T resolution, but the size of this modulation is at least one order of magnitude smaller than the effects observed in η and p_T, and is thus neglected.

The momentum scale correction is applied using the following function:

$$p_\mathrm{T}^{corr} = b_0 + b_1\,p_\mathrm{T} + q\,b_2\,\eta + q\,b_3\,\sin(\phi + b_4)\,, \tag{4.11}$$

where q is the muon charge and accounts for the opposite trends of μ^+ and μ^- observed in data and Monte Carlo in the η and ϕ dependences. Note that the sinusoidal functions for opposite charge muons are here used with the same phase and amplitude.

The fit strategy is the same used in the J/ψ case: background, resolution and scale are fitted separately, in this order. In Table 4.2, the results of the resolution and scale fits are reported.

In Figure 4.20, the Z mass *vs.* muon η, p_T and ϕ before and after the calibration are compared. The corrected distributions are, in general, flatter and closer to the expected mass value. As in the case of the J/ψ, it must be noted that the Z mass measured at the LHC is about 0.5 GeV/c^2 lower

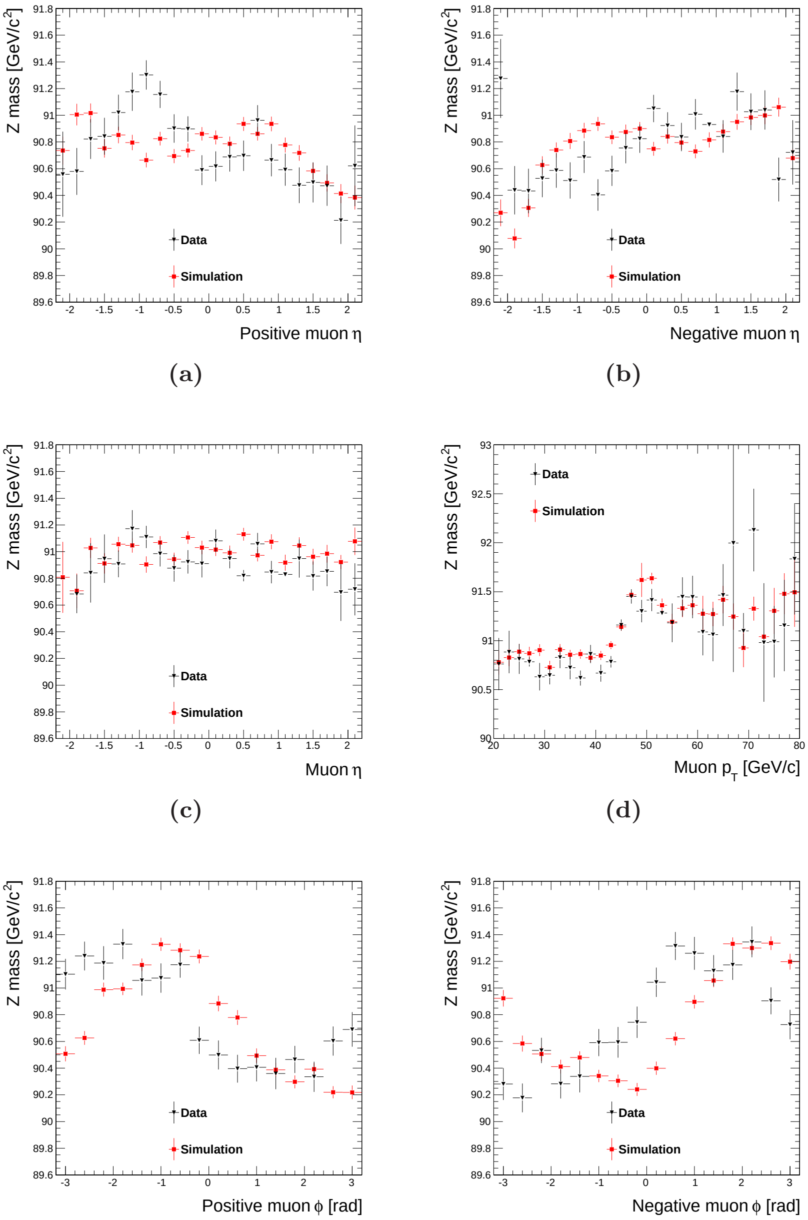

(a) **(b)** **(c)** **(d)** **(e)** **(f)**

Figure 4.18: Z *mass vs. (a)* η *of positive muon, (b)* η *of negative muon, (c)* η*, (d)* p_{T}*, (e)* ϕ *of positive muon and (f)* ϕ *of negative muon, as measured on data (black) and simulation (red), before the scale calibration procedure. Each bin reports the mean value of a fit to the* Z *mass with a Voigtian plus an exponential.*

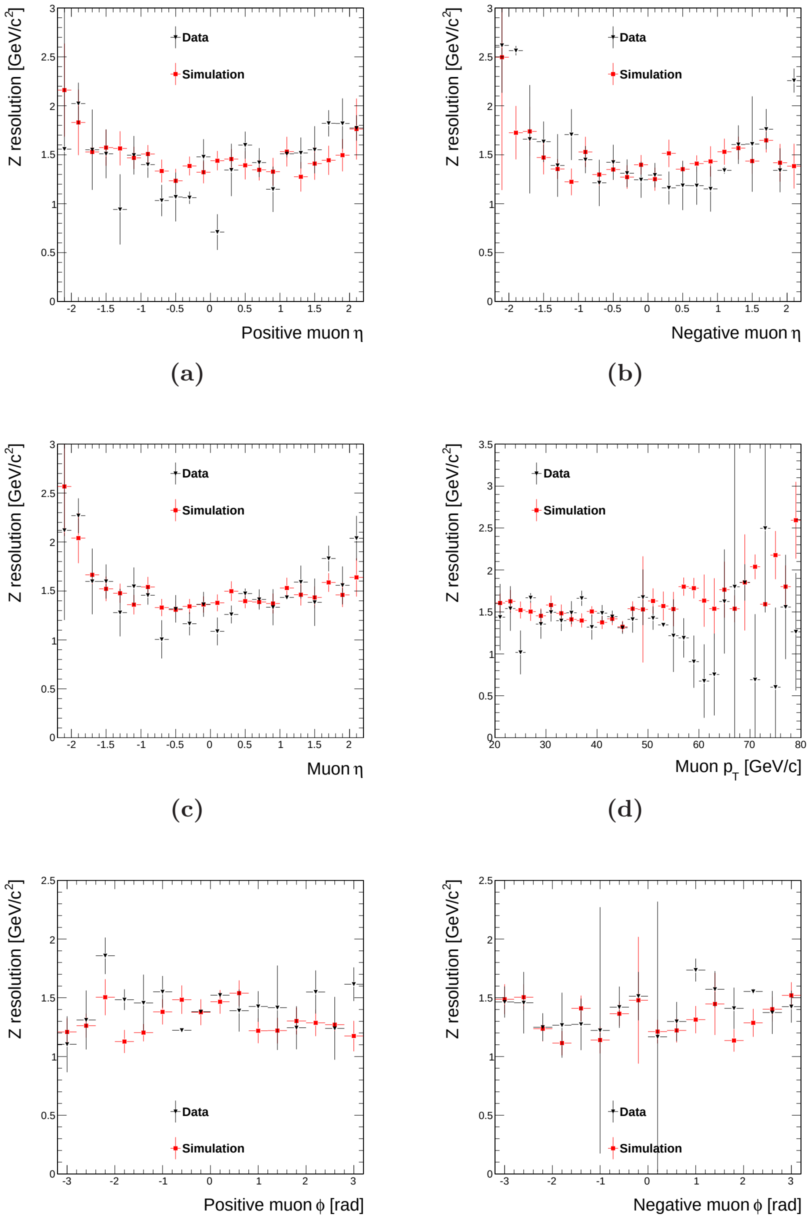

(a) **(b)**

(c) **(d)**

(e) **(f)**

Figure 4.19: *Resolution on the* Z *mass vs. (a)* η *of positive muon, (b)* η *of negative muon, (c)* η*, (d)* p_{T}*, (e)* ϕ *of positive muon and (f)* ϕ *of negative muon, as measured on data (black) and simulation (red), before the scale calibration procedure.*

Parameter	Value
a_0	1.59 ± 0.03
a_1	0.022 ± 0.007
a_2	$(7.6 \pm 0.9) \cdot 10^{-3}$
a_3	$(3.9 \pm 2.9) \cdot 10^{-2}$
a_4	1.39 ± 0.22
a_5	0.09 ± 0.24
a_6	1.72 ± 0.22

(a)

Parameter	Value
b_0	1.0182 ± 0.0011
b_1	$(-4.66 \pm 0.27) \cdot 10^{-4}$
b_2	$(5.23 \pm 0.45) \cdot 10^{-3}$
b_3	$(5.20 \pm 0.39) \cdot 10^{-3}$
b_4	0.37 ± 0.07

(b)

Table 4.2: *Results of the transverse momentum (a) resolution and (b) scale fits, using Equations 4.10 and 4.11.*

than the PDG value, 91.1876 ± 0.0021 GeV/c^2 [21], due to the convolution of the elementary production cross section with the parton distribution functions and to the final state radiation: a mean value of about 90.7 GeV/c^2 is expected. The main biases, i.e. those found in $\phi(\mu^+)$ and $\phi(\mu^+)$, are essentially eliminated. In the η distribution, the mass values are shifted towards the expected value, but the relatively simple function chosen to model the scale correction is not sufficient to correct properly some fluctuations. Also in the p_{T} distribution, the corrected mass is slightly closer to the expected value. The structure observed in p_{T} around 50 GeV/c is still present. Its origin is currently under study, and is probably related to the kinematics of boosted Z bosons. More accurate functions will be developed when more data becomes available.

In Figure 4.21, the Z line-shape, before and after the momentum correction, is fitted with a Voigtian function and an exponential. The mean value, σ and background parameters are reported. The correction shifts the mass peak by almost 100 MeV/c^2 towards the expected value.

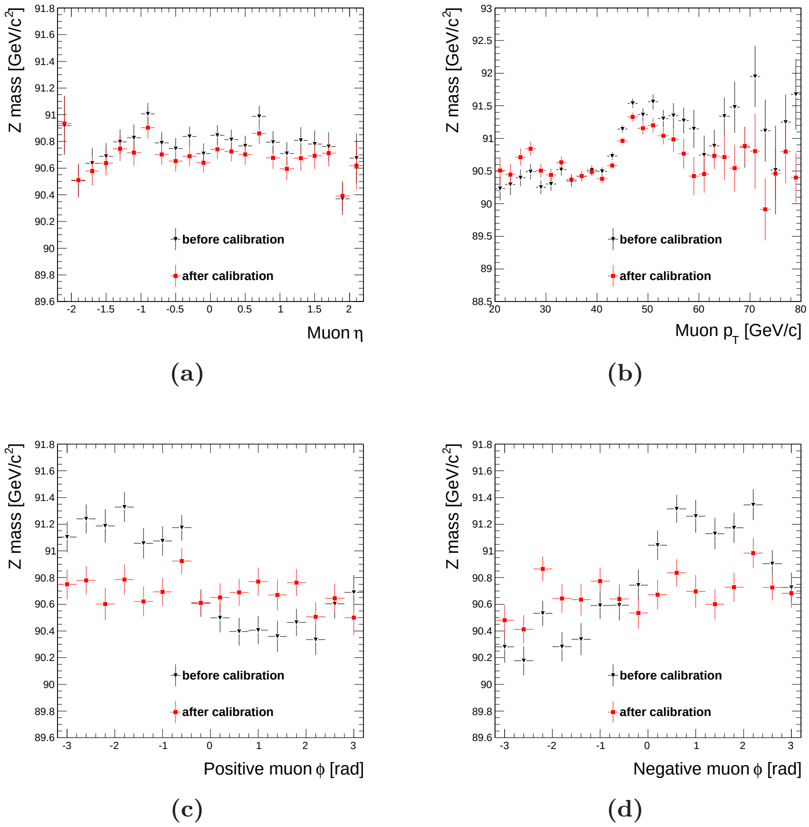

(a) **(b)**

(c) **(d)**

Figure 4.20: Z *mass vs. (a)* η*, (b)* p_{T}*, (b)* ϕ *of positive muon and (c)* ϕ *of negative muon, before (black) and after (red) the scale calibration procedure.*

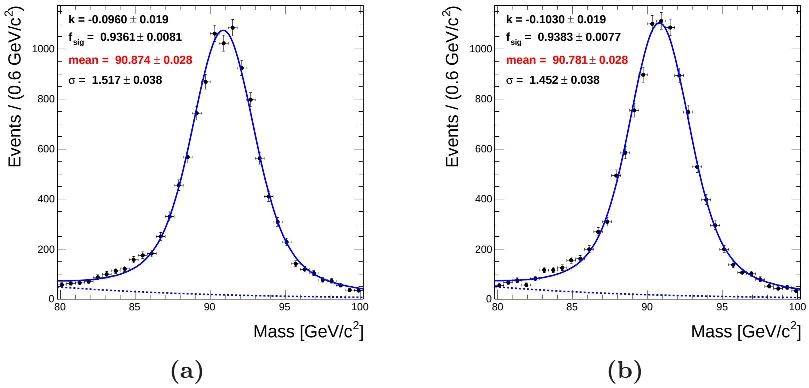

(a) **(b)**

Figure 4.21: Z *mass line-shape, (a) before and (b) after the momentum calibration.*

4.3.3 Calibration of Global Tracks' Momentum

In order to compare the performance of track reconstruction using the inner tracker alone or in combination with the muon spectrometer, the same calibration procedure described in the previous section is here applied to the muon global tracks. In Figures 4.22 and 4.23, the p_{T} relative bias and resolution of inner and global tracks are compared, using a sample of simulated $\mathrm{Z} \to \mu^+\mu^-$ events. As expected from Chapter 3, the results are compatible: the biases are very close and show the same dependences on the muon parameters, and the resolutions coincide within the errors. Thus, the calibration of global tracks is performed using the same parametrisations and strategy adopted with inner tracks: Equations 4.10 and 4.11.

Figures 4.24 and 4.25 show a comparison between the Z mass and mass resolution measured on about 30 pb^{-1} of data using global tracks or using the inner tracker alone, both after the track momentum calibration. Again, the results are completely compatible, confirming the expectations.

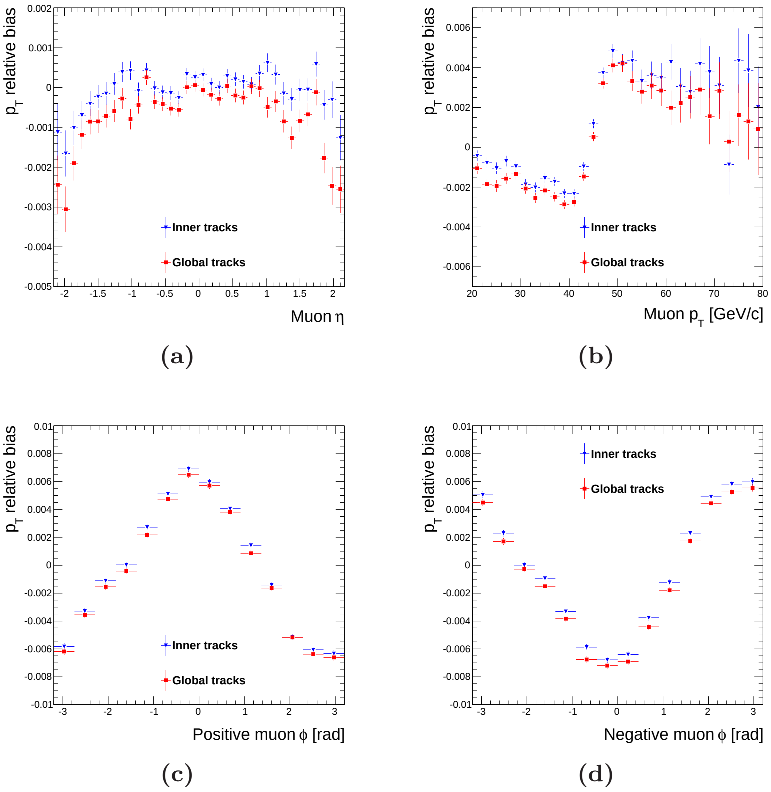

(a) (b)

(c) (d)

Figure 4.22: *Muon p_{T} relative bias as a function of muon (a) η, (b) p_{T}, (c) ϕ of positive muon and (d) ϕ of negative muon, for simulated $\mathrm{Z} \to \mu^+\mu^-$ events, with a realistic start-up scenario.*

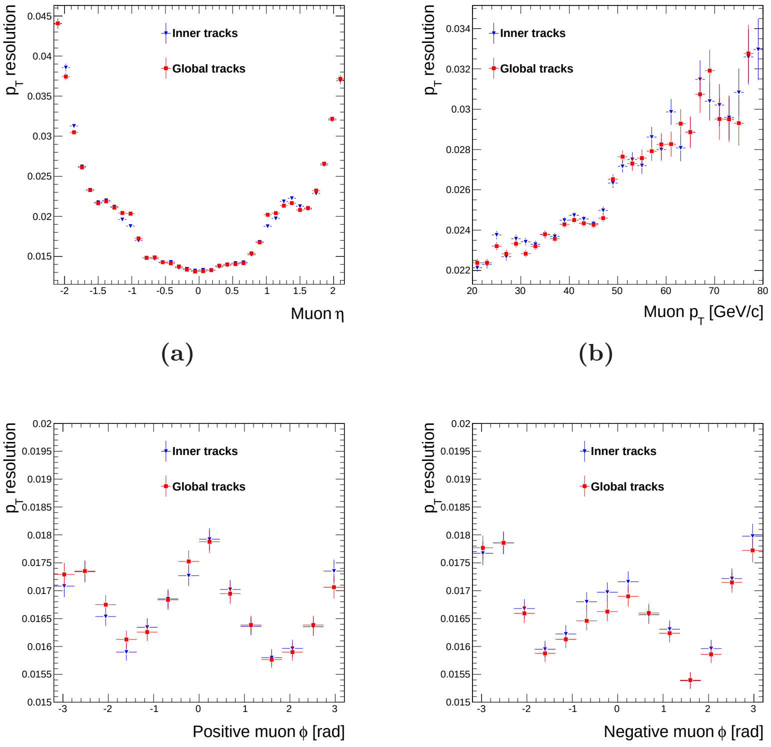

(a) (b)

(c) (d)

Figure 4.23: *Muon p_{T} relative resolution as a function of muon (a) η, (b) p_{T}, (c) ϕ of positive muon and (d) ϕ of negative muon, for simulated $\mathrm{Z} \rightarrow \mu^+\mu^-$ events, with a realistic start-up scenario.*

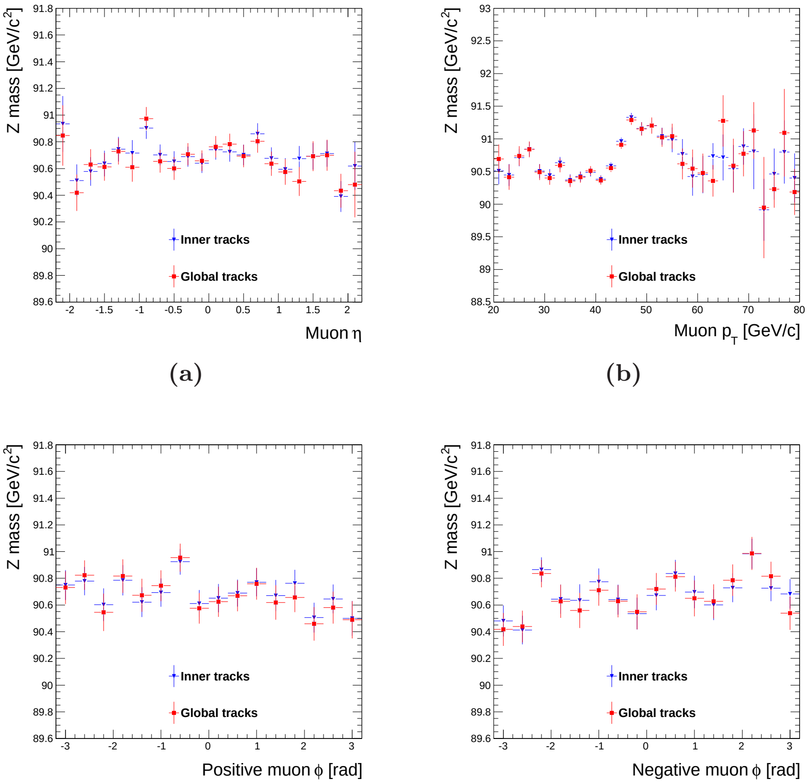

(a) **(b)**

(c) **(d)**

Figure 4.24: Z *mass after the calibration, measured on about 30* pb^{-1} *of data, using inner tracker tracks (blue) and global tracks (red), as a function of (a)* η*, (b)* p_{T}*, (b)* $\phi(\mu^{+})$ *and (c)* $\phi(\mu^{-})$*.*

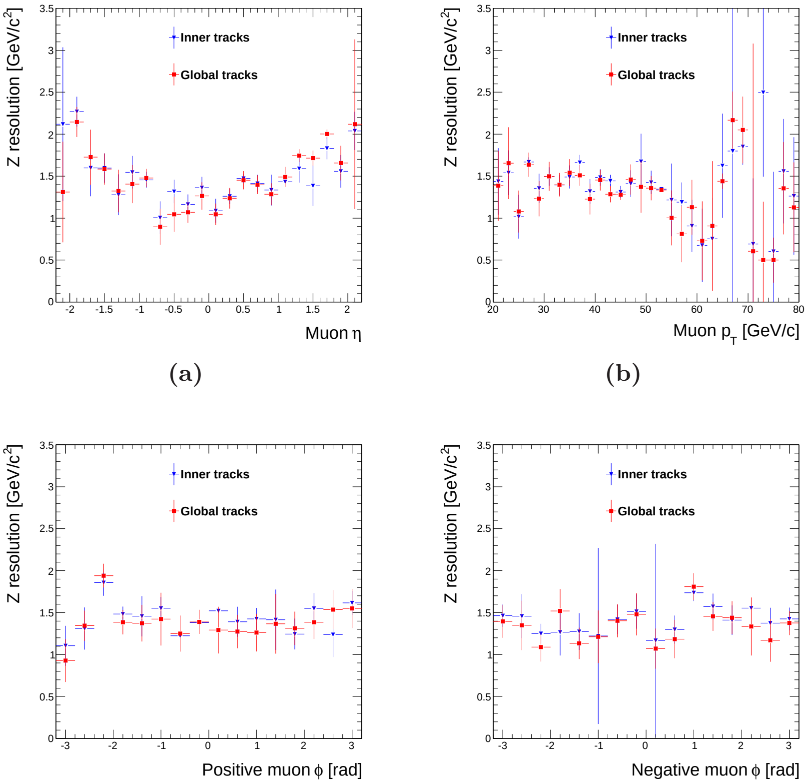

(a) **(b)**

(c) **(d)**

Figure 4.25: Z *mass resolution after the calibration, measured on about 30* pb^{-1} *of data, using inner tracker tracks (blue) and global tracks (red), as a function of (a)* η*, (b)* p_{T}*, (b)* $\phi(\mu^+)$ *and (c)* $\phi(\mu^-)$*.*

Chapter 5

Standard Model Higgs Boson Search in the Four Muon Final State

The SM Higgs boson decay into four muons, $\mathrm{H} \to \mathrm{ZZ} \to 4\mu$, is one of the most promising discovery channels at the LHC over the whole range of possible Higgs masses allowed by the SM (*cf.* Chapter 1).

In this chapter, a prospective analysis of this search is presented for an LHC centre-of-mass energy of 7 TeV and an instantaneous luminosity of $2 \cdot 10^{32}\ \mathrm{cm}^{-2}\,\mathrm{s}^{-1}$. This analysis is part of a CMS search strategy aiming at a combination of the results of the three different leptonic decay channels, $\mathrm{H} \to \mathrm{ZZ} \to \ell^+\ell^-\ell'^+\ell'^-$, with ℓ and ℓ' being muons or electrons, described in [59][60][61] for energies of 14 and 10 TeV. The aim of the present work is to adapt the startegy to the actual operating conditions of the 2010 LHC data taking and to the expected conditions for 2011. The latest developments in lepton reconstruction and identification are adopted, exploiting, in particular, the experience gained from the first year's data.

The selection is here described in detail only for muons. However, a common strategy is used for all final states (as outlined in Section 5.1), based on cuts on the same kinematic variables. In particular, the same Monte Carlo simulation of signal and background samples (Section 5.2) was used for the three channels, and is thus presented here in the context of the complete $\mathrm{H} \to \mathrm{ZZ} \to 4\ell$ analysis. The final results obtained on a total integrated luminosity of 1 fb^{-1} combining the three channels are also presented (Section 5.9).

5.1 Analysis Baseline

The analysis is targeted an integrated luminosity of 1 fb^{-1}, which is expected to be delivered by the end of 2011 at a centre-of-mass energy of 7 TeV.

With this luminosity, the expected number of Higgs events is very low for any possible mass. Thus, it is essential to keep the signal efficiency as high as possible.

The use of a common cut-based analysis for the three final states allows a cross-check of the results. After the trigger selection (Section 5.4), a first skimming procedure (Section 5.5.1), common to the three final states, brings the data volume to a more manageable level. Further preliminary selections (Section 5.5.2) are applied separately to the three channels: these are aimed at reducing the abundant QCD background and consist of loose cuts on the lepton transverse momenta and on the two-lepton and four-lepton invariant masses.

The final selection (Section 5.6) is based on the same variables for the three different channels, in order to keep the selection as homogeneous as possible, although the specific characteristics of electrons and muons and the different background levels contributing to each final state have to be taken into account.

In Section 5.7, the results of the selection applied to the 2010 CMS data, for an integrated luminosity of about 32 pb^{-1}, are compared with the expectations from Monte Carlo simulations. Particular emphasis is put on the development of techniques for the control of background rates from data and for a data-driven derivation of experimental and background systematic uncertainties (Section 5.8).

Finally, the expected sensitivity of CMS for the observation of a SM-like Higgs boson is discussed in a mass range from 115 to 250 GeV/c^2 (Section 5.9).

5.2 Monte Carlo Simulation of the Relevant Physics Processes

Datasets of signal and background events with the 4ℓ final state were produced with a detailed Monte Carlo simulation of the detector response, and with the complete CMS reconstruction chain, including the imperfect calibration and alignment expected at the beginning of data taking.

Different Monte Carlo generators were used for signal and background production, in particular PYTHIA [38], ALPGEN [42], MADGRAPH [62] and POWHEG [63]. For all processes, the showering and hadronisation phases were performed by PYTHIA.

In all distributions presented in the following and for the final results, the number of events of each sample is rescaled according to the highest-order cross section computation available for that process: in general, the backgrounds are known at NLO level, and the signal at NNLO [18][19]. Thus, in all figures in this chapter, unless differently specified, each distribution is

Process		Generator (order)	$\sigma_{\mathrm{HO}} \cdot BR$ (HO)
	(130 GeV/c^2)		6.87 fb (NNLO)
$\mathrm{H} \to 4\ell$	(150 GeV/c^2)	POWHEG (NLO)	10.41 fb (NNLO)
	(200 GeV/c^2)		15.93 fb (NNLO)
$t\bar{t} \to 2\ell 2\nu b\bar{b}$		POWHEG (NLO)	16.71 pb (NLO)
$\mathrm{Z}b\bar{b} \to 2\ell b\bar{b}$		ALPGEN (LO)	2.93 pb (NLO)
$\mathrm{ZZ}^{(*)} \to 4\ell$		MADGRAPH (LO)	4.80 pb (NLO)

Table 5.1: *Description of the simulated datasets for signal and main backgrounds. Here ℓ stands for e, μ or τ.*

scaled with the following factor:

$$w_{HO} = \frac{L \cdot \sigma_{\mathrm{HO}}}{N_{\mathrm{gen}}}\,, \tag{5.1}$$

where σ_{HO} is the highest-order available cross section, N_{gen} is the number of generated Monte Carlo events and L is the integrated luminosity considered in this prospective analysis, i.e. 1 fb^{-1}. In the comparisons between data and simulations, the simulated distributions are normalised to the integrated luminosity considered in data, i.e. about 32 pb^{-1}.

Table 5.1 summarises the generators used and the cross sections at the highest known order for the Higgs signal and for the three main backgrounds: $t\bar{t}$ + n-jets, $\mathrm{Z}b\bar{b}$ + n-jets, $\mathrm{ZZ}^{(*)}$ + n-jets. Additionally, other backgrounds are taken into account: n-jets (hereafter referred to as "QCD"), Z/W$^{\pm}$ + n-jets, $\mathrm{Z}c\bar{c}$ + n-jets. "Jets" are here understood as gluon- or light quark-induced jets (u, d, s), and their number n is up to four. For the event generation, the parton density function set CTEQ6L1 is used, with the QCD scale set at PYTHIA's default values. The masses of the b and t quarks are set to 4.75 and 172.5 GeV/c^2, respectively. Finally, ℓ is understood as being any charged lepton, e, μ or τ, and Z stands for Z, Z* or γ^*.

5.2.1 Signal $\mathrm{H} \to \mathrm{ZZ}^{(*)} \to 4\ell$

The Higgs boson events were generated at NLO with POWHEG through the main production channel, gg → H. H is forced to decay into two Z bosons, which are allowed to be off-shell, and both Z bosons are forced to decay into lepton pairs. Thus, the cross section quoted in Table 5.1 is

$$\sigma_{\mathrm{NNLO}}(\mathrm{pp} \to \mathrm{H}) \cdot BR(\mathrm{H} \to \mathrm{ZZ}^{(*)}) \cdot BR(\mathrm{Z} \to 2\ell)^2.$$

In the 4μ and $4e$ channels, the cross sections are enhanced due to the interference of amplitudes with permutations of identical leptons in the final state. Since POWHEG does not account for such enhancement, a correction factor is evaluated with CompHEP [64] and considered in the 4μ and $4e$ analyses. This factor is significant only for Higgs masses below 200 GeV/c^2. Figure 5.1 shows the $\mathrm{H} \to 4\ell$ cross section and the $4\mu/4e$ enhancement factor as a function of the Higgs boson mass.

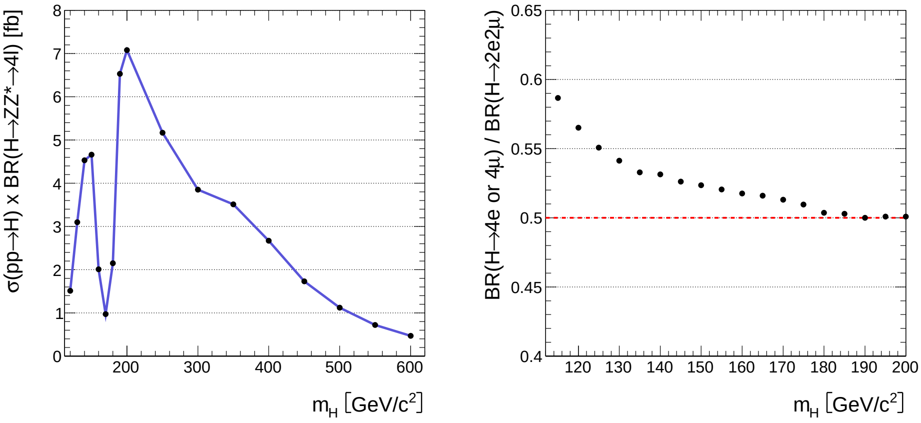

(a) **(b)**

Figure 5.1: *(a) NNLO cross section for* $\mathrm{H} \to \mathrm{ZZ}^{(*)} \to 4\ell$ *as a function of the Higgs boson mass* ($\ell = e,\ \mu$ *here). (b) Enhancement factor of the* 4μ *and* $4e$ *branching ratios with respect to the* $2\mu 2e$ *one (without this factor, the ratio would be 0.5).*

5.2.2 Background $t\bar{t}$

A fully inclusive sample of $t\bar{t}$ + n-jets (n = 0, 1, 2, 3) was generated with powheg. Events were preselected with the following requirements: at least four leptons (e or μ) with $p_{\mathrm{T}} > 4$ GeV/c and $|\eta| < 2.7$.

5.2.3 Background Z$b\bar{b}$

The process $\mathrm{gg}/q\bar{q} \to \mathrm{Z}b\bar{b} \to 2\ell b\bar{b}$ was generated at LO with alpgen and filtered with the same requirements used for $t\bar{t}$. The NLO cross section was calculated using mcfm [65].

5.2.4 Background ZZ

The $q\bar{q} \to \mathrm{ZZ}^{(*)} \to 4\ell$ sample was generated with MadGraph in the t and s channels, then filtered with the same requirements described above. To account for contributions from all the NLO diagrams, events are reweighted in the analysis with a mass-dependent factor, $K_{\mathrm{NLO}}(m_{4\ell})$, computed with mcfm and shown in Figure 5.2. The average correction, also shown in the figure, is 1.345. The contribution from gluon fusion process $\mathrm{gg} \to \mathrm{ZZ}^{(*)}$

is also included, weighting about 20% with respect to $q\bar{q} \rightarrow \mathrm{ZZ}^{(*)}$ at large Higgs masses.

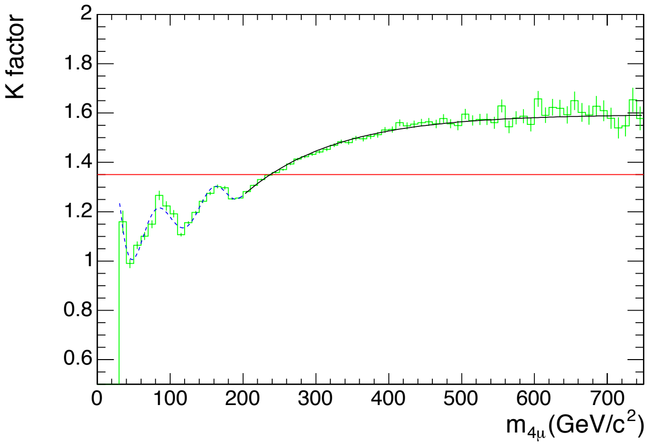

Figure 5.2: *Mass-dependent NLO k-factor for the* $\mathrm{ZZ}^{(*)} \rightarrow 4\ell$ *process, evaluated with* MCFM.

5.3 Definition of Muon Variables

Before proceeding to the description of the selection strategy, it is useful to define some variables that will be used at different stages of the analysis. The variables are here defined for muons, but equivalent definitions are valid also for electrons.

5.3.1 Muon Isolation Variables

To define the *isolation* of a muon, a cone in the η-ϕ space is built around its track, with radius $\Delta R_{\mathrm{iso}} = \sqrt{\Delta\eta^2 + \Delta\phi^2}$. Another narrower "veto" cone is defined around the muon, with $\Delta R_{\ \mathrm{veto}} < \Delta R_{\ \mathrm{iso}}$. All the tracks or energy deposits falling inside the isolation cone, but outside the veto cone are considered in the calculation of the isolation observable. Minimal cuts on the p_{T} and quality of the tracks are applied. If two or more muons fall in the same isolation cone, the contribution of the extra muon(s) is subtracted. Optimal values for the two cones were found to be $\Delta R_{\ \mathrm{iso}} = 0.3$ and $\Delta R_{\ \mathrm{veto}} = 0.015$.

The *track-based* isolation variable are defined as

$$\mu\mathrm{Iso}_{\mathrm{trk}} = \frac{\sum_i p_{\mathrm{T},\,i}}{p_{\mathrm{T},\,\mu}}\,, \tag{5.2}$$

where $\Delta R_{\,\mathrm{veto}} < \Delta R_{\,i} < \Delta R_{\,\mathrm{iso}}$. Similar definitions apply to the *calorimeter-based* isolation variables, replacing the p_T of tracks with the energy of calorimeter deposits in the cone around the muon track: $\mu\mathrm{Iso}_\mathrm{ECAL}$ and $\mu\mathrm{Iso}_\mathrm{HCAL}$. A combined isolation variable can be defined as

$$\begin{aligned} \mu\mathrm{Iso} &= \alpha \cdot \mu\mathrm{Iso}_\mathrm{trk} + \beta \cdot \mu\mathrm{Iso}_\mathrm{ECAL} + \gamma \cdot \mu\mathrm{Iso}_\mathrm{HCAL} \\ &= \frac{\sum_i \big(\alpha \cdot p_{\mathrm{T},i} + \beta \cdot E_{\mathrm{ECAL},i} + \gamma \cdot E_{\mathrm{HCAL},i}\big)}{p_{\mathrm{T},\mu}} \,, \end{aligned} \tag{5.3}$$

where the coefficients α, β and γ can be optimised to obtain the best performance. Note that μIso depends on the muon p_T through the denominator. An independent variable can be defined removing the division by p_T:

$$\mu\mathrm{Iso}_\mathrm{ind} = \sum_i \left(\alpha \cdot p_{\mathrm{T},i} + \beta \cdot E_{\mathrm{ECAL},i} + \gamma \cdot E_{\mathrm{HCAL},i}\right) . \tag{5.4}$$

5.3.2 Muon Track Impact Parameter

The *impact parameter* (IP) of a track provides a measurement of its three-dimensional distance from the primary vertex of the collision. The *transverse* and *longitudinal* impact parameters (TIP, LIP) are defined on the transverse plane x-y and on the longitudinal axis z, respectively.

The IP *significance* ($\mathrm{S_{IP}}$) is defined as the ratio between the IP and its error

$$\mathrm{S_{IP}} = \frac{\mathrm{IP}}{\sigma_\mathrm{IP}} \,, \tag{5.5}$$

thus it takes into account the finite resolution of the position measurement. Similar definitions hold for the significances of the TIP and LIP.

The CMS pixel detector provides an excellent resolution both in the transverse plane and in the longitudinal direction, so a selection based on the three-dimensional $\mathrm{S_{IP}}$ can be expected to give performances comparable to separate cuts on $\mathrm{S_{TIP}}$ and $\mathrm{S_{LIP}}$.

Note that, in general, the IP and its significance can be positive or negative. For the purpose of this analysis, however, the sign is irrelevant, thus all the IP-related variables used hereafter are understood as absolute values.

5.3.3 Dimuon and Four-Muon Invariant Mass

Throughout the analysis, the invariant mass of muon pairs (i.e. the mass of Z candidates) and the invariant mass of the four muons (i.e. the mass of the Higgs candidate) are exploited. Even when only four muons are present in the event, an ambiguity arises in the definition of the muon pairs to form the Z candidates. If more than four muons are detected, the number of possible $\mu^+\mu^-$ combinations increases, and also the Higgs candidate can

Trigger Object	L1 thres. [GeV/c^2]	HLT thres. [GeV/c^2]
Single μ	7	15
Double μ	0-0	3-3

Table 5.2: *p_T thresholds for muon L1 and HLT paths used in this analysis. No isolation is required. For more details on these path, see Table 3.1*

be reconstructed in several ways. To solve these ambiguities, a univocal definition is needed for the two Z candidates.

The two muon pairs are reconstructed in the following way:

- the first Z candidate (expected to be on mass shell) is chosen as the muon pair with opposite charge and with the closest invariant mass to the nominal Z boson mass;
- the second Z candidate ("$Z^{(*)}$") is formed by choosing, among the remaining muons, the two with highest p_T and opposite charge.

When more than four muons are found, the Higgs boson candidate is built from the two $\mu^+\mu^-$ pairs selected as above.

In the context of the $H \to 4\ell$ analysis, the aforementioned definitions apply also to the $4e$ channel. For the $2\mu 2e$ final state, the leptons in a pair are also required to match in flavour. This also reduces the level of ambiguity.

5.4 Trigger Selection

In the decay of the Higgs boson, for any allowed mass, at least one of the intermediate Z bosons is likely to be produced on the mass shell and decay into a pair of muons with p_T around $m_Z/2$. Thus, the triggering strategy relies on the presence of one or two high-p_T muons. The LHC luminosity foreseen for the first years of data taking, $2 \cdot 10^{32}$ cm^{-2} s^{-1}, allows for unprescaled muon HLT paths with p_T thresholds as low as 15 GeV/c. A very high trigger efficiency is therefore expected for the Higgs signal. For the 4μ channel, in order to maximise the trigger efficiency, the logical `OR` among single and double muon HLT paths is chosen. Similar paths, including also some requirements on the isolation of muons, will be exploited at higher luminosities (e.g., see [60] and [61]). For this analysis, instead, it was chosen not to use the "isolated" trigger paths, since they are not fully commissioned yet. A list of the used HLT paths is provided in Table 5.2.

In this work, in order to compare the results from simulated and real data, the HLT paths considered in data taking are emulated in simulation by applying the same cuts on top of the skimming step (Section 5.5.1).

5.5 Preliminary Selections

The events passing the combination of triggers described in Section 5.4 undergo a preliminary selection, aimed at rejecting the majority of "unuseful" events that will not pass the entire selection, while preserving the signal efficiency and the phase space for the measurement of backgrounds and for systematics studies. This preliminary selection consists of two steps, called *skimming* (described in Section 5.5.1) and *preselection* (Section 5.5.2).

5.5.1 Event Skimming

The aim of this first selection is to reduce the data volume after the HLT to a manageable level. The skimming is designed to keep the signal efficiency close to 100% and significantly suppress QCD, W + jets and Z + jets backgrounds.

The same skimming strategy is applied in the three analyses:

- at least two leptons (e or μ) with $p_{\mathrm{T}} > 10$ GeV/c;
- one additional lepton with $p_{\mathrm{T}} > 5$ GeV/c.

These cuts leave the number of signal events almost unchanged, while the total number of events is reduced by a factor 50 with respect to the HLT output. It was also checked that none of the signal events rejected by the skimming would have passed the full selection.

5.5.2 Event Preselection

The main goal of this step is to reject fake leptons, mostly coming from multi-jet events, so to bring the contributions from QCD di-jet and W/Z + jets to a level comparable to or below the three main backgrounds. The rejection of fake leptons also serves to reduce the combinatorial ambiguities due to the presence of more than four leptons in the event.

For the 4μ final state, the preselection consists of the following cuts:

- at least two $\mu^+\mu^-$ pairs with invariant mass $m(\mu^+\mu^-) > 12$ GeV/c^2; the muons are required to be "global muons" (see Chapter 3) with $p_{\mathrm{T}} > 5$ GeV/c for $|\eta| < 1.2$ (barrel), or $p_{\mathrm{T}} > 5$ GeV/c and $p > 9$ GeV/c for $|\eta|$ between 1.2 and 2.4 (endcaps);
- at least one combination of two matching pairs with an invariant mass $m(4\mu) > 100$ GeV/c^2;
- at least four muons with loose isolation requirements: μIso < 1, according to the definition given in Equation 5.3 (with $\alpha = \beta = \gamma = 1$).

The requirement of two muon pairs with the right combination of charge and flavour is motivated by the main characteristics of the signal event topology, and the cut on the invariant mass of the four muons eliminates events that are incompatible with the SM Higgs mass constraints. The cut on the invariant mass of muon pairs protects against the contamination from low mass hadronic resonances. Finally, the loose isolation requirements further suppress the QCD background and reject fake muons and punch-through.

The reduction of the background rate at each preselection step is shown in Figure 5.3a for the 4μ case. The dominating QCD and W + jets backgrounds are completely suppressed after the requirement of four loose-isolated muons, and the contribution of the Z + jets process is brought down to a level comparable with that of the $t\bar{t}$, $Zb\bar{b}$ and ZZ final states.

The four-muon invariant mass reconstructed after the preselection is shown in Figure 5.3b. The spikes visible in the Z + jets distribution are due to the limited number of events available in simulation, compared to the large cross sections of these process: the weights used to normalise the distributions (Equation 5.1) are therefore very large. This is confirmed by the statistical error bars in Figure 5.3a.

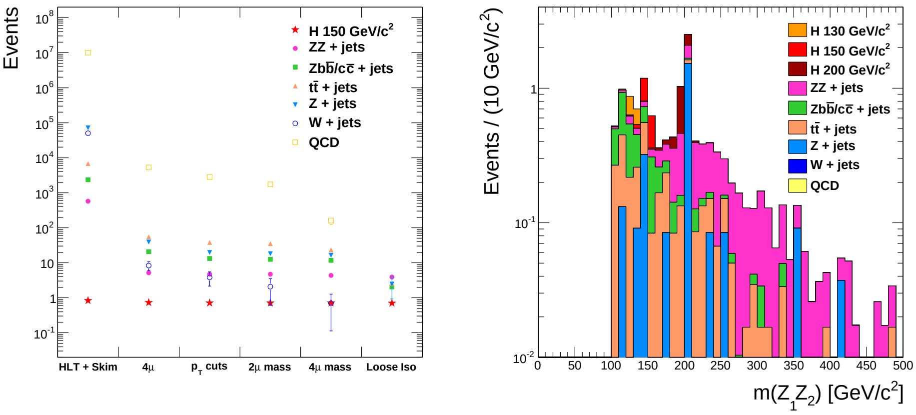

(a) (b)

Figure 5.3: *(a) Number of signal and background events per fb^{-1} in the 4μ channel. QCD, W/Z + jets, $t\bar{t}$, $Zb\bar{b}$ and ZZ backgrounds are shown, along with the $H \rightarrow ZZ \rightarrow 4\mu$ signal at m_H = 150 GeV/c^2. (b) Four-muon invariant mass spectrum after the preselection (the distributions are stacked). Higgs bosons with masses 130, 150, and 200 GeV/c^2 are considered.*

5.6 Signal Selection

After the preselection, the event sample is dominated by $t\bar{t}$, $\mathrm{Z}b\bar{b}/\mathrm{Z}c\bar{c}$ and Z + jets. The following steps of the analysis will be focused on the rejection of these backgrounds. In all these processes, two muons originate from inside the jets, and are therefore surrounded by hadrons. In the two main backgrounds, $t\bar{t} \rightarrow 2\mathrm{W}b\bar{b}$ and $\mathrm{Z}b\bar{b}$, the muons produced inside the b-jets are likely to have large impact parameters with respect to the primary vertex, due to the long lifetime and large mass of b-hadrons. Thus, the isolation and IP variables defined in Section 5.3 can strongly reduce these backgrounds. Moreover, constraints on the invariant mass of muon pairs can provide further rejection power. The discriminating strategies exploiting these variables are described in Sections 5.6.1 to 5.6.3, and their combination for a cut-based event selection is discussed in Section 5.9. The selection is described for the 4μ channel only.

5.6.1 Muon Isolation

The isolation variables have been introduced in Section 5.3.1. Several observables are available: track-based or calorimeter-based variables, or their combinations with different weights. Among them, the best discriminating power between signal and background is shown by $\mu\mathrm{Iso}$ (Equation 5.3) [61], here used with the three coefficients, α, β and γ, set to 1, i.e. counting with the same weight the contributions from the three sub-detectors, tracker, ECAL and HCAL. However, different definitions were used to test the stability of the isolation cut, and it was verified that the efficiencies do not strongly depend on the variable definitions. $\mu\mathrm{Iso}$ showed better discriminating power than $\mu\mathrm{Iso}_{\mathrm{indep}}$ (Equation 5.4).

The selection of an event is based on the isolation of the two least isolated muons, which are likely to come from jets in background events. Rather than using the isolation of the two muons separately, their sum is found to be more effective: $\mu\mathrm{Iso}2_{\,\mathrm{least}} = \mu\mathrm{Iso}_{4\mathrm{th}} + \mu\mathrm{Iso}_{3\mathrm{rd}}$. The distribution of $\mu\mathrm{Iso}2_{\,\mathrm{least}}$ is shown in Figure 5.4a for the signal and main backgrounds. In Figure 5.4b, the signal efficiency is shown as a function of the $t\bar{t}$ and $\mathrm{Z}b\bar{b}$ efficiencies for different cuts on $\mu\mathrm{Iso}2_{\,\mathrm{least}}$. Efficiencies are computed with respect to preselected events. For a cut $\mu\mathrm{Iso}2_{\,\mathrm{least}} < 0.4$, the signal efficiency is about 90% for a Higgs boson mass of 150 GeV/c^2, with background efficiencies around 5% for $t\bar{t}$ and below 10% for $\mathrm{Z}b\bar{b}$.

Isolation *vs.* Muon p_{T}

As shown above, $\mu\mathrm{Iso}2_{\,\mathrm{least}}$ is more effective on $t\bar{t}$ than on $\mathrm{Z}b\bar{b}$. This is due to the different characteristics of the b-jets in the two processes: in $t\bar{t}$, jets are initiated by heavily boosted b quarks, coming from the decay of

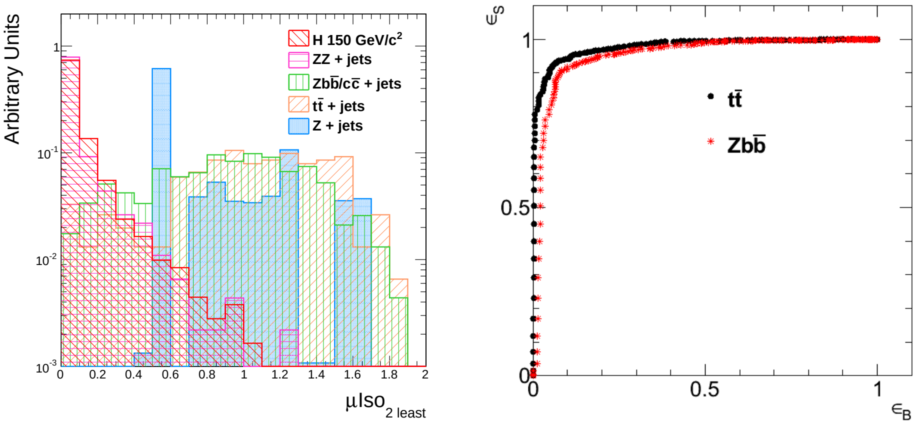

(a) (b)

Figure 5.4: *(a) Combined isolation variable $\mu\mathrm{Iso}_{2\,\mathrm{least}}$ distribution for signal and main backgrounds in the 4μ channel. All the distributions are normalised to unity. (b) Discriminating power of the cut on $\mu\mathrm{Iso}_{2\,\mathrm{least}}$ against $t\bar{t}$ and $\mathrm{Z}b\bar{b}$ backgrounds, in the 4μ channel.*

W bosons; in $\mathrm{Z}b\bar{b}$, b-jets are generally less collimated in the detector and lead to muons with a softer p_{T} spectrum. In order to preserve the signal efficiency while suppressing low p_{T} muons in $\mathrm{Z}b\bar{b}$ events, the isolation criteria for such muons can be made p_{T} dependent. In Figure 5.5, the bidimensional distributions $\mu\mathrm{Iso}_{2\,\mathrm{least}}$ *vs.* muon p_{T} are shown for a Higgs signal with mass 150 GeV/c^2 and for the $\mathrm{Z}b\bar{b}$ background. Here $\mu\mathrm{Iso}_{2\,\mathrm{least}}$ is redefined using the $\mu\mathrm{Iso}_{\mathrm{indep}}$ variable (Equation 5.4) of the two least isolated muons. In such a way, $\mu\mathrm{Iso}_{2\,\mathrm{least}}$ does not depend on the p_{T} of muons and no correlations are introduced between the two variables. On the abscissa, the p_{T} of the third ($p_{\mathrm{T},3}$, Figure 5.5a) or fourth ($p_{\mathrm{T},4}$, Figure 5.5b) highest-p_{T} muon can be used. Signal and background are well separated, so that the plane can be divided into two regions, respectively dominated by the signal or the $\mathrm{Z}b\bar{b}$ background. This conclusion has also important consequences for the control of background systematics (see Section 5.8). This separation can be expected, given that the muons from b-jets, other than non-isolated, are usually characterised by a lower p_{T} than those coming from the decay of heavy bosons.

The signal and background regions are best separated by a slanting line of the form

$$\mu\mathrm{Iso}_{2\,\mathrm{least}} \;=\; A \cdot p_{\mathrm{T},3/4} \;-\; B\,.$$

The discriminating lines shown in Figure 5.5 are optimised for a Higgs boson mass $m_{\mathrm{H}} = 150$ GeV/c^2 and used for all the mass values in this analysis.

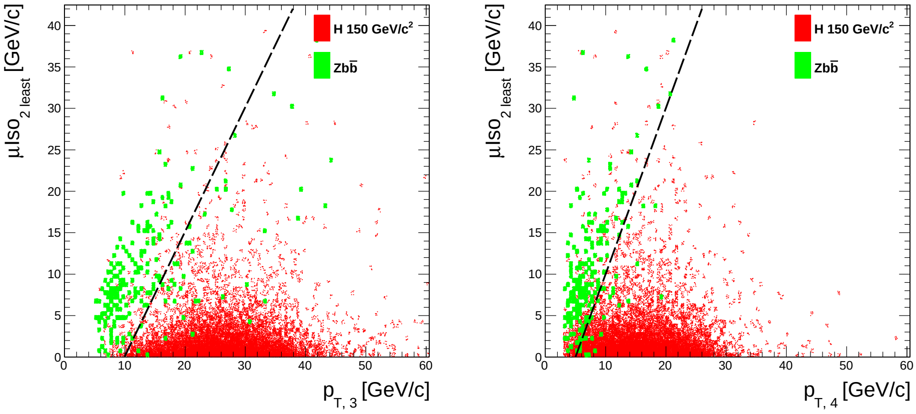

(a) **(b)**

Figure 5.5: *Combined isolation variable* $\mu\mathrm{Iso}_{2\,\mathrm{least}}$ *vs.* p_{T} *of the (a) third and (b) fourth highest* p_{T} *muon, for a Higgs boson mass of 150 GeV/*c^2 *and for the* $\mathrm{Z}b\bar{b}/\mathrm{Z}c\bar{c}$ *backgrounds in the* 4μ *final state.*

5.6.2 Impact Parameter

In signal events, muons are expected to come from the primary vertex of the interaction, so the IP of their tracks is statistically compatible with zero. In $t\bar{t}$ and $\mathrm{Z}b\bar{b}$ events, instead, two muons originate from the displaced decay vertex of the b-hadron, so a larger IP with respect to the primary vertex is expected. Such information can be exploited to discriminate $t\bar{t}$ and $\mathrm{Z}b\bar{b}$ backgrounds from signal.

As explained in Section 5.3.2, several IP-related variables are available. The three-dimensional IP was found to have the same discriminating power as the combination of two separate variables on the transverse plane (TIP) and longitudinal direction (LIP). More precisely, the significance of the three-dimensional IP, S_{IP}, is used, in order to account for the finite resolution of the detector. The four muons, selected as in Section 5.5.2, are sorted by increasing S_{IP}. In background events, the third and fourth muons (i.e. the two with the highest S_{IP}) are likely to come from b-jets, and are thus considered for the selection. In Figures 5.6a and 5.6b, the S_{IP} distributions of the third and fourth muon are presented for a Higgs signal with $m_{\mathrm{H}} = 150\ \mathrm{GeV}/c^2$ and for the main backgrounds. As expected, $t\bar{t}$ and $\mathrm{Z}b\bar{b}$ have distributions extending to much larger values than the Higgs, while the *irreducible* ZZ background is essentially indistinguishable from the signal. The discriminating power of the S_{IP} variable of the third muon against $t\bar{t}$ and $\mathrm{Z}b\bar{b}$, after the preselection, is illustrated in Figure 5.6c.

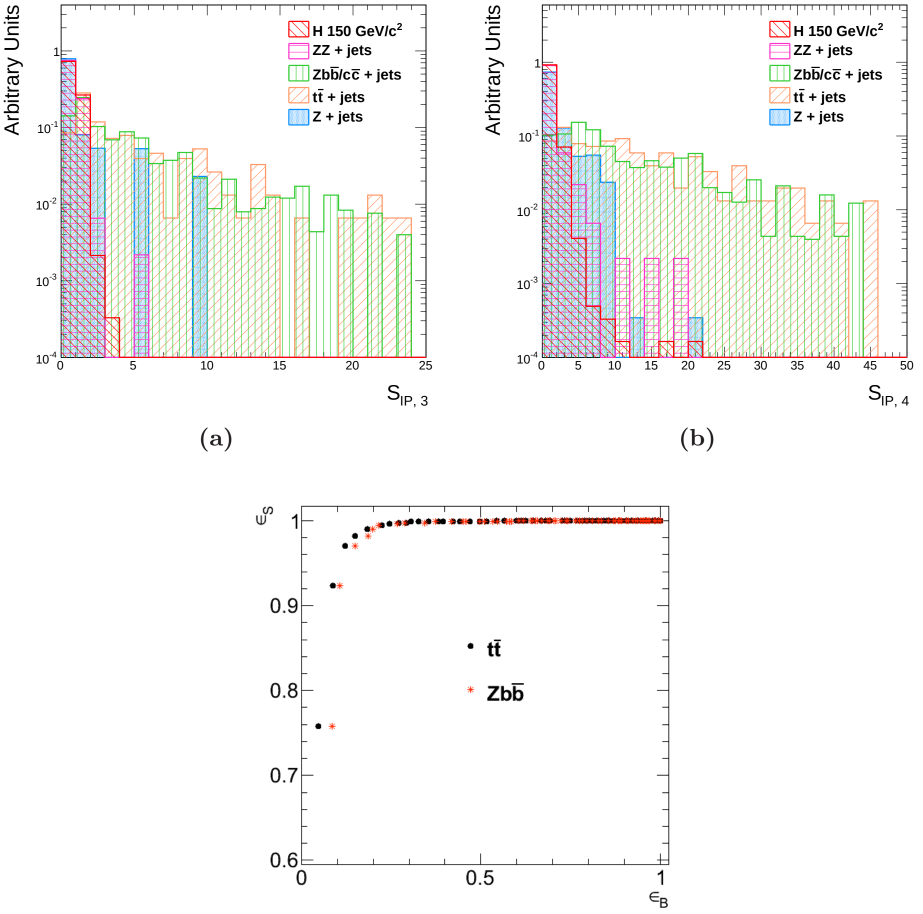

(a) (b)

(c)

Figure 5.6: *Distributions of the muon impact parameter significance* $\mathrm{S_{IP}}$ *for the (a) third and (b) fourth muon, sorted by increasing* $\mathrm{S_{IP}}$*, for signal and for* $t\bar{t}$ *and* $\mathrm{Z}b\bar{b}/\mathrm{Z}c\bar{c}$ *backgrounds. All the distributions are normalised to unitary area. (c) Discriminating power of the* $\mathrm{S_{IP}}$ *of the third muon.*

5.6.3 Kinematics

The presence of two Z bosons in the intermediate state of the Higgs decay chain, one of which is likely to be on mass shell, provides further rejection power against all the main backgrounds.

The muons forming the candidate $\mathrm{Z}^{(*)}$ (according to the definition given in Section 5.3.3) have a harder p_T spectrum in the signal than in the $t\bar{t}$ and $\mathrm{Z}b\bar{b}$ backgrounds. The invariant mass of the first muon pair (the on-shell candidate Z) well separates the signal from the non-resonant $t\bar{t}$ background. The mass of the second muon pair (the candidate Z^*) can be exploited to reject both $t\bar{t}$ and $Zb\bar{b}$. Moreover, the mass spectra of both muon pairs distinguish the Higgs signal from the irreducible ZZ background, which receives contributions also from γ^*. The invariant mass distributions of both muon pairs for the signal and the main backgrounds are shown in Figure 5.7, after the preselection step.

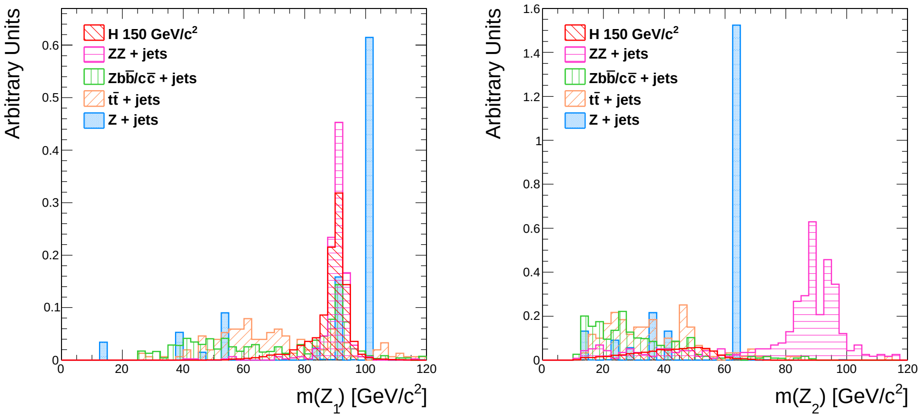

(a) **(b)**

Figure 5.7: *Invariant mass distributions of the Z (left) and $Z^{(*)}$ (right) candidates, according to the definitions given in Section 5.3.3, for a Higgs signal with m_H = 150 GeV/c^2 and the main backgrounds. All the distributions are normalised to unity. The spikes in the Z + jets distribution are due to the limited number of events in the simulated sample, as explained in Section 5.5.2 and shown by the error bars in Figure 5.3a.*

5.6.4 Event Selection

The observables described in the previous sections are used for a cut-based mass-independent selection. This allows for a simple, reliable and robust search procedure for the start-up luminosities and conditions. An additional sliding window cut in the measured 4μ invariant mass spectrum is used to derive the sensitivity for a Higgs boson of given mass m_H. The selection cuts are optimised to provide the best significance for the observation of a Higgs boson with a mass around 150 GeV/c^2.

Cuts are applied to muon isolation, impact parameter and the bidimensional distribution of isolation *vs.* muon p_T. As for the dimuon invariant mass, only loose cuts are applied, in order to minimise the dependence on m_H and thus obtain a simple selection, quasi-optimal for any m_H hypothesis. The set of selection cuts is reported in Table 5.3 and the number of signal and background events after each cut is shown in Figure 5.8a for an integrated luminosity of 1 fb^{-1}.

Variable	Threshold
Isolation	$\mu\mathrm{Iso}_{2\,\mathrm{least}} < 0.4$ $\mu\mathrm{Iso}_{2\,\mathrm{least}} < 1.5 \cdot p_{\mathrm{T},3} - 15$ $\mu\mathrm{Iso}_{2\,\mathrm{least}} < 2.0 \cdot p_{\mathrm{T},4} - 10$
IP significance	$\mathrm{S}_{\mathrm{IP}}(4^{th}\,\mu) < 5$ $\mathrm{S}_{\mathrm{IP}}(3^{th}\,\mu) < 4$
m_{Z}	50–100 GeV$/c^2$
m_{Z}^*	20–100 GeV$/c^2$

Table 5.3: *Set of selection cuts.*

The reconstructed 4μ invariant mass spectrum after the whole selection is shown in Figure 5.8b. The $\mathrm{Z}b\bar{b}$ background is completely suppressed and $t\bar{t}$ is considerably reduced, with an event rate well below the $\mathrm{ZZ}^{(*)}$ continuum. SM Higgs boson signals expected for an experiment at 1 fb^{-1} of integrated luminosity, for masses 130, 150 and 200 GeV$/c^2$, are superimposed for illustration. The signals are observed as narrow peaks. The average number of events expected from Higgs signals is comparable to or larger than that expected from the background in a narrow mass window centered on the signal. Thus, after the m_{H} independent baseline selection, a signal with mass m_{H} = 130-200 GeV$/c^2$ would emerge above the background.

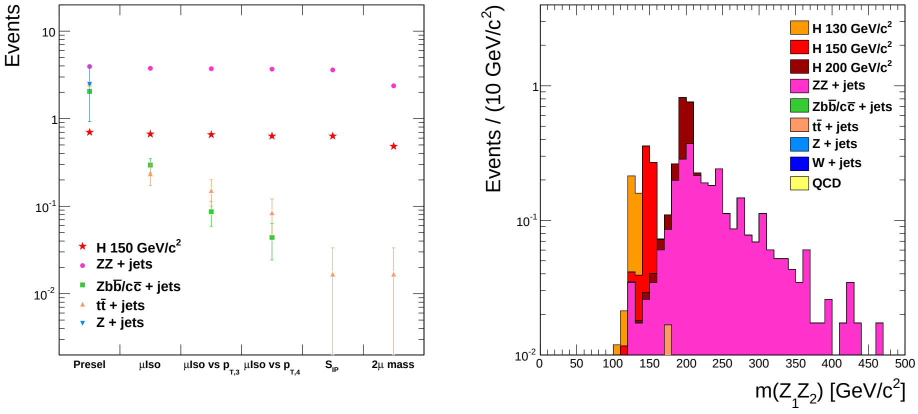

(a)

(b)

Figure 5.8: *(a) Number of signal and background events per* fb^{-1} *in the* 4μ *final state after each selection cut.* $t\bar{t}$, $\mathrm{Z}b\bar{b}/\mathrm{Z}c\bar{c}$ *and* ZZ *backgrounds are shown, along with* $\mathrm{H} \to \mathrm{ZZ} \to 4\mu$ *signal at* m_{H} = *150 GeV*$/c^2$*. (b) Four-muon invariant mass spectrum after the complete selection (the distributions are stacked). A Higgs boson with mass 150 GeV*$/c^2$ *is considered.*

5.7 Results on the Data Collected in 2010

The selection criteria described in the previous sections are applied to the LHC collision data collected by CMS in 2010, for an integrated luminosity of about 32 pb^{-1}. The results are compared with the expectations from simulation shown above. Figures 5.9 and 5.10 show the distribution of the main variables used for the selection, after the HLT and skimming steps and the requirement of four reconstructed muons. The data are in good agreement with the expectations from simulation.

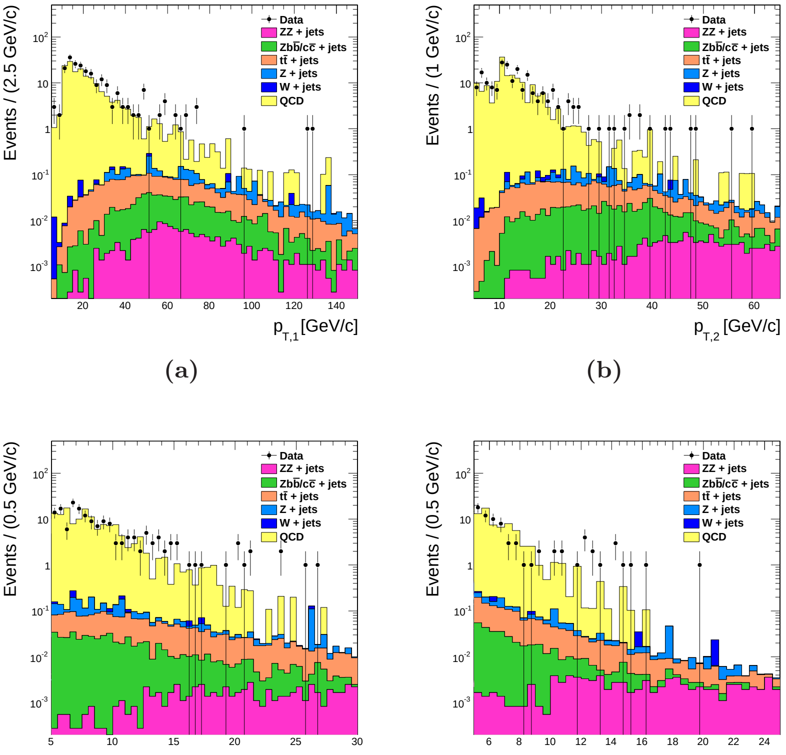

(a) (b)

(c) (d)

Figure 5.9: *Transverse momentum of the four muons of each event, sorted from the highest p_T (a) to the lowest p_T (d), for events after HLT, skimming and the requirement of four reconstructed muons, in data and simulation, for an integrated luminosity of 32 pb^{-1}. The Monte Carlo distributions include only the backgrounds and are stacked.*

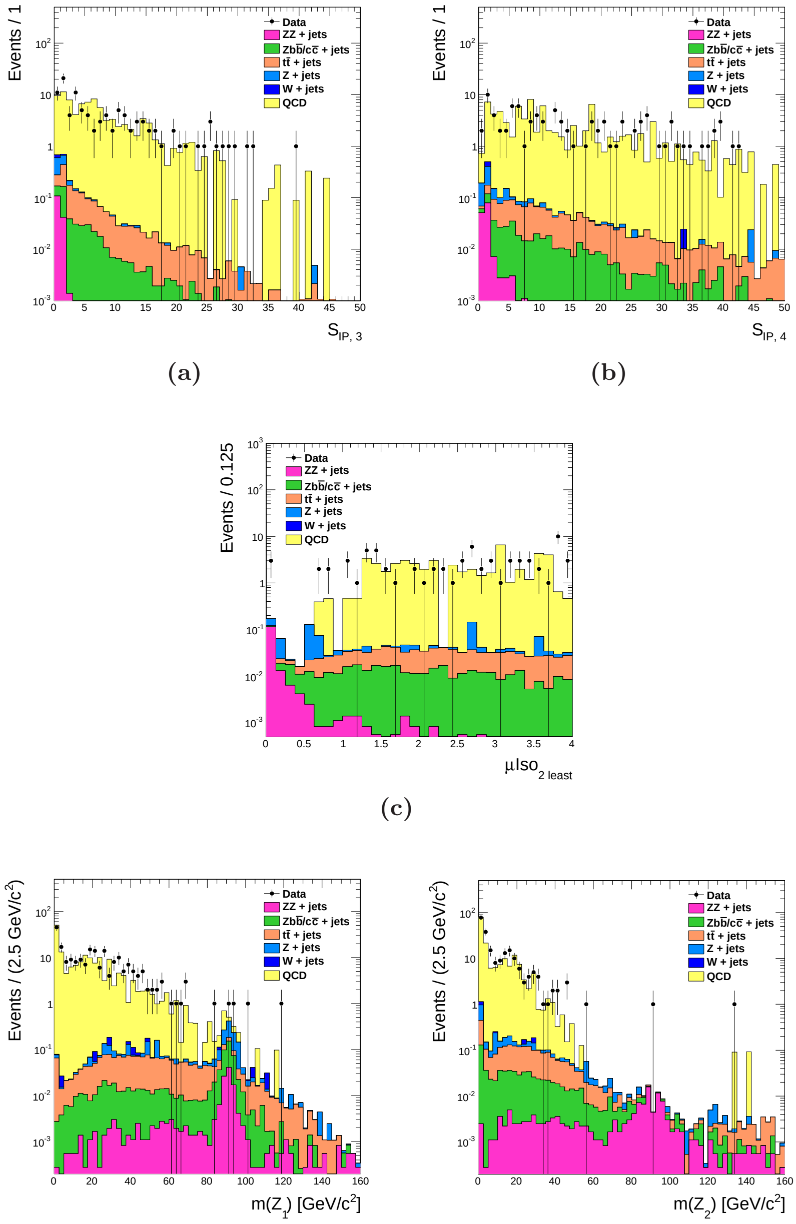

(a) **(b)**

(c)

(d) **(e)**

Figure 5.10: *Distributions of the (a) highest* $\mathrm{S_{IP}}$ *and (b) second highest* $\mathrm{S_{IP}}$ *of each event. (c) Distribution of the isolation variable* $\mu\mathrm{Iso}_{2\,\mathrm{least}}$*. Invariant mass of the (d)* Z *and (e)* $\mathrm{Z}^{(*)}$ *candidates, according to the definitions given in Section 5.3.3. Events after HLT, skimming and the requirement of four reconstructed muons are considered, in data and simulation, for an integrated luminosity of 32* pb^{-1}*. The Monte Carlo distributions include only the backgrounds and are stacked.*

In Figure 5.11a, the 4μ invariant mass distribution is shown after the HLT and skimming steps and the requirement of four reconstructed muons. At this stage, the event sample is still dominated by the QCD background, and the agreement with the Monte Carlo expectation is fairly good.

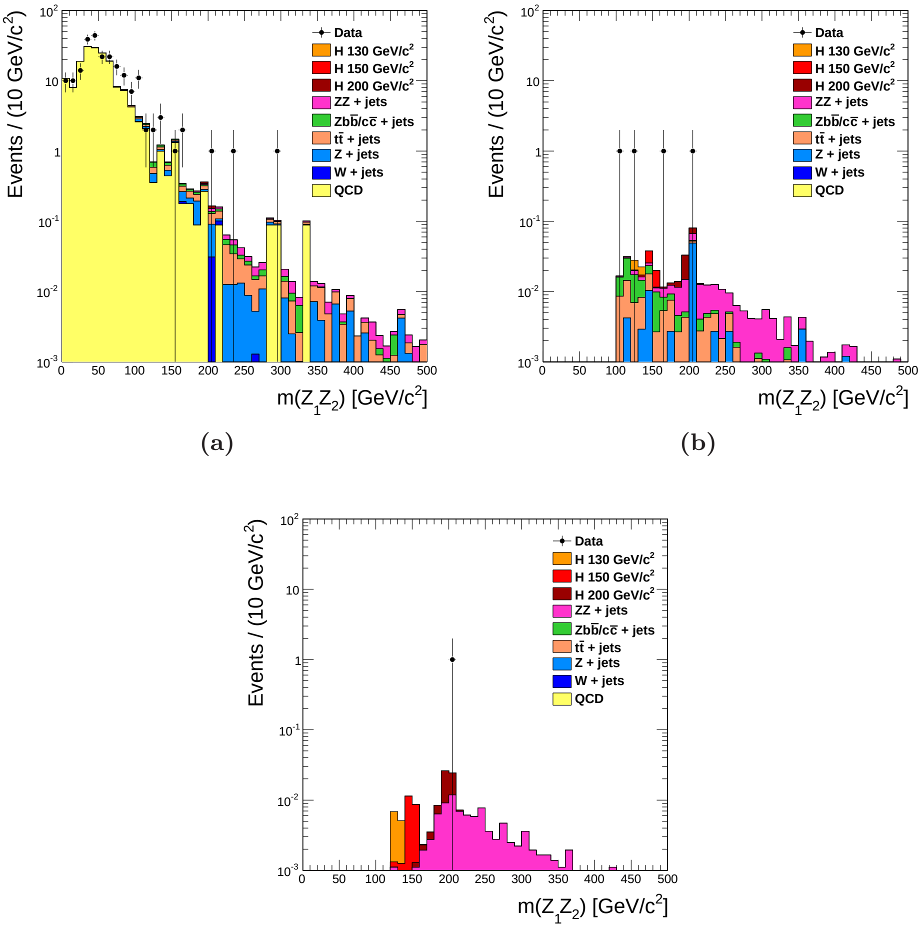

(a) **(b)**

(c)

Figure 5.11: *Four-muon invariant mass spectrum (a) after the skimming and the requirement of four reconstructed muons, (b) after the preselection, and (c) after the whole selection, for an integrated luminosity of 32 pb^{-1}. Higgs bosons with masses 130, 150 and 200 GeV/c^2 are also shown for reference. The black points are the CMS data. The Monte Carlo distributions are stacked.*

In Figure 5.11b, the same comparison is made after the preselection. Four events are left, which is much more than expected from simulation. In Table 5.4, a description of these four events is provided. All the events contain at least one Z boson candidate. Event 1, in particular, seems a plausible $Z\gamma^*$ event, considering the invariant mass of the second muon pair

	m(4ℓ) [GeV/c^2]	m(2ℓ) [GeV/c^2]	p_{T} (μ) [GeV/c]	μIso	$\mathrm{S_{IP}}$
1	110.0	90.04	35.32	0	0.422
			37.13	0.03	0.460
		0.35	5.17	0	0.832
			9.55	0	1.811
2	125.5	92.08	9.17	0	1.187
			20.25	0.69	7.407
		29.06	5.11	0.13	0.771
			7.81	0	0.360
3	167.8	101.13	63.67	0.02	0.507
			48.78	0	0.240
		39.90	26.66	0.008	0.426
			14.13	0	0.496
4	201.7	92.12	19.56	0	0.537
			25.88	0	1.029
		92.23	48.14	0	0.994
			43.44	0	0.411

Table 5.4: *Description of the four events surviving the preselection.*

and the isolation of the corresponding muons. It should be noted that events of such kind are not included in the simulated samples used in this analysis: although the $\mathrm{ZZ}^{(*)}$ Monte Carlo sample described in Section 5.2.4 does include the contribution from Z^* and γ^*, a mass cut is applied at generator level, such that $m(\gamma^*/\mathrm{Z}^*) > 20$ GeV/c^2. This partly accounts for the observed discrepancy. Event 2 satisfies a specific selection for $\mathrm{Z}b\bar{b}$ and $t\bar{t}$ events (see Section 5.8.1 and Figure 5.14b) and has a good Z candidate, so it is a plausible $\mathrm{Z}b\bar{b}$ event. Though there is no sufficient information to confirm the presence of two b-jets. Event 3 is consistent with ZZ^* and event 4 has two clean Z candidates, both on mass shell.

In Table 5.5, the number of events in 32 pb^{-1} of data is reported after each step of the selection, and compared to the number of signal and background events expected from simulation. Only one of the four preselected events survives the whole selection, i.e. event 4. Event 1 is rejected by the requirement on the invariant mass of the $\mathrm{Z}^{(*)}$ candidate and the bidimensional $\mu\mathrm{Iso}_{2\,\mathrm{least}}$ *vs.* p_{T} cuts. Event 2 fails the isolation, isolation *vs.* p_{T} and $\mathrm{S_{IP}}$ cuts. Event 3 does not satisfy the requirements on the invariant mass of the on-shell Z candidate.

The four-muon invariant mass of event 4 is around 202 GeV/c^2 and lies roughly on the top of the mass spectrum expected from Monte Carlo simulations (*cf.* Figure 5.11c). The Poissonian probability of observing one $\mathrm{ZZ} \to 4\mu$ event in 32 pb^{-1} of data, after the selection chain described above, is about 8%. Considering a four lepton final state, since no events are se-

Process	Presel.	Iso	Iso *vs.* p_T	IP sign.	$Z^{(*)}$ mass
H 130 GeV/c^2	0.0137	0.0126	0.0114	0.0113	0.0095
H 150 GeV/c^2	0.0232	0.0211	0.0201	0.0200	0.0186
H 200 GeV/c^2	0.0420	0.0359	0.0353	0.0349	0.0335
ZZ	0.1218	0.1039	0.1023	0.1007	0.0863
$Zb\bar{b}/Zc\bar{c}$	0.2790	0.0223	0.0024	0	0
$t\bar{t}$	0.1134	0.0059	0.0027	0.0005	0.0005
Z + jets	0.0793	$1.2 \cdot 10^{-6}$	$8.9 \cdot 10^{-7}$	0	0
Total MC	0.5935	0.1321	0.1074	0.1012	0.0868
Data	4	3	2	2	1

Table 5.5: *Number of events after each selection step, in data and in simulation, for an integrated luminosity of 32 pb^{-1}. The total number of simulated events includes only backgrounds.*

lected in the $4e$ and $2\mu 2e$ channels, the probability of a single observation rises to about 23%. At the same luminosity, the probability for the observation of a Higgs boson with mass around 200 GeV/c^2 and decaying into four muons is instead about 3.2%, and 9.9% considering all three final states. A display of event 4 is shown in Figure 5.12.

5.8 Control of Background and Systematic Uncertainties

In the first phase of LHC data taking, when a very low statistics is available and the discovery of a SM-like Higgs boson in the four-lepton final state is inaccessible, particular emphasis is placed on the understanding of the systematic uncertainties, on the measurement of the efficiency of the algorithms used in the analysis, and on the precise estimate of the background rates.

5.8.1 Control of Background from Data

After the cut-based selection described in Section 5.6.4, only a handful of events are left in both signal and background. It is therefore crucial to estimate correctly the amount of background remaining in the signal phase space. A typical procedure consists in choosing a *control region* outside the signal phase space, measuring the number of background events therein, and extrapolating it to the signal region, using the ratio between the number of background events in the signal region and in the control region derived from the Monte Carlo simulation.

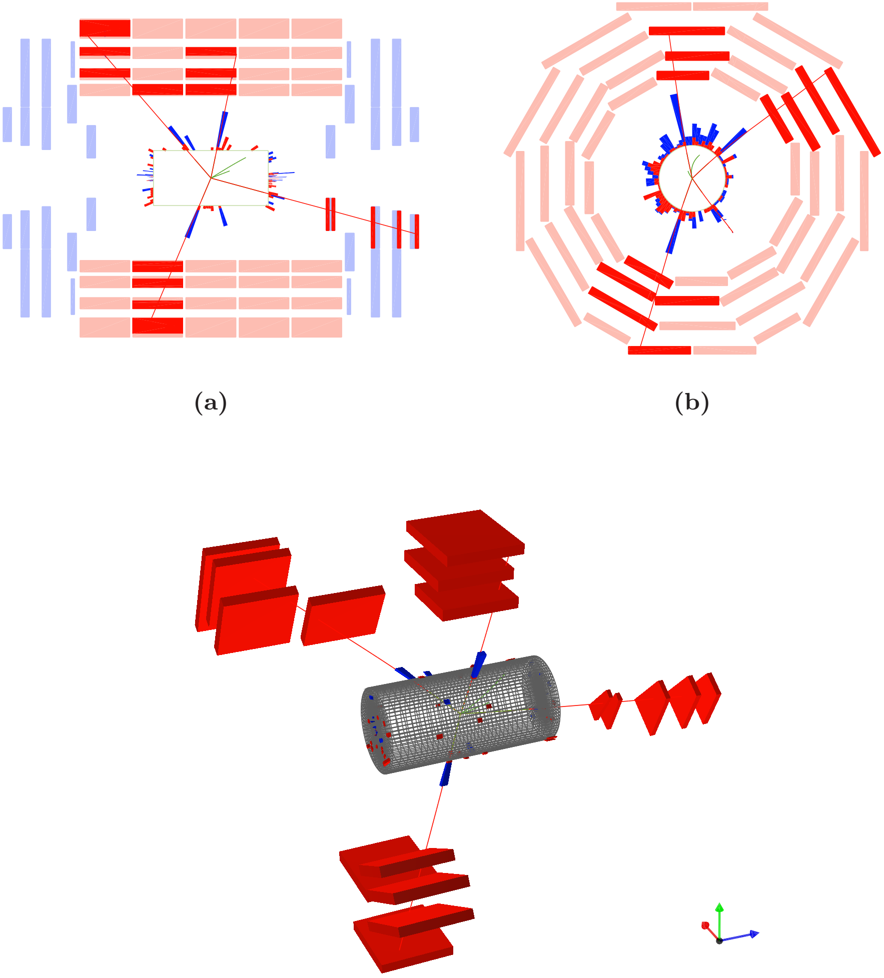

(a) (b)

(c)

Figure 5.12: *Display of the 4μ event passing the whole* H → 4μ *selection (event 4 in Table 5.4): (a) r-z view, (b) r-φ view, (c) 3D view.*

Measurement of the ZZ Background Contribution from Data

Indirect Measurement Two data-driven methods are used to evaluate the level of the ZZ background in a given Higgs mass window, defined as

$$m_{\mathrm{H}} - 2\sigma_m < m(4\ell) < m_{\mathrm{H}} + 2\sigma_m \ ,$$

where σ_m is the width of the Higgs boson resonance with mass m_{H}. One method consists in using the *sidebands* in the $m(4\ell)$ spectrum outside the signal window as control region. The second method relies on the measurement of the number of $\mathrm{Z} \to 2\ell$ events in the signal region. In this case, the control region coincides with the signal region, but using a different reference process.

In both cases, the ZZ background rate $N_{\mathrm{ZZ}}(\Delta m)$ in any given signal mass window Δm can be predicted from the observed event count in the control region N_{CR}:

$$N_{\mathrm{ZZ}}^{pred}(\Delta m) \;=\; \rho(m_{\mathrm{H}}) \cdot N_{CR}^{meas} \;.$$

The factor $\rho(m_{\mathrm{H}})$ is derived from Monte Carlo:

$$\rho(m_{\mathrm{H}}) \;=\; \frac{N_{\mathrm{ZZ}}^{theo}(\Delta m) \cdot \varepsilon_{\mathrm{ZZ}}}{N_{CR}^{theo} \cdot \varepsilon_{CR}} \;,$$

where the ε's are the reconstruction and selection efficiencies.

Both methods are described in detail elsewhere [66]. The uncertainties for such predictions have two distinct components: systematic errors associated with the factor $\rho(m_{\mathrm{H}})$ and statistical errors associated with N_{CR}^{meas}.

The theoretical systematic uncertainties on $\rho(m_{\mathrm{H}})$ (PDFs and QCD scales [66]), known at the NLO level, are of the order of 2-4% in both methods. Systematic uncertainties on reconstruction and isolation efficiencies cancel out nearly completely in the side-bands method, and only partly in the other method, where two muons are reconstructed. Muon reconstruction and isolation cut efficiencies can be measured with a 1% uncertainty. For both methods, the uncertainty on luminosity cancels out completely.

The largest difference comes from the statistical uncertainty on the measurement of N_{CR}^{meas}: the rate of ZZ → 4μ events produced at the LHC is about 10^{-5} times that of Z → $\mu^+\mu^-$, which means that the statistical error on N_{CR} obtained with the side-bands method is at least two orders of magnitude larger than that obtained with the normalisation to single Z events.

Direct Measurement The analysis flow described in the previous sections for the Higgs boson search will be also used to measure the ZZ → 4μ cross section with the first data [67].

For this purpose, both Z candidates are required to be on mass shell, with an invariant mass between 65 and 115 GeV/c^2. These cuts alone, applied on top of the preselection, leave the background at a few percent level. After the whole selection described in Table 5.3, about 3 ZZ → 4μ events are expected with an integrated luminosity of 1 fb^{-1} at 7 TeV, while the $t\bar{t}$ and Z + jets backgrounds are completely suppressed and the expectation value for Z$b\bar{b}$ is 0.003 events. In Figure 5.13a, the 4μ invariant mass spectrum after this selection is shown for an integrated luminosity of 1 fb^{-1}. In Figure 5.13b, the same distribution at 32 pb^{-1} is compared with the results from data. Only one event passes the whole ZZ selection, the same selected by the H → 4μ analysis (event 4 in Table 5.4).

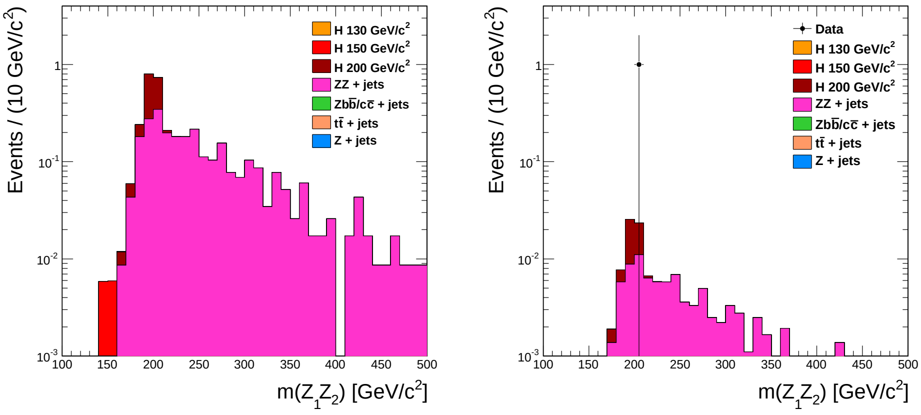

(a) **(b)**

Figure 5.13: *Four-muon invariant mass spectrum after the ZZ selection, for integrated luminosities of (a) 1 fb^{-1} and (b) 32 pb^{-1}, compared with the results of the same selection applied on CMS data (black marker). Higgs bosons with masses 130, 150 and 200 GeV/c^2 are also shown for reference. The Monte Carlo distributions are stacked.*

Measurement of the $Zb\bar{b}$ and $t\bar{t}$ Background Contributions from Data

A small number of $t\bar{t}$, $Zb\bar{b}$ and Z + jets events survive the whole selection described in Section 5.6.4. To measure the contamination from these backgrounds, a control region can be defined by inverting some cuts in the standard selection.

A possible strategy to isolate background events can profit from the following cuts, applied on top of the standard skim (Section 5.5.1):

- four muon invariant mass larger than 100 GeV/c^2, to suppress the QCD background;
- invariant mass of the off-shell Z candidate (according to the definition in Section 5.3.3) below 60 GeV/c^2, to suppress ZZ and Higgs signal;
- largest value of $\mathrm{S_{IP}}$ larger than 4;
- isolation variable $\mu\mathrm{Iso}_{2\,\mathrm{least}}$ larger than 0.2.

In Figure 5.14a, the invariant mass spectrum of the on-shell Z boson candidate in this control region is shown for an integrated luminosity of 1 fb^{-1}. In Figure 5.14b, the same distribution is compared with CMS data: one event is found, which is event 2 of Table 5.4.

As shown in these plots, Higgs signal and ZZ background are removed almost completely. The contributions from $t\bar{t}$ and $Zb\bar{b}$ processes can be separated by fitting the peak and the non-resonant continuum in the invariant mass distribution of the on-shell Z candidate. A small contamination from Z + jets events is still present and cannot be disentagled from the $Zb\bar{b}$ component. Since the fraction of such events is reasonably small, their contribution can be accounted for by adding a systematic uncertainty to the total error in the count of $Zb\bar{b}$ events. The systematic error on the expected number of events in the Z mass distribution can be estimated by performing pseudo-experiments, varying the number of initial expected events with a Poisson distribution. A total error of the order of 35% is found, assuming 100% uncertainty on the number of Z + jets events contaminating the mass peak [61][67].

Alternatively, the simple isolation cut described above can be replaced by the bidimensional cut on the distribution $\mu\text{Iso}_{2\,\text{least}}$ *vs.* p_T of the third or fourth muon, as explained in Section 5.6.1 and shown in Figure 5.5. The control region found by inverting these bidimensional cuts is basically free from signal and more populated by $Zb\bar{b}$ events than the region defined by simple isolation cuts. A possible strategy exploiting this selection is described elsewhere [60].

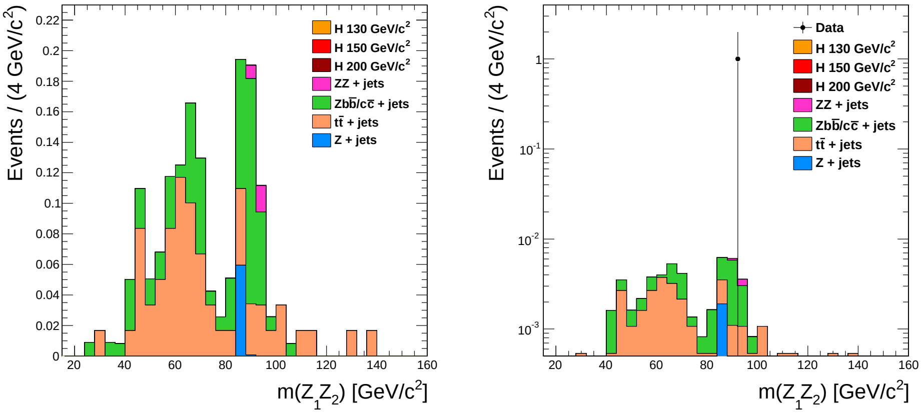

(a) **(b)**

Figure 5.14: *Measured invariant mass distribution of the on-shell* Z *candidate for events in the* $t\bar{t}/Zb\bar{b}$ *control region, (a) for an integrated luminosity of 1* fb^{-1} *(linear scale) and (b) 32* pb^{-1} *(logarithmic scale), compared with the results of the same selection applied on CMS data (black marker). In both figures, the Monte Carlo distributions are stacked.*

5.8.2 Control of Systematics from Data

Several methods have been developed to measure muon efficiencies, resolution, momentum scale and other properties directly from data. A brief list is provided in the following.

Muon Efficiencies

Muon reconstruction efficiency can be measured from data with the tag-and-probe method, using muon decays of J/ψ (for low p_{T}) and Z (for high p_{T}), as explained in Section 3.7 and in Appendix C. With 1 fb^{-1}, the single muon reconstruction efficiency can be measured with an uncertainty better than 1%, depending on muon kinematics. Knowing the single muon efficiency and the kinematics of muons in $\mathrm{H} \rightarrow 4\mu$ and $\mathrm{ZZ} \rightarrow 4\mu$ events, the 4μ efficiency can be deduced with a precision better than 4%. Comparing the results of this method on simulated data with the efficiency obtained from Monte Carlo truth, a systematic discrepancy of about 2% is found.

The tag-and-probe technique is also used to evaluate the HLT efficiency. The corresponding uncertainty, for the purpose of this analysis, is found to be negligible. The efficiency of some analysis cuts, such as isolation, vertexing, etc., can be measured with the same method as well.

Muon Momentum Resolution

Muon p_{T} resolution can be measured from data using methods that exploit the J/ψ and Z mass peaks, such as the `MuScleFit` algorithm, described in Chapter 4. The uncertainty on the muon p_{T} resolution directly propagates into the four-muon invariant mass reconstruction. The $m(4\mu)$ distribution width drives the width of the search window that will be used for evaluating the significance of a signal excess at low Higgs masses. The uncertainty on the width of the window is estimated to be around 3% and its effect is almost negligible: even an error as large as 25% would have a very small impact on the signal significance.

Applying this method on simulated data, the $m(4\mu)$ resolution inferred from single muon p_{T} resolution can be compared with the Monte Carlo truth. The results are in good agreement for $m(4\mu) < 200$ GeV/c^2, while significant deviations are found for larger masses. The reason of this discrepancy is under investigation, but it does not affect the results presented here.

Muon Momentum Scale

The momentum scale of muons and the corresponding uncertainty can be determined with the same tools used for the momentum resolution (Chapter 4). This uncertainty is very small and usually neglibible in this analysis, and affects significantly the number of background events in a given mass window only on steep slopes of the $m(4\mu)$ distribution, especially between 180 and 200 GeV/c^2. Even in this region, however, this effect can be neglected if the momentum scale is known with a precision better than 0.1 GeV/c, which is reached with few hundred $\mathrm{Z} \rightarrow 2\mu$ events.

Muon Isolation

The main source of systematics on muon isolation is the limited knowledge of the *underlying event*. Previous studies [68] using different models for the underlying event have shown that the variation of the isolation efficiency can be as large as 5%.

Several strategies are available to measure the isolation efficiency directly from data. The tag-and-probe method can be used, but it was found to give uncertainties of the order of 10%. Thus, dedicated methods have been developed, such as the *random cone* [69][68] and the *kinematic template* [61] techniques. Using these, the isolation cut can be calibrated with few tens of selected Z + jets events and with uncertainties as low as 1%.

Vertexing Algorithm

A strategy for measuring the background rejection power of IP-based selections has been developed. This method is based on a control sample including one Z candidate plus a b-tagged jet, provided that b-tagging algorithm does not make use of the IP information (e.g. see [70]) and provides a pure selection. Fake Higgs candidates are then built by combining the muons associated to the Z candidate with any other pair of tracks in the event, making sure that the four tracks satisfy some minimum requirements for a signal-like event (two- and four-muon invariant masses as in Section 5.5.2). Once this sample of "fake Higgs" has been extracted, the background power rejection obtained by cutting on the worst $\mathrm{S_{IP}}$ track can be checked.

Summary of Systematic Uncertainties

Other than those described in the previous sections, the main sources of systematic uncertainty for this analysis are listed below.

Integrated luminosity: it can be obtained from the measurement of inclusive Z and W bosons production, with the limitation coming from the limited knowledge of the parton density functions in the calculation of the theoretical vector boson cross sections. An uncertainty of 11% is commonly assumed.

Higgs cross section: the dominant production channel, gg → H, is known at the NNLO, complemented with the NNLL resummation. An uncertainty of about 15-20% is assumed, depending mostly on the sensitivity to the QCD scale and on PDF uncertainties [19].

Background cross sections: 2-8% for $q\bar{q} \to \mathrm{ZZ}$, as a function of the 4μ mass; about 30% for $\mathrm{gg} \to \mathrm{ZZ}$, which is only known at the lowest order; about 30% for $\mathrm{Z}b\bar{b}$; 20% for $t\bar{t}$.

5.9 Results

The goal of this search is either to confirm the existence of a Higgs signal or to exclude it. In order to quantify the sensitivity of this analysis to the presence of a Higgs boson signal, a simple *counting experiment* approach is adopted. The results are here presented for an integrated luminosity of 1 fb^{-1}, for the 4μ final state and for a combination of the three leptonic channels.

5.9.1 Significance

In a counting experiment, for any given Higgs mass hypothesis m_{H}, the events are counted in a mass window $m(4\ell) \pm 2\sigma(m(4\ell))$. This window slides along the measured mass spectrum of Figure 5.8b to test the various possible m_{H} hypotheses.

Given the mean number of expected signal and background events in the mass window, $\bar{s}$ and $\bar{b}$ respectively, the *likelihood ratio* $Q(n)$ is defined as

$$Q(n) \;=\; \frac{L(n,\, \bar{s}+\bar{b})}{L(n,\, \bar{b})}\,, \tag{5.6}$$

where

$$L(n,\, x) \;=\; \frac{e^{-x}\cdot x^{n}}{n!} \tag{5.7}$$

is the Poisson probability of observing n events when a mean x is expected. In the case of multiple channels, the likelihood ratio is the product of the individual likelihood ratios for each channel.

The estimator used in this analysis is the *log-likelihood ratio*, defined as

$$-\,2\ln Q \;=\; -2(\bar{s}+\bar{b})\ln(1+\bar{s}/\bar{b}) + 2\bar{s}\,, \tag{5.8}$$

which, in the high statistics limit, tends to a $\Delta\chi^2$ distribution.

Under the background-only hypothesis, the *p-value* is the probability for Q to be equal or greater than the Q_{obs} value built with the number of observed events:

$$p \;=\; \mathcal{P}(Q \geq Q_{\text{obs}} \mid b)\,. \tag{5.9}$$

The *significance* for a signal observation is obtained converting the p-value into an equivalent number of one-sided tail σ of a Gaussian distribution. Typically, a significance value of 3 is considered sufficient to claim an observation, while 5 is regarded as the limit to claim a discovery.

In Figure 5.15, the expected sensitivity with 1 fb^{-1} of data is shown as a function of the Higgs boson mass, for the three separate channels and for their combination. The continuous lines, connecting several data points between 115 and 250 GeV/c^2, are obtained by extrapolating the results of previous studies at LHC centre-of-mass energies of 14 and 10 TeV [59][60][61]:

the significancies are simply rescaled to account for the lower cross sections of signal and background processes at 7 TeV. The three red points at 130, 150 and 200 GeV/c^2 show the sensitivity of the optimised strategy presented here, combining the results of the three parallel analyses for the 4μ, $4e$ and $2\mu 2e$ final states: the significance of the present study is higher than that extrapolated from previous studies, especially at low Higgs boson masses. Nevertheless, it is clear that 1 fb^{-1} at 7 TeV is not sufficient for an observation at any $m_{\rm H}$ value, even combining the three channels.

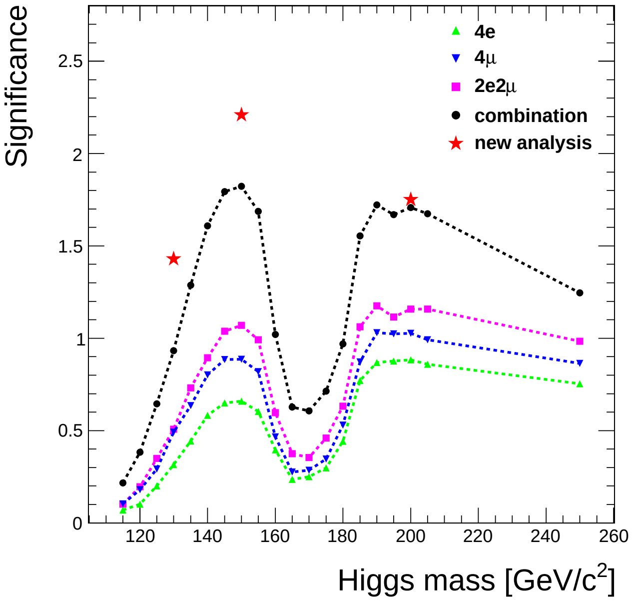

Figure 5.15: *Expected significance of an event excess with 1 fb^{-1} of data, for several Higgs boson mass hypotheses. The continuous lines are extrapolated from analyses at higher energies, as explained in the text, for the three separate leptonic channels and for their combination. The red markers show the significance of the analysis presented here, combining the three channels.*

5.9.2 Exclusion Limits

In the absence of a significant deviation from the background-only hypothesis, an upper limit on the H $\to$ ZZ $\to 4\mu$ cross section σ can be set. This limit is usually expressed in terms of $r = \sigma/\sigma_{\rm SM}$, where $\sigma_{\rm SM}$ represents the expected cross section for a SM Higgs at a given mass. Using a Bayesian approach [61], the exclusion limit is derived from the *a posteriori* probability for r, given n observed events:

$$\mathcal{P}(r) \;=\; \frac{L(n,\,\bar{b}+r\cdot\bar{s})\cdot\pi(r)}{\displaystyle\int_0^\infty L(n,\,\bar{b}+r'\cdot\bar{s})\cdot\pi(r')\,\mathrm{d}r'}\,, \tag{5.10}$$

where $\pi(r)$ is the prior on the value of r. A standard *confidence level* (C.L.) of 95% for the exclusion limit is set by solving the equation

$$\int_r^\infty \mathcal{P}(r)\,\mathrm{d}r \;=\; 0.05\,. \tag{5.11}$$

The experimental uncertainties can be included in the calculation of $L(n,\,\bar{b}+r\cdot\bar{s})$. Systematics are taken to be 100% correlated, which represents the most conservative assumption and is a good approximation in this analysis. However, the effect of including systematics here is rather small, as the sensitivity for an integrated luminosity of 1 fb^{-1} is dominated by the statistical uncertainties.

The Bayesian exclusion limit is obtained by repeating multiple toy Monte Carlo experiments and taking the mean value $\langle r\rangle$ and the 68% fluctuation bands. The results for the three separate channels and for their combination are shown in Figure 5.16. As in the case of the significance, the continuous lines are extrapolations from the analyses at 14 and 10 TeV, while the red markers represent the results of the new analysis, described in the previous sections, for the combination of the three channels. Again, the statistics available at 1 fb^{-1} is not enough to exclude a SM-like Higgs boson at 95% C.L. in the considered mass range, even when combining the three final states.

5.10 Conclusions

The results of this chapter clearly show that the discovery of a SM-like Higgs boson is inaccessible with 1 fb^{-1} of integrated luminosity for an LHC centre-of-mass energy of 7 TeV. The highest significance can be reached for a Higgs boson of mass 150 GeV/c^2, and is slightly above 2. Simply extrapolating this result, at least 2 fb^{-1} are needed for an observation, more than 5 fb^{-1} for a discovery at 7 TeV. A higher energy would obviously improve the discovery potential.

From Figure 5.16, it can be deduced that few fb^{-1} will allow to exclude the existence of the SM Higgs boson in the mass region above 180 GeV/c^2, inaccessible to the Tevatron experiments.

These results also depend on the precision with which the systematics are determined and the backgrounds measured. Hence, the data that CMS will collect in 2011 will mainly serve to measure the background rates, especially for ZZ and $\mathrm{Z}b\bar{b}$, and to improve the knowledge of the detector and of the algorithms used in this analysis.

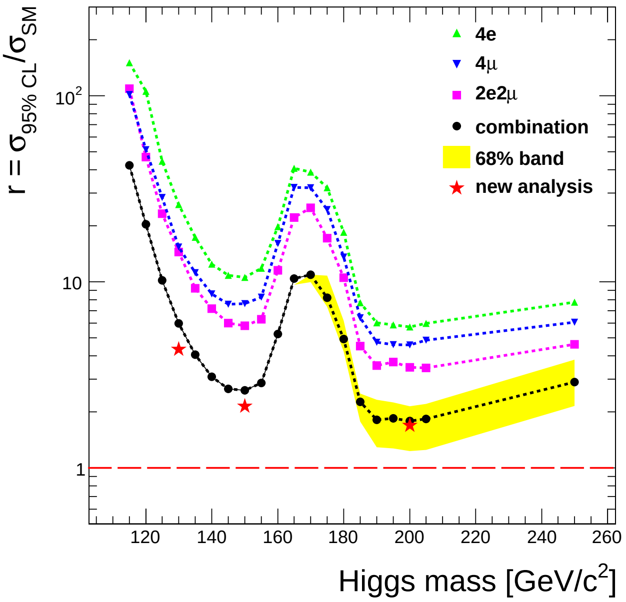

Figure 5.16: *95% C.L. exclusion limits of a SM Higgs boson in the 4μ final state with 1 fb^{-1} of data. On the y axis, the variable $r = \sigma_{95\%}/\sigma_{\rm SM}$ is shown. The continuous lines are extrapolated from analyses at higher energies, as explained in the text, for the three separate leptonic channels and for their combination. The red markers show the significance of the analysis presented here, combining the three channels. The yellow 68% fluctuation band is referred to the old analysis.*

However, the time-scale for a discovery will be driven by the LHC plans concerning the centre-of-mass energy and instantaneous luminosity to be delivered, which are continuously evolving: the discovery could be closer than expected.

Summary

The reconstruction of muon tracks and the precise measurement of their properties play a key role in fulfilling the challenging CMS physics program, since muons provide a clear signature in many analyses. One of the most notable examples is the search of the Standard Model Higgs boson, whose decay into four muons represents the favourite discovery channel at the LHC and allows the most precise measurement of its mass and the determination of its properties. The work presented in this thesis is my contribution to this ideal path, which starts from the development of track reconstruction in the CMS muon spectrometer and comes to the elaboration of a complete analysis strategy for the search of the SM Higgs boson in four muons final state.

The reconstruction of muons combines the information of the inner tracking system with the outer muon spectrometer, to ensure high precision, efficiency and purity. In particular, I developed the algorithms for the reconstruction of tracks in the muon spectrometer. I tested their performance on simulated muons, described some of the features that I introduced to address specific problems and showed the resulting improvements, such as a better resolution in high-momentum muons, a lower ghost rate, and a higher efficiency of muon trigger.

The first year of LHC data taking gave me the chance to test the performance of muon reconstruction and of the last developments on muons from proton-proton collisions, to adapt the algorithms to cope with the evolution of data taking conditions, and to make sure that the reconstruction and trigger are ready to face the data taking of next years at higher luminosities and energies. The results of this work are described in Chapter 3.

After muon reconstruction, the momentum measurement may need further refinements, to eliminate biases coming from several sources, in particular residual misalignments and imperfect knowledge of material budget and magnetic field. Moreover, it is essential to measure precisely the the muon momentum resolution, which is a source of systematic uncertainty for several physics analyses. A dedicated algorithm has been developed for this purpose, called `MuScleFit`, which uses muon pairs from the decay of neutral resonances. In the context of this framework, I explored and developed new strategies to determine scale corrections and resolutions in different muon momentum ranges, exploiting decays of J/ψ mesons and Z bosons. The strategies were first developed on Monte Carlo samples and then applied and optimised on collision data. In Chapter 4, these methods are described and the results obtained on Monte Carlo simulations and data are reported and compared. In the J/ψ case, I selected a large sample of muon pair candidates from 2010 CMS data, which allowed for very detailed corrections. As for the Z boson, the available statistics was obviously lower, so the momentum scale and resolution had to be determined using simpler models. The results of my studies were used in several CMS analyses, in particular for the measurement of the production cross sections of J/ψ and Υ mesons and Z boson [71][72][73]: the models found for scale and resolution were used to apply momentum corrections and to determine the systematic uncertainties.

Finally, I worked on a prospective analysis for the search of the SM Higgs boson in its "golden channel", i.e. the four muon final state. This study has been carried out for the last three years and is part of a more general analysis, involving all the Higgs decays into four leptons (muons and/or electrons). I contributed, in particular, to the four muon channel, in which I could make use of the experience gained in my work on muons. At the beginning, the analysis was developed considering an LHC centre-of-mass energy of 14 TeV, which will be eventually reached in the next years, and a total integrated luminosity of 1 fb^{-1}. Then, following the LHC plans for the start-up and first years of data taking, the same strategy was adapted to lower energies. In the Monte Carlo study reported in Chapter 5, I used the actual conditions of LHC in 2010: 7 TeV energy and $2 \cdot 10^{32}\ \text{cm}^{-2}\,\text{s}^{-1}$ instantaneous luminosity. I considered again an integrated luminosity of 1 fb^{-1}, which will be likely collected within 2011. Using Monte Carlo samples, I analysed the potential of this strategy for the discovery or exclusion of a SM-like Higgs boson in the four muon channel. The results show that no discovery is possible with 1 fb^{-1} at 7 TeV: for Higgs masses around 150 GeV and 200 GeV/c^2, a maximum significance of about 1 is reachable in the four muon channel, slightly more than 2 if all the four lepton channels are combined together. An exclusion at 95% C.L. is not possible either, for any mass value, but upper limits on the cross sections can be fixed. In case of masses below 200 GeV/c^2, applying the selection described in Chapter 5, a Higgs signal would appear in the four muon invariant mass spectrum, as narrow peak above the continuum of the $\text{ZZ}^{(*)}$ background. Finally, I applied the selection strategy to the 2010 CMS data and I found a good agreement with the simulated distributions. The analysis selected one good four muon event, with two on shell Z boson candidates and a four-muon invariant mass of about 200 GeV/c^2.

Appendix A

Kalman Filter

The Kalman filter [45][74] is a recursive method for the fit of a discrete set of data. This method is particularly suited for track fitting, since it allows implementation of reconstruction code which is independent of the number of measurements available.

The problem consists in the determination of an estimate of a generic state vector $\mathbf{x}$ given a set of measurements $\mathbf{m}_k$, which are assumed to have the form

$$\mathbf{m}_k \;=\; H_k\,\mathbf{x}_{k,\,true} \,+\, \epsilon_k\,, \tag{A.1}$$

where H_k is the transform matrix from the state space to the measurement space and ϵ_k is the noise that affects the true state.

In the case of track reconstruction, the state vector is defined as the position and momentum relative to a given surface (in the local coordinate frame):

$$\mathbf{x} = \begin{pmatrix} q/p \\ \tan\phi \\ \tan\theta \\ x \\ y \end{pmatrix}, \tag{A.2}$$

where q is the charge, p is the momentum and ϕ, θ, x and y identify the track direction and position on the surface.

The first step consists in the seed generation. For muon tracks, the seed can either be generated from the parameters of Level-1 candidates or from an approximate state estimation based on the measurements themselves.

Each step is then decomposed into two parts: the prediction of the state vector and of the error covariance matrix on the surface of the next measurement to be included, and the update of the state, i.e. the inclusion of the information from that measurement. They are encapsulated in two basic components, called *propagator* and *updator*. The updator includes all the algebra of the filter, so that the complexity of fitting is reduced to providing an analytic or numeric algorithm to propagate tracks and their errors. The propagator used in the muon system is able to extrapolate a state vector and its covariance matrix in a non-constant magnetic field, taking into account the effect of energy loss and multiple scattering in the material traversed by the track.

An external steering code is also needed to look for the measurements to be included in the fit. The algorithm for the hits search in the muon detectors is described in Section 3.3.2.

The result of a Kalman filter is a state on the surface of the last measurement, which includes all the available information. However, the trajectory parameters calculated at other points of the trajectory do not include the information from all measurements. A special procedure is used to update the parameters at every surface, referred to as *smoothing*.

Figure A.1 gives a pictorial view of the iterative process. x_{k-1}, the filtered state on the $(k-1)^{th}$ layer, is propagated to the k^{th} layer using the formulae

$$\begin{aligned} x_k^{k-1} &= F_{k-1}\, x_k \\ C_k^{k-1} &= F_{k-1}\, C_{k-1}\, F_{k-1}^T + Q_{k-1}\,, \end{aligned} \tag{A.3}$$

where x_k^{k-1} is the estimated state on the k^{th} layer, F_{k-1} is the application to propagate x_{k-1} to the next layer, C_k^{k-1} is the covariance matrix of the predicted state on $k-1$, and Q_{k-1} is the covariance matrix of the process noise (which takes into account the energy loss and the multiple scattering between detectors $k-1$ and k).

On the k^{th} layer, the pattern recognition is performed, usually based on χ^2 criteria, to select the most compatible measurement with the predicted state. Once the best measurement $\mathbf{m}_k$ has been identified, the trajectory is updated with the new information. This task is accomplished by the updator, using the equations

$$\begin{aligned} x_k &= x_k^{k-1} + K_k\,(m_k - H_k\, x_k^{k-1}) \\ C_k &= (1 - K_k\, H_k)\, C_k^{k-1}\,, \end{aligned} \tag{A.4}$$

where

$$K_k = C_k^{k-1}\, H_k^T\, (V_k + H_k\, C_k^{k-1}\, H_k^T)$$

is the *gain matrix* and V_k is the covariance matrix of ϵ_k.

Once all measurements have been filtered, the smoothing step can be performed. Like the filtering step, the smoothing process is iterative (Figure A.2):

$$\begin{aligned} x_k^n &= x_k + A_k\,(x_{k+1}^n - x_{k+1}^k) \\ C_k^n &= C_k + A_k\,(C_{k+1}^n - C_{k+1}^k)\, A_k^T\,, \end{aligned} \tag{A.5}$$

where

$$A_k = C_k\, F_k^T\, (C_{k+1}^k)^{-1}$$

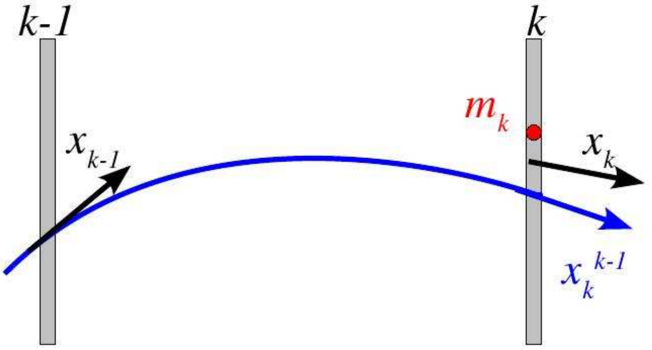

Figure A.1: *Schematic view of the propagation and update of the trajectory state.*

and $n > k$.

The filtered estimate of the state vector is unbiased and has minimum variance among all linear estimates using the same set of measurements. The same holds true for the smoothed estimates. Therefore the Kalman filter with a subsequent smoothing is equivalent to a global linear least-square fit which takes into account all the correlations arising from the process noise.

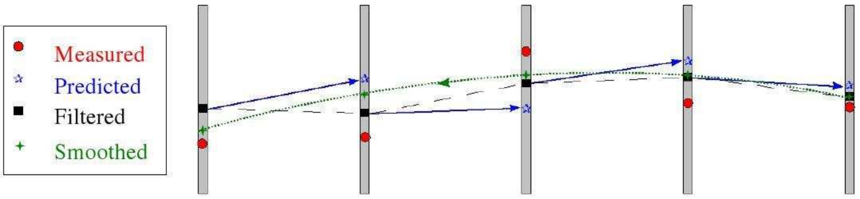

Figure A.2: *Schematic view of the Kalman filter applied to track fitting.*

Appendix B

Configurable Parameters of the Stand-Alone Reconstruction

Configuration of the Forward Filter

Parameter name	**Parameter description**	**Default value**
EnableDTMeasurement	Use DT measurements	true
EnableCSCMeasurement	Use CSC measurements	true
EnableRPCMeasurement	Use RPC measurements	true
Propagator	Track parameter propagator used between hits	SteppingHelix-PropagatorAny
MaxChi2 (compatibility)	Limit on the hit χ^2 compatibility	1000
MaxChi2 (update)	Max $\Delta\chi^2$ to use the hit information	25
RescaleError	Whether to rescale the error prior to the first update	false
RescaleErrorFactor	Rescale factor used if above is true	Not used
Granularity	Determines the dimension of `RecHit` used to update the track parameters	0 (3D segments)

Table B.1: *Configurable parameters for the forward pattern recognition.*

Configuration of the Backward Filter

Parameter name	**Parameter description**	**Default value**
EnableDTMeasurement	Use DT measurements	true
EnableCSCMeasurement	Use CSC measurements	true
EnableRPCMeasurement	Use RPC measurements	true
Propagator	Track parameter propagator used between hits	SteppingHelix-PropagatorAny
MaxChi2 (compatibility)	Limit on the hit χ^2 compatibility	100
MaxChi2 (update)	Max $\Delta\chi^2$ to use the hit information	25
RescaleError	Whether to rescale the error prior to the first update	false
RescaleErrorFactor	Rescale factor used if above is true	Not used
Granularity	Determines the dimension of `RecHit` used to update the track parameters	2 (1D/2D hits)

Table B.2: *Configurable parameters for the backward pattern recognition.*

Configuration of the Final Fit

Parameter name	**Parameter description**	**Default value**
NumberOfIterations	Number of times the filter-smoother is run	3
RescaleError	Factor by which the error matrix is rescaled prior to the final fit	100
ForceAllIterations	Require all iterations to succeed to keep the output	false
MaxFractionOfLostHits	Fraction of lost hits allowed	0.05

Table B.3: *Configurable parameters for the final fit.*

Configuration of the Beam Spot Constraint

Parameter name	**Parameter description**	**Default value**
BeamSpotPosition	Fixed position of the beam spot	Not used
BeamSpotPositionErrors	Error assigned to the beam spot position	$[0.1, 0.1, 5.3]$ cm
MaxChi2	Maximum compatibility of update to vertex	100000

Table B.4: *Configurable parameters for the beam spot constraint.*

Appendix C

The Tag-And-Probe Method

The *tag-and-probe* method is a generic technique that uses resonances, such as Z or J/ψ, to measure from the data itself any sort of per-object efficiency (reconstruction, trigger, etc.) in an almost unbiased way. A general explanation of the method can be found in [48]. Here only a brief description is provided, with particular focus on the applications described in Chapter 3.

A well known mass resonance is used to select particles of the desired type – e.g., muons. In each event, a set of such particles is chosen with very tight identification criteria: these objects are called *tags* and must have very high purity. Another set of particles, known as *probes*, is generally chosen with looser cuts. In principle, probes are not even required to be reconstructed objects of the same type as the tags. In the applications of Chapter 3, for example, tags are chosen as global muons with strict identification cuts, while probes are simple tracker tracks with no muon identification, only some quality requirements.

Resonances are reconstructed by pairing tags and probes, such that the invariant mass of the combination falls in a predefined window around the mass of the resonance. In addition to particle pairs from resonance decays, the mass window will also contain combinatoric backgrounds.

Among all the probes, a subset of *passing probes* is defined according to some selection criterion, whose efficiency is to be measured. The ratio of the number of passing probes and the total number of probes is an estimate of such efficiency, provided that the background has been correctly subtracted: in this case, the "sideband" subtraction is chosen.

The tag-probe pairs are divided in two categories, depending on whether the probe passes or fails the selection. For each category ("passing probes", "failing probes" and "all probes"), the tag-probe invariant mass spectrum is fitted with some signal + background model (see Figure C.1). In the applications of Chapter 3, e.g., the background is fitted using Chebyshev polynomials of second degree, the J/ψ peak with a Crystal-Ball function, and the Z peak with a Voigtian profile. The efficiency is computed from the ratio of the signal yields in the “passing probe” and “all probe” categories. The fits can be performed constraining the ratio to be less than or equal to 1. If the event sample is sufficiently large, the efficiency can be measured separately in different bins of any kinematic variable of the probe, thus obtaining the dependence of the efficiency on the particle kinematics.

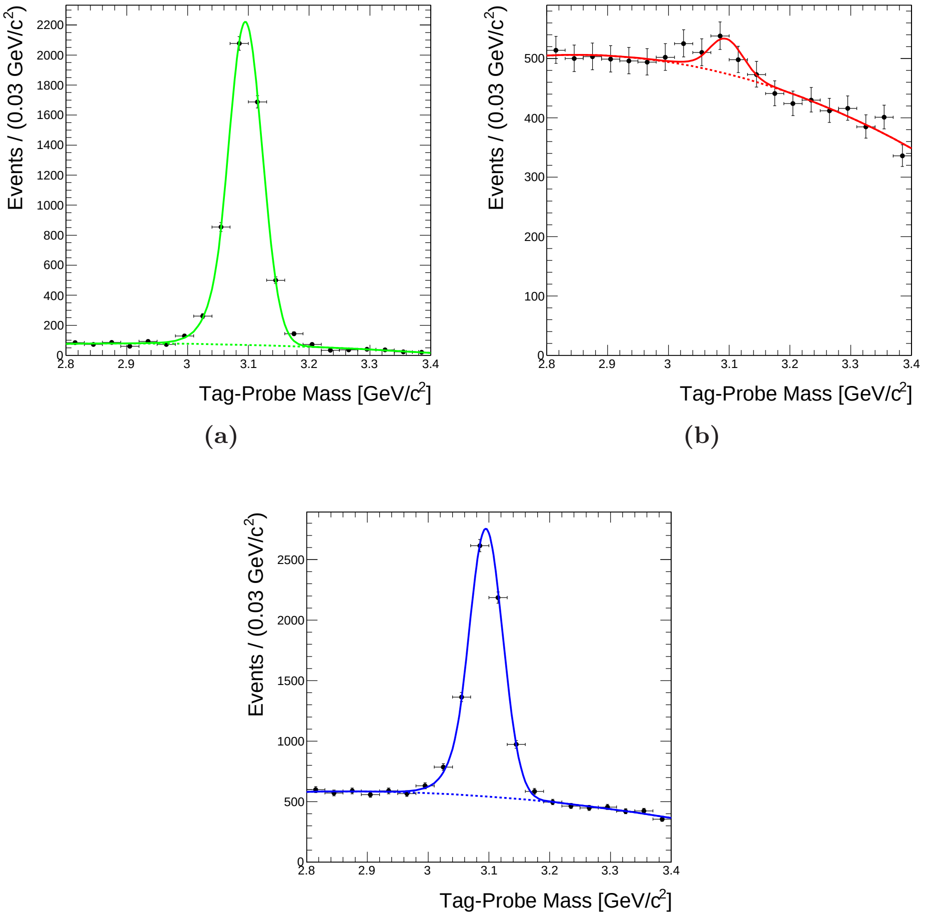

(a) **(b)**

(c)

Figure C.1: *Examples of* J/ψ *line-shapes from CMS data, fitted with a Crystal-Ball function plus a second degree Chebyshev polynomial, for the three categories: (a) passing probes, (b) failing probes and (c) all probes.*

Bibliography

[1] F. Halzen and A. D. Martin, *Quarks and Leptons.* Wiley, 1985.

[2] E. Fermi, "Trends to a theory of Beta radiation," *Nuovo Cimento*, vol. 11, pp. 1–19, 1934.

[3] S. L. Glashow, "Partial Symmetries of Weak Interactions," *Nucl. Phys.*, vol. 22, pp. 579–588, 1961.

[4] S. Weinberg, "A Model of Leptons," *Phys. Rev. Lett.*, vol. 19, pp. 1264–1266, 1967.

[5] A. Salam, *Elementary Particle Theory.* Stockholm: Almqvist & Wiksell, 1968.

[6] S. Dawson, "Introduction to electroweak symmetry breaking," 1998. hep-ph/9901280.

[7] S. Bolognesi, C. Mariotti, and D. Trocino, "The standard model Higgs boson," pp. 139–155, 2006. In *Frascati 2006, Monte Carlo's, physics and simulations at the LHC.* Part 1.

[8] G. Ridolfi, "Search for the Higgs boson: Theoretical perspectives," 2001. `arXiv:0106300 [hep-ph]`.

[9] *LEP design report.* CERN, 1984.

[10] P. Proudlock, "LEP200 Design report," Tech. Rep. SL-PC-Tech-Note-91-87, CERN, Geneva, Jun 1991.

[11] *SLC design handbook. Stanford Linear Collider. Design report.* Stanford, CA: SLAC, 1984.

[12] Tevatron I Group, "Design Report Tevatron 1 Project," 1984. FERMILAB-DESIGN-1984-01.

[13] The LEP Working Group for Higgs boson searches, "Search for the standard model Higgs boson at LEP," *Phys. Lett.*, vol. B565, pp. 61–75, 2003.

[14] CDF and DØ Collaborations, "Combined CDF and DØ Upper Limits on Standard Model Higgs-Boson Production with up to 6.7 fb^{-1} of Data," 2010. `arXiv:1007.4587 [hep-ex]`.

[15] The LEP Collaborations, the LEP Electroweak Working Group, "A Combination of preliminary electroweak measurements and constraints on the standard model," 2006. `arXiv:0612034 [hep-ex]`.

[16] The LEP Electroweak Working Group. `http://lepewwg.web.cern.ch/LEPEWWG/`.

[17] Tevatron Electroweak Working Group. `http://tevewwg.fnal.gov/`.

[18] LHC Higgs Cross Section Working Group, S. Dittmaier, C. Mariotti, G. Passarino, R. Tanaka (Eds.), *et al.*, "Handbook of LHC Higgs Cross Sections: 1. Inclusive Observables," 2011. `arXiv:1101.0593 [hep-ph]`.

[19] C. Mariotti *et al.*, "LHC Higgs Cross Section Working Group." `https://twiki.cern.ch/twiki/bin/view/LHCPhysics/CrossSections`.

[20] "LHC Design Report." CERN 2004-003, 2004.

[21] K. Nakamura *et al.*, "Review of particle physics," *J. Phys.*, vol. G37, p. 075021, 2010.

[22] H. L. Lai *et al.*, "Improved parton distributions from global analysis of recent deep inelastic scattering and inclusive jet data," *Phys. Rev.*, vol. D55, pp. 1280–1296, 1997.

[23] R. Adolphi *et al.*, "The CMS experiment at the CERN LHC," *JINST*, vol. 3, p. S08004, 2008.

[24] The CMS Collaboration, "The CMS Physics Technical Design Report, Volume I: Detector performance and software," Tech. Rep. CERN/LHCC 2006-001 and CMS TDR 8.1, CERN, 2006.

[25] The CMS Collaboration, "The Magnet Project Technical Design Report," Tech. Rep. CERN/LHCC 97-10 and CMS TDR 1, CERN, 1997.

[26] S. Chatrchyan *et al.*, "Precise Mapping of the Magnetic Field in the CMS Barrel Yoke using Cosmic Rays," *JINST*, vol. 5, p. T03021, 2010.

[27] The CMS Collaboration, "The Tracker Project Technical Design Report," Tech. Rep. CERN/LHCC 98-6 and CMS TDR 5 (1998), CERN, 1998.

[28] CMS Collaboration, "Measurement of Tracking Efficiency." CMS PAS TRK-10-002, 2010.

[29] CMS Collaboration, "Tracking and Primary Vertex Results in First 7 TeV Collisions." CMS PAS TRK-10-005, July 2010.

[30] The CMS Collaboration, "The Electromagnetic Calorimeter Project Technical Design Report," Tech. Rep. CERN/LHCC 97-33 and CMS TDR 4, CERN, 1997.

[31] The CMS Collaboration, "The Hadronic Calorimeter Technical Design Report," Tech. Rep. CERN/LHCC 97-31 and CMS TDR 2, CERN, 1997.

[32] The CMS Collaboration, "The Muon Project Technical Design Report," Tech. Rep. CERN/LHCC 97-32 and CMS TDR 2, CERN, 1997.

[33] S. Chatrchyan *et al.*, "Performance of the CMS Drift Tube Chambers with Cosmic Rays," *JINST*, vol. 5, p. T03015, 2010.

[34] S. Chatrchyan *et al.*, "Performance of the CMS Cathode Strip Chambers with Cosmic Rays," *JINST*, vol. 5, p. T03018, 2010.

[35] The CMS Collaboration, "The TriDAS Project Technical Design Report, Volume I: The Level-1 Trigger," Tech. Rep. CERN/LHCC 2000-038 and CMS TDR 6.1, CERN, 2000.

[36] W. Adam *et al.*, "The CMS high level trigger," *Eur. Phys. J.*, vol. C46, pp. 605–667, 2006.

[37] The Geant4 Collaboration, "GEANT – Detector Description and Simulation Tool."
`http://geant4.web.cern.ch/geant4/`.

[38] T. Sjostrand, L. Lonnblad, S. Mrenna, and P. Z. Skands, "Pythia 6.3 physics and manual," 2003.

[39] S. Chatrchyan *et al.*, "Alignment of the CMS Silicon Tracker during Commissioning with Cosmic Rays," *JINST*, vol. 5, p. T03009, 2010.

[40] S. Chatrchyan *et al.*, "Alignment of the CMS Muon System with Cosmic-Ray and Beam-Halo Muons," *JINST*, vol. 5, p. T03020, 2010.

[41] S. Chatrchyan *et al.*, "Aligning the CMS Muon Chambers with the Muon Alignment System during an Extended Cosmic Ray Run," *JINST*, vol. 5, p. T03019, 2010.

[42] M. L. Mangano, M. Moretti, F. Piccinini, R. Pittau, and A. D. Polosa, "ALPGEN, a generator for hard multiparton processes in hadronic collisions," *JHEP*, vol. 07, p. 001, 2003.

[43] E. Gatti, A. Longoni, P. Semenza, and H. Okuno, "Optimum Geometry For Strip Cathodes Or Grids In MWPC For Avalanche Localization Along The Anode Wires," *Nucl. Instrum. Meth.*, vol. 163, pp. 83–92, 1979.

[44] S. Chatrchyan *et al.*, "Performance Study of the CMS Barrel Resistive Plate Chambers with Cosmic Rays," *JINST*, vol. 5, p. T03017, 2010.

[45] R. Fruhwirth, "Application of Kalman filtering to track and vertex fitting," *Nucl. Instrum. Meth.*, vol. A262, pp. 444–450, 1987.

[46] V. Khachatryan *et al.*, "CMS Tracking Performance Results from early LHC Operation," *Eur. Phys. J.*, vol. C70, pp. 1165–1192, 2010.

[47] CMS Collaboration, "Performance of muon identification in pp collisions at $\sqrt{s} = 7$ TeV." CMS PAS MUO-10-002, 2010.

[48] N. Adam *et al.*, "Generic Tag and Probe Tool for Measuring Efficiency at CMS with Early Data." CMS AN-2009/111, June 2009.

[49] S. Chatrchyan *et al.*, "Performance of the CMS Level-1 Trigger during Commissioning with Cosmic Ray Muons and LHC beams," *JINST*, vol. 5, p. T03002. 49 p, Dec 2009.

[50] E. Migliore and G. Sguazzoni, "Altered scenarios of the CMS Tracker material for systematic uncertainties studies." CMS NOTE-2010/010, May 2010.

[51] S. Bolognesi *et al.*, "Calibration of track momentum using dimuon resonances in CMS." CMS AN-2010/059, March 2010.

[52] S. Bolognesi *et al.*, "MuScleFit: muon momentum scale calibration and momentum resolution fit."
`https://twiki.cern.ch/twiki/bin/viewauth/CMS/MuonScaleCalib`.

[53] C. M. Carloni Calame, G. Montagna, O. Nicrosini, and A. Vicini, "Precision electroweak calculation of the production of a high transverse-momentum lepton pair at hadron colliders," *JHEP*, vol. 10, p. 109, 2007.

[54] T. Skwarnicki, *A Study Of The Radiative Cascade Transitions Between The Upsilon-Prime And Upsilon Resonances* (Appendix E). PhD thesis, DESY F31-86-02, 1986.

[55] CMS Collaboration, "Measurement of Momentum Scale and Resolution using Low-mass Resonances and Cosmic Ray Muons." CMS PAS TRK-10-004, July 2010.

[56] V. Maroussov, *Fit to an analytic form of the measured central CMS magnetic field.* PhD thesis, CMS TS-2009/018, 2008.

[57] CMS Collaboration, “Measurement of the W and Z inclusive production cross sections at $\sqrt{s} = 7$ TeV with the CMS experiment at the LHC.” CMS PAS EWK-10-002, 2010.

[58] J. Olivero and R. Longbothum, “Empirical fits to the voigt line width: A brief review,” *Journal of Quantitative Spectroscopy and Radiative Transfer*, vol. 17, no. 2, pp. 233–236, 1977.

[59] CMS Collaboration, “Search for the Higgs boson in the ZZ* decay channel with the CMS experiment.” CMS PAS HIG-08-003, 2010.

[60] D. Trocino *et al.*, “Search strategy for the Higgs boson in the $ZZ^{(*)}$ decay channel with the CMS experiment.” CMS AN-2008/050, June 2008.

[61] D. Trocino *et al.*, “Search strategy for the Higgs boson in the $ZZ^{(*)}$ decay channel at $\sqrt{s} = 10$ TeV with the CMS experiment.” CMS AN-2010/237, April 2010.

[62] J. Alwall *et al.*, “MadGraph/MadEvent v4: The New Web Generation,” *JHEP*, vol. 09, p. 028, 2007.

[63] S. Alioli, P. Nason, C. Oleari, and E. Re, “A general framework for implementing NLO calculations in shower Monte Carlo programs: the POWHEG BOX,” *JHEP*, vol. 06, p. 043, 2010.

[64] A. Pukhov *et al.*, “CompHEP: A package for evaluation of Feynman diagrams and integration over multi-particle phase space. User’s manual for version 33,” 1999.

[65] J. Campbell and K. Ellis, “MCFM - Monte Carlo for FeMtobarn processes.”
`http://mcfm.fnal.gov/`.

[66] S. Abdullin *et al.*, “Study of PDF and QCD Scale Uncertainties in pp→ ZZ → 4μ Events at the LHC.” CMS NOTE-2006/068, April 2006.

[67] N. De Filippis, C. Mariotti, and L. Nervo, “Strategy for the observation of the first ZZ events produced at 7 and 10 TeV center of mass energy in the CMS experiment.” CMS AN-2010/228, July 2010.

[68] S. Abdullin *et al.*, “Sensitivity of the Muon Isolation Cut Efficiency to the Underlying Event Uncertainties.” CMS NOTE-2006/033, January 2006.

[69] G. L. Bayatian *et al.*, “CMS technical design report, volume II: Physics performance,” *J. Phys.*, vol. G34, pp. 995–1579, 2007.

[70] CMS Collaboration, “Algorithms for b Jet identification in CMS.” CMS PAS BTV-09-001, 2009.

[71] V. Khachatryan *et al.*, “Prompt and non-prompt J/ψ production in pp collisions at $\sqrt{s} = 7$ TeV,” 2010. `arXiv:1011.4193 [hep-ex]`.

[72] V. Khachatryan *et al.*, “Measurement of the Inclusive Υ production cross section in pp collisions at $\sqrt{s} = 7$ TeV,” 2010. `arXiv:1012.5545 [hep-ex]`.

[73] V. Khachatryan *et al.*, “Measurements of Inclusive W and Z Cross Sections in pp Collisions at $\sqrt{s} = 7$ TeV,” 2010.

[74] R. Bellan and E. Migliore, *Study and Development of the CMS High Level Trigger and Muon Reconstruction Algorithms and Their Effects on the* $pp \to \mu^+\mu^- jjjj$ *Vector Boson Fusion Process* (Appendix A). PhD thesis, CMS TS-2008/021, Università degli Studi di Torino, 2007. Presented on 28 Nov 2007.